UNIVERSITY OF CALIFORNIA, MERCED

Numerical Simulations of Manipulation of Microparticles by Droplets in Digital Microfluidics

by

Chuanjin Lan

A dissertation submitted in partial satisfaction of the
requirements for the degree of
Doctor of Philosophy

in

Mechanical Engineering

Committee in charge:
Professor Yanbao Ma, Chair
Professor Gerardo C. Diaz
Professor Shilpa Khatri
Professor Michael F. Modest

Spring 2016

The dissertation of Chuanjin Lan is approved:

Yanbao Ma, Chair — Date

Gerardo C. Diaz — Date

Shilpa Khatri — Date

Michael F. Modest — Date

University of California, Merced

To the unexpected journey I had here.

Acknowledgments

First of all, I would like to sincerely express my special appreciation and thanks to my advisor, Professor Yanbao Ma, for supporting me during these past five years. He has always been supportive and provided me with constant and patient guidance over the years. I would like to thank him for encouraging me and for allowing me to grow as a research scientist, turning me from a dependent graduate student into an independent confident scientific researcher. I hope that I could be as lively, enthusiastic and energetic as Yanbao and in the future be able to command an audience as well as he can.

I am also very grateful to my dissertation committee, Professor Gerardo C. Diaz and Professor Michael F. Modest from Mechanical Engineering, Professor Shilpa Khatri from Applied Mathematics for their time, insightful comments and constructive guidance on my research and this dissertation.

Furthermore, I must thank my previous and current labmates and colleagues at UC Merced. Dr. Zhen Li has been very helpful in providing advice many times when I began this research. Dr. Souvik Pal also offered me valuable advices during his one year stay in UC Merced. It is also a memorable collaboration with Dr. Mohammad R. Shaeri and Mr. Gene D. Su. on the battery project. I also want to thank my current colleagues Dr. Majid Ahmadlouydarab, Dr. Tao Ren, Dr. Jian Xu, Dr. Dadong Wang, Mr. Chengjie Qin, Mr. Wei Liang, Mr. Zhengxian Qu and Ms. Xiumin Shang for all the support and help in both research and life, and my many other friends whom I cannot name them all herein in both China and USA.

Special thanks to the financial support from UC Merced, the Department of Mechanical Engineering, and the Center for Research in Teaching Excellence at the university. I also want to extend my gratitude to the know-it-all graduate coordinator Tomiko Hale for her kind guidance through my whole Ph.D. study, and graduate coordinators Paul Roberts and Rita Guel from School of Natural Science for giving me the opportunity to teach my favorite Maths and Physics courses.

At last, I especially thank my parents. My hard-working parents have sacrificed their lives for me and without them I would not have made it this far. They have provided unconditional love and care for these many years, and I know I always have my family to count on when times are tough. As the only child in my family, I was not able to accompany them very often during the past five years and I sincerely thank them for their understanding.

Curriculum Vitae

Education

- Ph.D. in Mechanical Engineering. University of California, Merced (UCM). Merced, CA, USA, Aug.2010-May.2016
- B.S. in Thermal and Power Engineering, Harbin Institute of Technology, Harbin, China, Sep.2006-Jul.2010

Publications

1. Lan, C., Xu, J., Qiao, Y., & Ma, Y. (2016). Thermal management for high power lithium-ion battery by minichannel aluminum tubes. Applied Thermal Engineering. (In press)
2. Lan, C., Pal, S., Li, Z., & Ma, Y. (2015). Numerical Simulations of the Digital Microfluidic Manipulation of Single Microparticles. Langmuir, 31(35), 9636-9645.
3. Pal, S., Lan, C., Li, Z., Hirleman, E. D., & Ma, Y. (2015). Symmetry boundary condition in dissipative particle dynamics. Journal of Computational Physics, 292, 287-299.
4. Lan, C., Jia, L., Li, Z., & Ma, Y. (2013). Wall Effect on Separated Flow Around an Inclined Flat Plate at High Incidence. In ASME 2013 International Mechanical Engineering Congress and Exposition (pp. V07AT08A022-V07AT08A022). American Society of Mechanical Engineers.
5. Lan, C., Li, Z., & Ma, Y. (2012). Numerical Study of Sand Deposition and Control by Flat Solar Panels. In ASME 2012 International Mechanical Engineering Congress and Exposition (pp. 643-649). American Society of Mechanical Engineers.

Honors

School of Engineering Dean's Travel Fellowship, UC Merced	2015
Mechanical Engineering Bobcat Fellowship, UC Merced	2015
MEAM Graduate Fellowship Award, UC Merced	2013
MEAM Travel Fellowship Award, UC Merced	2013
Graduate Division General Fellowship, UC Merced	2012

Contents

List of Figures

List of Tables

Nomenclature and Abbreviations

Roman Letters

a_{ij}	repulsion force amplitude between the i^{th} bead and the j^{th} bead, N
A_{ls}	amplitude of attractive force between liquid droplet and solid microparticle, N
A_{lw}	amplitude of attractive force between liquid droplet and wall, N
A_{sw}	amplitude of attractive force between solid microparticle and wall, N
B_{ls}	amplitude of repulsive force between liquid droplet and solid microparticle, N
B_{lw}	amplitude of repulsive force between liquid droplet and wall, N
B_{sw}	amplitude of repulsive force between solid microparticle and wall, N
d	initial distance between droplet and microparticle, m
d_{in}	depth of indentation, m
E	elastic moduli of wall, Pa
$\overrightarrow{e_{ij}}$	unit vector pointing from the i^{th} bead towards the j^{th} bead
$\overrightarrow{f_i}$	total force on the i^{th} bead
$\overrightarrow{F_{ij}^{C}}$	conservative force between the i^{th} bead and the j^{th} bead
$\overrightarrow{F_{ij}^{D}}$	dissipative force between the i^{th} bead and the j^{th} bead
$\overrightarrow{F_{ij}^{R}}$	random force between the i^{th} bead and the j^{th} bead
F_{normal}	normal force from wall to microparticle, N
f_r	rolling friction coefficient, –
f_s	maximum static friction coefficient, –

I	momentum of inertia of the microparticle, kg m^2
k_B	Boltzmann constant, kg m^2 s^{-2} K^{-1}
$\overrightarrow{L}$	angular momentum of the microparticle
m_i	i^{th} bead's mass, kg
m_s	mass of solid microparticle, kg
n	coarse-graining level, –
N_s	number of beads forming a solid microparticle, –
P	pressure, Pa
P^*	nondimensional pressure, –
R	radius, m
r	length, m
r^*	nondimensional length, –
r_C	cutoff radius for repulsive conservative force, m
r_d	cutoff radius for attractive conservative force, m
$\overrightarrow{r_i}$	i^{th} bead's position
$\overrightarrow{r_{iC}}$	position of the centroid of the microparticle
r_{ij}	distance between the i^{th} bead and the j^{th} bead, m
R_l	radius of the liquid droplet, m
Rot_ϕ	rotation matrix for the position of bead after rotating an angle of ϕ
R_s	radius of the solid microparticle, m
R_{xyz}	position of a bead on the microparticle surface
Sc	Schmidt number, –
t	time, s
Δt	time step, s
Δt^*	nondimensional time step, –
T^*	nondimensional temperature, –

U velocity in x direction, m/s

U_{ij} potential between the i^{th} bead and the j^{th} bead, J

$\overrightarrow{v_i}$ i^{th} bead's velocity

$\overrightarrow{v_s}$ velocity of solid microparticle

W probability density function, –

x x coordinate

x_0 start position of the wettability gradient region/initial position of liquid droplet, m

x_f end position of the wettability gradient region, m

y y coordinate

z z coordinate

Greek Letters

ϵ ratio of slip region length to the radius of droplet footprint, –

γ amplitude of dissipative force, N

κ_T isothermal compressibility of water, GPa^{-1}

ν kinetic viscosity, m^2/s

ω_D weight function for dissipative force

ω_R weight function for random force

$\overrightarrow{\omega}$ rotational velocity of the microparticle

Ψ probability for the current state transferring to another state during a certain time interval, –

ρ density, kg/m^3

ρ^* nondimensional density, –

ρ_{bead} number density in DPD model, i.e., the amount of DPD beads in unit volume, –

σ surface tension, N/m

σ_0 the distance at which the L-J potential reaches its minimum, nm

τ^K stress tensor due to bead momentum

τ^U stress tensor due to forces between beads

θ static contact angle, $^\circ$

θ_0 contact angle at the hydrophobic end of the wettability gradient region, $^\circ$

θ_e equilibrium contact angle, $^\circ$

θ_f contact angle at the hydrophilic end of the wettability gradient region, $^\circ$

φ amplitude of random force, N

ζ_{ij} Gaussian white noise with zero mean and unit variance

Subscripts

DPD characteristic value in DPD model

l liquid droplet

MD characteristic value in MD model

s solid microparticle

w wall

Abbreviations

μPIV micro-particle image velocimetry

BD Brownian dynamics

CFD computational fluid dynamics

CFM continuous flow microfluidics

DMF digital microfluidics

DPD dissipative particle dynamics

$DSMC$ Direct Simulation Monte Carlo

$EWOD$ electrowetting-on-dielectric

FDM finite difference methods

FDT fluctuation dissipation theorem

FEM finite element methods

FVM finite volume methods

LBM lattice Boltzmann method

MB magnetic beads

MD molecular dynamics

MDPD many-body dissipative particle dynamics

MPCD multi-particle collision dynamics

PCR polymerase chain reaction

PIC particle-in-cell

PM particulate matter

SDPD smoothed dissipative particle hydrodynamics

SPH smoothed particle hydrodynamics

WG wettability gradient

Abstract

Numerical Simulations of Manipulation of Microparticles by Droplets in Digital Microfluidics
by
Chuanjin Lan
Doctor of Philosophy
in
Mechanical Engineering
University of California, Merced
Professor Yanbao Ma, Chair

Manipulation of microparticles by droplets is a very useful and important technique for many microfluidics applications. Due to the large specific surface necessary for chemical binding and easy recovery from a dispersion, utilization of nanospheres or microspheres has become more and more popular for different medical, biological, and optical applications. The goal of this research is to understand the mechanism for the manipulation of microparticles by droplets. Dissipative particle dynamics (DPD), which is extensively used to model mesoscale flow phenomena, is applied as the numerical tool for this study. A model for solid microparticles is designed to study the interactions among microparticles, liquid droplets, and solid substrates. A spherical shell is used to represent the microparticle, and the shell surface is packed by dense enough beads to avoid undesired penetration of liquid beads into solid microparticles, conserving the momentum automatically. After that, the interaction between a rigid microparticle and a solid substrate is modeled based on contact mechanics, including adhesion forces, normal forces, and friction forces. After the model for microparticles is built, a baseline case simulating the pickup and transport of a hydrophobic microparticle by a droplet is demonstrated and compared with experimental observations. Then, the flow structures within a droplet containing a hydrophobic microparticle are revealed.

With this developed numerical tool, parametric studies are conducted to investigate the effects on the manipulation processes (including pickup, transport, and drop off) of a microparticle by droplet sizes, wetting properties of microparticles, and particle-substrate friction coefficients. The increase of droplet size can speed up the transport of microparticles. However, the increase of particle-substrate friction coefficients can lead to drop-off of a hydrophobic microparticle. The mechanism for the drop-off, or delivery, is analyzed by checking the development of the friction force and driving force on the microparticle during the transport process. The critical velocity, defined as the instantaneous velocity of the microparticle right before the occurrence of delivery, is measured, and it is found that the critical velocity is about same for different sizes of droplets. Based on the numerical results, two different designs, namely passive delivery and active delivery, have been demonstrated to be capable of controlling the location for the delivery of single hydrophobic microparticle without any trap design or external field forces. These numerical results provide a fundamental understanding of interactions among the microparticle, the droplet and the substrate to facilitate the optimal experimental design of digital microfluidic system utilizing microparticles.

Chapter 1

Introduction

In this chapter, the application background for this study is presented first. The manipulation of microparticles by droplets is a new and powerful tool for medical, biological, and optical applications using digital microfluidics. The interaction between microparticles and droplets is of key importance for different chemical and biological processes. The state of the art research on droplet microparticle interaction will be reviewed in the next section, including both experimental and numerical studies. After that, approaches and objectives of this study are presented in detail. In the last section, an outline for future research is given.

1.1 Background of manipulation of microparticles by droplets

Microfluidics technology is a powerful and effective tool that emerged in the 1990s and can perform numerous laboratory operations using very small quantities of samples and reagents in a significantly short time [1]. In the last two decades, there has been a steady increase in the interest and development of tools for microfluidics technology [2], which has been used for an increasing number of applications in the fields of biology [3, 4], chemistry [5, 6], medicine [7–9], optics [10], and so on.

1.1.1 Utilization of microparticles in droplet-based microfluidics

In the early stages of microfluidics technology, continuous-flow microfluidics (CFM) was the first approach. In continuous flows, the fluid is constrained and guided by well-designed microchannels, which leads to several drawbacks, including quick increase of complexity to scale up and low flexibility for even slight design modification [11]. A solution to these drawbacks is found in droplet-based microfluidics or digital microfluidics (DMF). DMF is an alternative technology for lab-on-a-chip systems based on the generation and control of discrete droplets inside micro-devices, in contrast to continuous-flow microfluidics [12–15]. This method produces highly monodisperse droplets as microreactor units in the nanometer to micrometer diameter range, at rates of up to twenty thousand per second. Unlike in continuous-flow systems, droplet-based microfluidics allows for independent control of each individual droplet, by acoustic actuation [16, 17], magnetic actuation [18, 19], optoelectrowetting [20], piezoelectric [21], or asymmetrically changing the interfacial

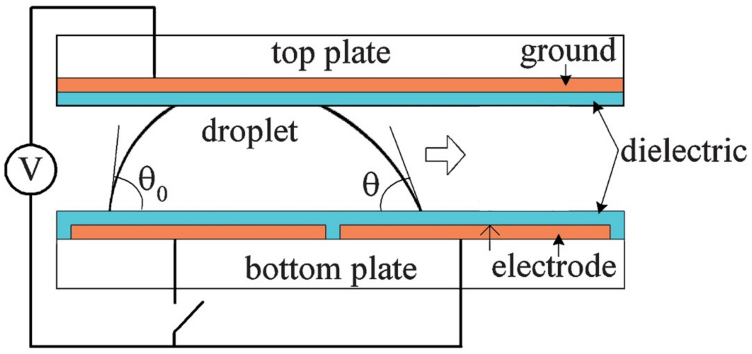

Figure 1.1: Schematic view of an electrowetting device (cross-section) to manipulate droplet, which is confined between two plates coated with hydrophobic dielectric layers [14].

tension (e.g., thermocapillary [22] or electrocapillary/electrowetting-on-dielectric (EWOD) [23]). By far, EWOD is the most popular mechanism used for droplet manipulation (see schematic design in Fig. 1.1 [14]), including droplet positioning, merging [24], splitting [25], and sorting [26]. Since multiple identical microreactor units can be formed in a short time, parallel processing and experimentation can easily be achieved, allowing large data sets to be acquired efficiently. In analogy to digital microelectronics, the basic instructions to control the droplet motions can be combined and reused within hierarchical design structures so that complex procedures (e.g. chemical synthesis or biological assays) can be built up step-by-step, instead of building complex microchannels in continuous-flow systems [12].

Another great advantage that DMF can provide over channel-based microfluidics is its outstanding capability to handle nano-sized or micro-sized solid particles, without the worry of possible clogging as in channel-based microfludics. Due to the large specific surface area (SSA) necessary for chemical binding and easy recovery from a dispersion, utilization of nanospheres or microspheres has become a hot topic for different medical, biological, and optical applications [27, 28], as a review of different applications shows in Fig. 1.2. The typical size of microspheres ranges from tens of nanometers to hundreds of micrometers. The microsphere surface is specially treated or coated to achieve desired binding to specific proteins or cells, so that the capture and transport of target proteins or cells can be implemented by manipulating motions of microspheres. The manipulation of microparticles is of key importance for the control of multi-step biological or chemical processes.

To have more flexible and precise control, magnetic microparticles, also called magnetic beads (MB) in the literature, were recently adopted in different biological and chemical applications [29–31]. Due to easy manipulation by magnetic fields, MB have been proven as multifunctional manipulation vehicles in various lab-on-a-chip systems. MB can be used as mobile substrates to capture target antibodies or DNA, carriers of captured target antigens, labels of target cells and proteins for detection, self-assembled structures to mix fluids, and so on (see Fig. 1.3 [31]).

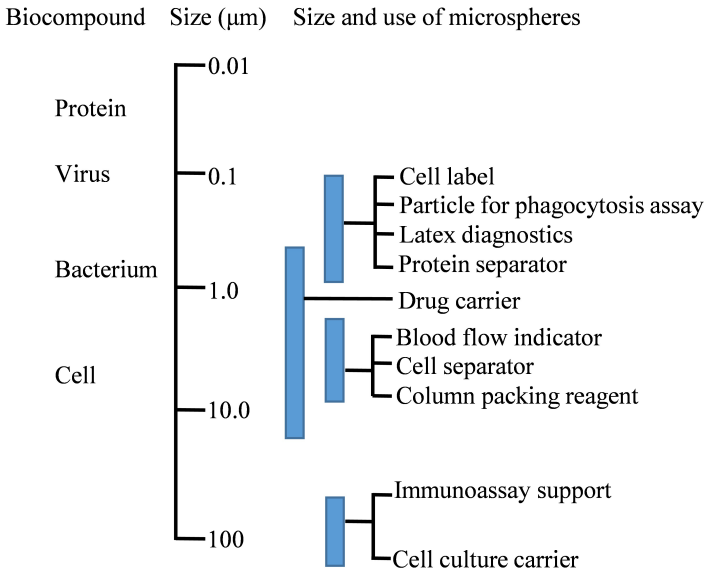

Figure 1.2: Typical sizes and applications of polymer microspheres [28]

1.1.2 Sampling of aerosols using droplet-based microfluidics

Besides the applications utilizing microparticles to facilitate biological or chemical processes, interactions between droplets and microparticles are also important for applications of air-monitoring systems, where droplets are used as samplers and carriers to pick up and transport aerosols collected from the environment. The collected aerosols, or microparticles, will be the sole targets, instead of an auxiliary component of a droplet-based microfluidics system.

Exposure to toxic chemicals or aerosols in environments, such as outdoor, agricultural, and industrial workplaces, has caused adverse health effects for millions of people all over the world. During the last decade, increasing research and public concerns have focused on the massive concentrations of $PM_{2.5}$ and PM_{10} (particulate matter less than $2.5\mu m$ and $10\mu m$, respectively), which threaten people of all ages who perform outdoors activities in cities [32–35]. These fine particles, including dust, dirt, soot, and smoke, can be characterized by their source, e.g., coal burning products and traffic; origin, e.g., anthropogenic or geogenic; or physical chemical properties such as solubility. Besides these air pollutants, biological aerosols, including pollen, fungal spores, bacterial cells, viruses protozoa, and so on, also need to be swiftly detected, which is critically important technology given the increasing risk of bio-terrorism today [36–39].

In order to control and prevent exposure to harmful biological aerosols or particles, an effective sampling and monitoring system is highly needed for quantitative assessment [40–43]. To directly measure aerosol levels, lab-on-a-chip systems can be a promising solution due to its advantages over conventional analytical techniques. As mentioned earlier, these advantages include short processing time, huge reduction in reagent and sample consumption, small mass of the equipment,

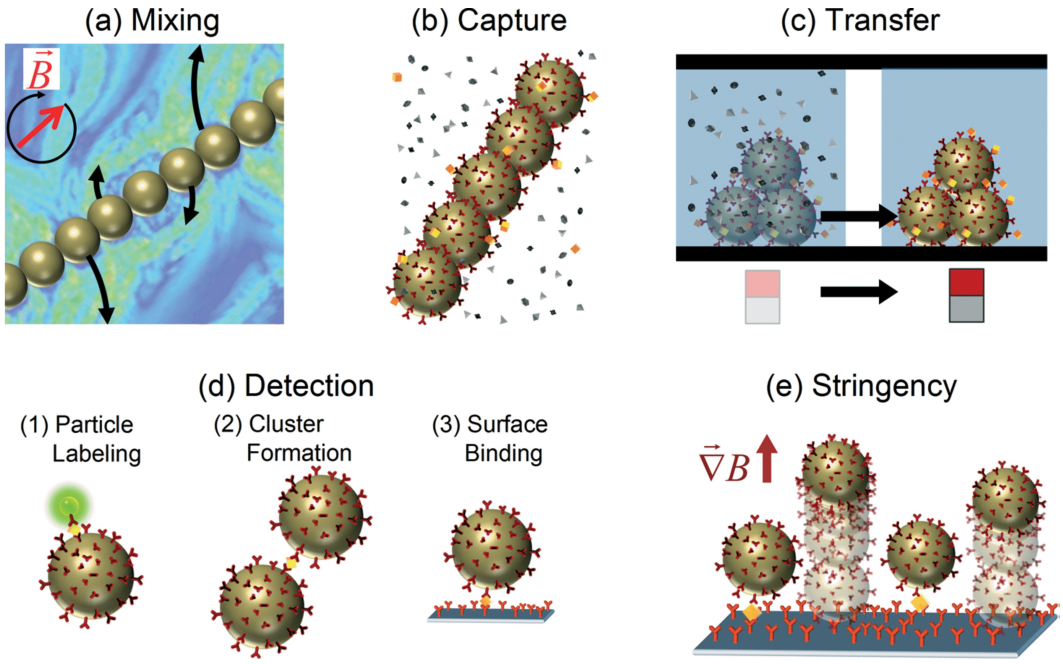

Figure 1.3: Several representative applications of magnetic beads (MB) on lab-on-a-chip devices [31]. By applying magnetic fields, (a) self-assembled regularly-spaced MB can be rotated around certain axes to stir and mix fluids, (b) target analytes can be selectively captured by MB, (c) captured analytes are transferred to another fluid along with the motion of MB, (d) target cell or protein can be labeled and clustered by MB for detection or surface binding, and (e) unbound and weakly bound species are separated from strong bound species in a stringency process.

high throughput, and so on. These make the lab-on-a-chip system a better tool for the quick assessment of biological aerosols than conventional analytical techniques, which usually suffer drawbacks of long analysis time due to culture-based analysis, likely misidentification of cultured morphology and so on [44, 45].

However, there are still some challenges to apply lab-on-a-chip systems for aerosols monitoring, e.g., lack of efficient and compatible samplers. Conventional techniques typically use a large volume of liquid to impinge particles sucked on filter membranes into liquid for follow-up analyses, as well as numerous manual handling steps. It is impractical to incorporate these techniques with a fully automated lab-on-a-chip system that requires a micro-to-pico liter range volume of liquid and miniaturized electromagnetic components. To solve this issue, some new microparticle samplers were developed using droplets [46–48]. The envisioned portable aerosol-monitoring system is illustrated in Fig. 1.4 [48]. The aerosol particles of interest are stopped and collected on the microfilter membrane, the pore size of which is supposed to be slightly smaller than microparticles. Then a liquid droplet, actuated by EWOD or surface acoustic waves, is transported along the microfilter membrane to pick up the collected microparticles.

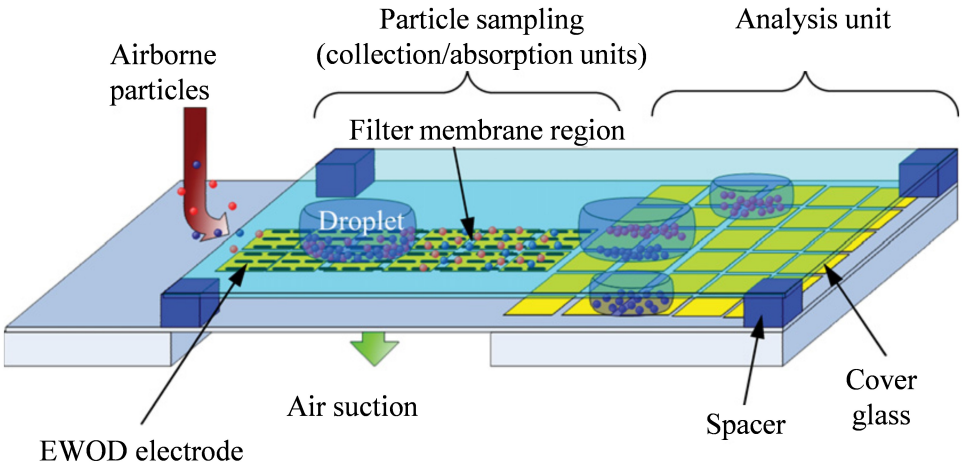

Figure 1.4: Schematic design for an envisioned aerosol-monitoring system [48]. Airborne microparticles are sucked and stopped on the microfilter membrane. Then, a droplet is moved around on the filter by EWOD to pick up and transport the microparticles to adjacent analysis units for downstream on-chip analysis.

1.2 State-of-the-art research

For the applications introduced in the previous section, a fundamental understanding of interactions among microparticles, droplets, and substrates is of critical importance to develop new lab-on-a-chip technologies. However, understandings of the manipulation of microparticles by droplets, such as the pickup, transport, and delivery of microparticles, is still limited, from both experimental and numerical aspects. In this section, the state of the art of research on the manipulation of microparticles by droplets is reviewed from both sides.

1.2.1 Experimental research

The simplest way to manipulate microparticles is to pick them up by droplets [46, 47]. An experimental setup was designed by Zhao and Cho [46] to sample microparticles efficiently using moving droplets actuated by EWOD. Both superhydrophobic (7.9 μm diameter Teflon-coated glass beads, contact angle $\sim$ 160°) and superhydrophilic (7.9 μm diameter glass beads, contact angle $\sim$ 15°) particles were examined to test efficiency, as shown in Fig. 1.6 and Fig. 1.7, respectively. Results showed that the superhydrophilic particles were effectively picked up by the droplet, even clustered together. These particles were suspended inside the droplet and exhibited violent motions possibly due to electrokinetic forces. However, superhydrophobic particles stayed on the air-to-water interface of the droplet, which restricted the particle storage for the droplet. Moreover, the superhydrophobic particles on the interface hindered the droplet movement. A plausible scenario for the pickup of superhydrophobic particles was described (see Fig. 1.5) as clockwise circulation

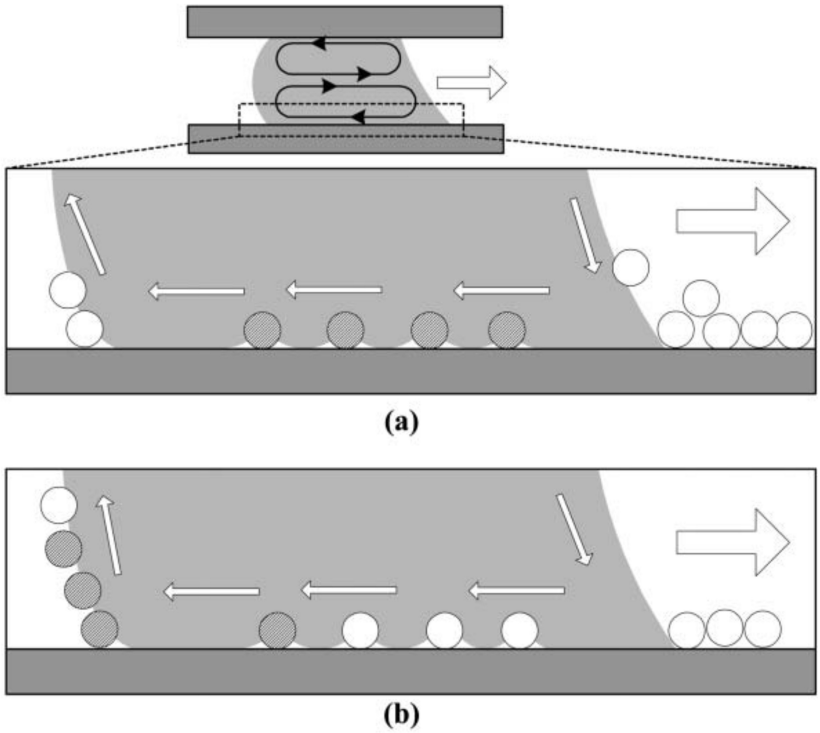

Figure 1.5: Possible scenario of the motion of superhydrophobic particles inside a moving droplet [46]. (a) Fluid circulates in clockwise direction in the lower part of the droplet and in counter clockwise direction in the upper part of the droplet, respectively. (b) The particles are transported to the receding region of the droplet and then are lifted up by the upward fluid motion as the droplet moves right.

took place in the lower part of the droplet and counterclockwise circulation in the upper part. This configuration may explain the low efficiency for pickup of hydrophobic particles, but this still lacks validation to date.

Pickup efficiency was also tested on some other materials, such as microbes and pollen, in the work by Tan et al. [47]. Since airborne bio-particles generally do not exist as smooth microspherical shapes, using pollen with natural roughness would provide a more realistic model than using synthetic analogs. Acoustic waves were used to drive droplets instead of EWOD. Results showed that the pickup efficiency was higher for smaller polystyrene (hydrophobic) particles while lower for smaller melamine (hydrophilic) particles. Another important finding was that the collection efficiency of pollens was always significantly higher than that of comparably sized melamine (hydrophilic) particles, due to the roughness of pollen's surfaces. Furthermore, changing the amount of microparticle density on the substrate did not change the collection efficiency appreciably. In addition to studies on the pickup efficiency for different microparticles, the efficiency for the same bioparticles on different surfaces was also studied [49]. Superhydrophobic surfaces (contact angle

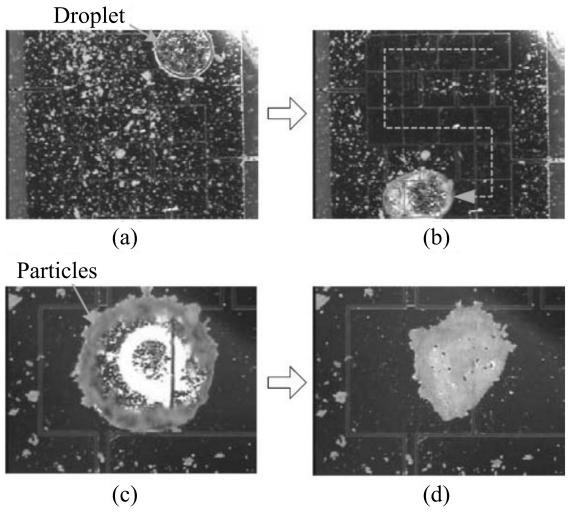

Figure 1.6: Sampling of Teflon-coated hydrophobic glass beads with diameter of 7.9μm. (a) The initial setup of particles and a water droplet before sampling; (b) Particles are sampled by the water droplet along its path; (c) Magnified view of the droplet containing particles; (d) Particles are deposited on the surface after the evaporation of the droplet. [46]

$\sim 160°$) showed higher pickup efficiency by water droplets than hydrophobic surfaces (contact angle $\sim 112°$) for all investigated particles.

Besides the pickup of microparticles, the concentration and separation of different types of electrically charged microparticles from one mother droplet into two daughter droplets were implemented by electrophoresis [50]. Three steps were needed to complete the separation process: (1) isolate two different types of particles by electrophoresis into two different regions inside a mother droplet, (2) physically split the mother droplet into two daughter droplets by electrowetting so that each daughter droplet contains only one type of particles, and (3) transport the daughter droplets by electrowetting to desired locations for further manipulation (see Fig. 1.8). The concept of concentration and separation was successfully demonstrated by a series of experimental results. For the concentration of a single type of particle, 83% of total particles were concentrated into a split droplet having half the volume of the mother droplet. However, due to the undesired vortex generated in the middle of the mother droplet during the separation process, the separation became less controllable. One possible scenario for the vortex generation was due to collision between the particle-dragged flow and the rebound flow inside the fixed meniscus boundary. More studies are needed to understand the physics behind that, which will lead to better control of the manipulation of droplets and microparticles. A similar idea was implemented by Zhao et al. [48], using traveling-wave dielectrophoresis to conduct concentration and separation of microparticles inside a droplet. Using this technique, long-distance transport of various particles can be achieved without liquid pumping, and more importantly, these particles need no charge treatments, thus leading to a wide range of applications. To obtain optimal results for concentration and separation efficiency, applied frequency and medium conductivity are the key parameters to adjust.

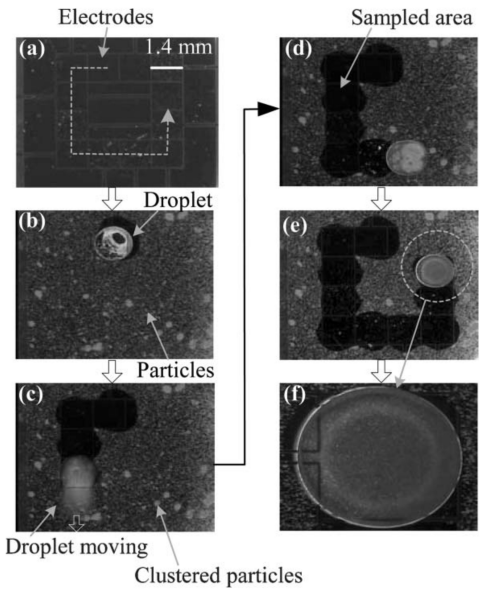

Figure 1.7: Sampling of 7.9 μm diameter borosilicate glass beads (superhydrophilic) [46]. (a) The path of the droplet is indicated by the dashed line; (b) The droplet is displaced on a glass plate covered by superhydrophilic beads; (c), (d) Two snapshots during the transport; (e) End of the transport process; (f) From a close-up view, sampled particles are distributed within the droplet.

In the discussions above, all the results obtained are phenomenological behaviors of a group of microparticles. Though pickup efficiency was obtained for different types of microparticles, the mechanisms for the interaction between droplets and different microparticles were not understood clearly. To have better control of the manipulation, a detailed understanding of flow physics inside a droplet containing microparticles is necessary, as well as interactions between single microparticle and a droplet, from which the behavior of a group of microparticles can be predicted. However, experimental measurements may not be a good option due to experimental costs for a more complicated system design, as well as the microsized scale. The challenge for experimental research at the microscale is to extract flow fields inside a droplet. The conventional micro-particle image velocimetry (μPIV) method is no longer applicable as it needs a sufficient amount of fluorescent tracing microparticles (μm size) to be seeded inside the liquid and tracked by a high speed camera [51–53]. Due to the comparable size with target microparticles, these tracing microparticles will have more effects on the flow fields than target microparticles and affect the desired flow phenomena. On the other hand, numerical simulations can provide qualitative as well as quantitative insights into the phenomena directly and quickly at desired length scales and time scales, at only a fraction of the experimental cost. Numerical research relating to manipulation of droplets and microparticles will be introduced in the following subsection.

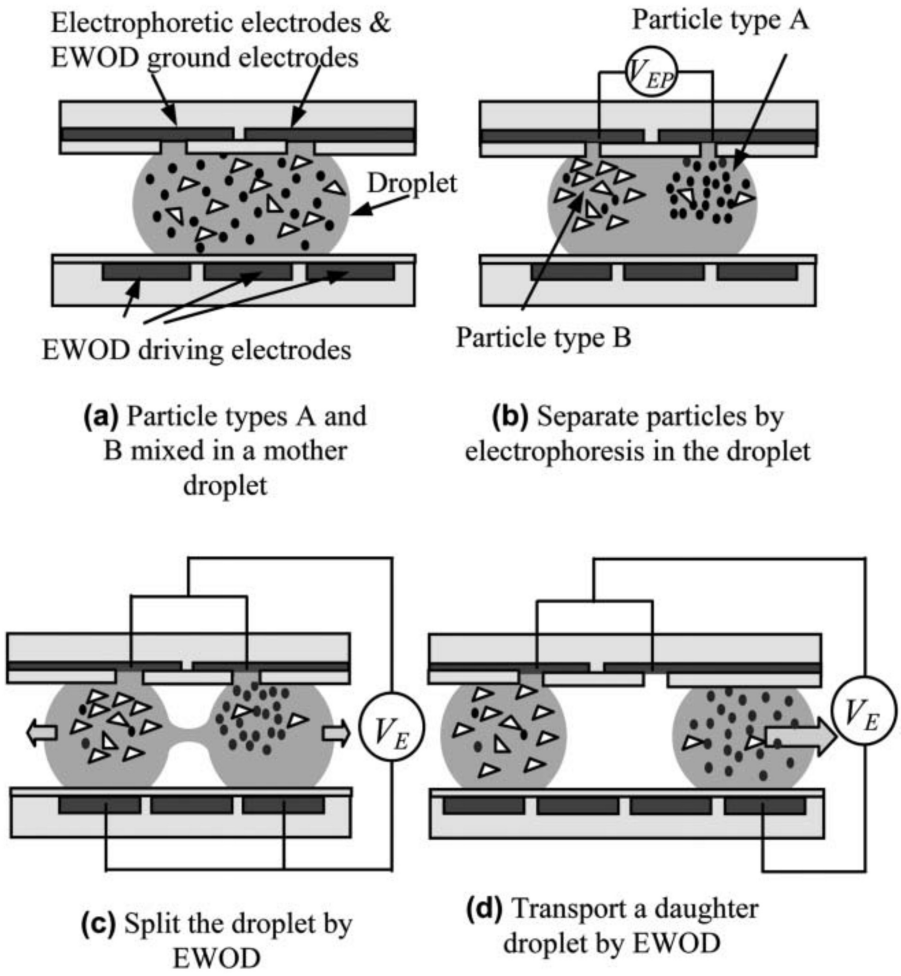

Figure 1.8: Schematic views of binary separation of microparticles in a droplet. After the separation, the droplet is split from the middle. [50]

1.2.2 Numerical research

Computational tools become more and more popular for different fields of scientific research, with exponentially dropping cost and fast developments in computational modeling softwares and packages. In the field of fluid dynamics, computational fluid dynamics (CFD) has already been an important branch for several decades, with theoretical and experimental tools as the other two branches. Numerical tools can be applied to validate analytical models, elucidate experimental results, show design feasibility, and also determine values of variables that cannot be measured experimentally at relatively low cost, in both microfluidics or macro-scale fluids [54].

To examine the problem of droplet microparticle interaction from the numerical perspective, it can be decomposed into several types of numerical problems. These include the free interface

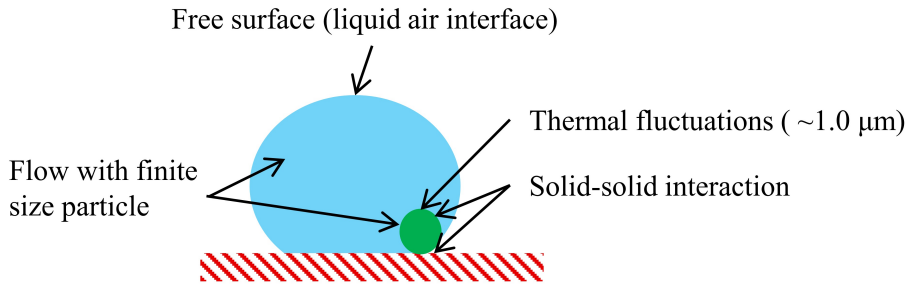

Figure 1.9: Four types of problems coupled for the droplet microparticle interaction: air liquid interface, solid-solid contact, liquid flow with finite size particles and thermal fluctuations.

between liquid and air, solid-solid contact between microparticles and substrates, liquid flow with finite size particles, and thermal fluctuations, as illustrated in Fig. 1.9. Each of them can be a challenging topic to solve, and many numerical methods and models have been developed, as introduced in detail in the following.

The first type of numerical problem to discuss is the simulation of the free interface between liquid and air, or more generally, the moving contact lines in two-phase flows with large (hundreds or thousands of times) density difference. In single-phase flow simulations, finite difference methods (FDM), finite volume methods (FVM), and finite element methods (FEM) are widely applied for different types of flows, e.g., supersonic/subsonic, compressible/incompressible, viscous/inviscid, and so on. For these grid-based methods, to capture the interface of two-phase flows, an additional interface capturing or tracing method has to be incorporated [55]. Four popular and representative methods are briefly introduced here. First, in the level-set method, a signed level-set function is used to track the interface, as the function value represents distance from the interface and the sign represents two different fluids [56–59]. The motion of contact lines is captured by updating the level-set function at each time step. Similarly in the volume-of-fluid method, the volume fraction of the trace fluid, instead of distance function, is used to track the interface [60–63]. Different from these two methods above, the front-tracking method uses a group of discrete Lagrangian markers to represent the interface [64–66]. These Lagrangian markers are explicitly updated according to local flows. Instead of treating the interface as a mathematically sharp interface in the previous three methods, the diffuse-interface method treats it as an interface of finite thickness [67–72].

Besides the grid-based methods mentioned above, there are also various meshfree methods, also called particle methods. Particle methods have been developed as a more convenient numerical simulation tool for certain specific applications, such as the Direct Simulation Monte Carlo (DSMC) method originally designed for modeling rarefied gas dynamics [73–75], particle-in-cell (PIC) method widely used for plasma simulation [76–78], and so on. For the moving contact lines problem, there are also some appropriate particle methods available. The droplet motion and internal three-dimensional velocity field have been studied using smoothed particle hydrodynamics

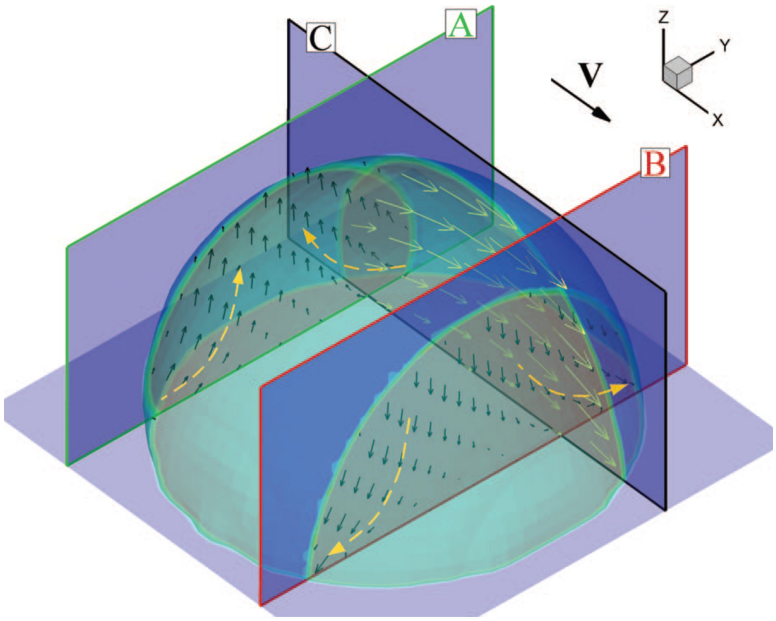

Figure 1.10: The three-dimensional velocity field of the moving droplet by using dissipative particle dynamics (DPD) [82]. Vector V denotes the direction the droplet is moving.

(SPH) [79, 80], lattice Boltzmann method (LBM) [81], molecular dynamics (MD), and dissipative particle dynamics (DPD) [82] (see Fig 1.10). Unlike grid-based techniques, which have to track fluid boundary or interface, these particle methods can represent a free interface for two-phase flows naturally and directly. To have a liquid air interface in particle methods, a convenient way is to use particles to represent denser fluid (usually water) and use empty space to represent air.

The second type of numerical problem pertaining to the droplet microparticle interaction is liquid flow with finite size particles, also called flow past moving rigid bodies. Different computational techniques have been developed using both grid-based methods and particle methods. The grid-based methods first compute the flow fields by solving the Navier-Stokes equations discretized on grids, and then calculate the hydrodynamic forces acting on each solid particle from the solutions of the flow field [83, 84]. The fluid-solid boundaries are tracked and updated for each time step, which is extremely computationally expensive. To save computational load, a fictitious domain method was developed using a fixed grid [85, 86]. The entire domain is computed by solving augmented Navier-Stokes equations on a single fixed grid, and then the velocity field inside each moving body is constrained to a rigid body motion via a Lagrangian multiplier. Compared to these two kinds of grid-based methods, particle methods can easily deal with multiphase flows by directly using different particles to represent different phases [87–89]. To simulate flow with moving rigid bodies in particle method, a rigid body can be formed by a group of particles fixed at their relative positions to the body centroid, as the surfactant nanoparticles modeled in Fig 1.11. Without

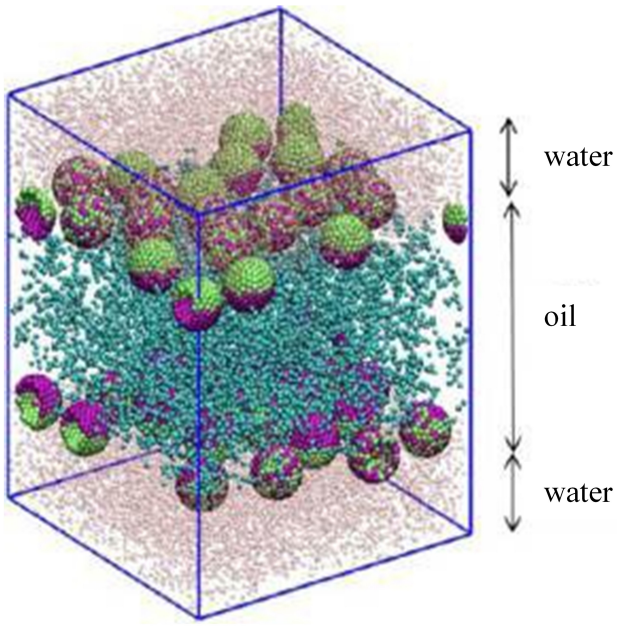

Figure 1.11: Representative snapshot for the oil water system containing nanoparticles at the interfaces by using DPD method [89]. Cyan and pink beads represent oil and water, respectively. Each surfactant nanoparticle is formed by two types of beads, polar beads (green) and nonpolar beads (purple).

refreshing grids at every time step and extra implementation of the complex Lagrangian multiplier, the motion of the rigid body can be solved easily by summing up the hydrodynamics forces from surrounding fluids, or fluid particles.

The third type of numerical problem regarding simulations of droplet microparticle interaction is thermal fluctuations. Thermal fluctuations are an essential part of fluid mechanical problems at microscopic and mesoscopic length scales [90–93]. Particles of a few micrometers, suspended in a quiescent fluid, are small enough to be subject to Brownian motion [94, 95]. To consider thermal fluctuations in numerical simulations, fluctuating hydrodynamics was developed by adding an additional stochastic flux into the deterministic Navier-Stokes equations [96–98]. These fluxes are the macroscopic manifestation of microscopic degrees of freedom, which give rise to hydrodynamic fluctuations and cause Brownian motion. Similarly, a fluctuating LBM was developed to incorporate thermal fluctuations and satisfy the fluctuation-dissipation theorem (FDT) [99–101]. Unlike previous methods, there also exist several mesoscopic particle methods that originally include thermal fluctuations, such as dissipative particle dynamics (DPD) [102, 103], Brownian dynamics (BD), and multi-particle collision dynamics (MPCD) [104, 105], which is a modification of DSMC. In DPD and BD, the random force is explicitly calculated and incorporated into the total force exerted

on each particle, while in MPCD and DSMC the stochastic process happens during the collision of particles.

The last type of numerical problem to investigate is the interaction between microparticle and substrate, or contact mechanics between two solid objects. For simple geometries, such as a solid regular body on an elastic half-space, a good estimation of forces and deformations can be achieved easily by theoretical modeling with appropriate assumptions [106, 107]. However, to solve real engineering problems with complex geometries or contacts, numerical simulation tools are needed to have a good estimation [108]. Different grid-based methods are available for calculating elastic and plastic deformations, such as FEM [109, 110] and boundary element method [111, 112]. Meanwhile, particle methods have also been developed and applied for the simulation of contact and frictional problems, e.g., movable cellular automata [113–115].

From this brief review, it can be seen that there have been many specific numerical methods developed for different types of applications and problems. For each type of numerical problem mentioned above, there are always several options from both grid-based methods and particle methods. However, there still is no universal numerical method for solving many types of problems altogether. For simulation of droplet microparticle interaction, none of the current methods can deal with the four types of problems mentioned above altogether.

1.3 Objectives and approaches

Considering the state of the art reviewed above, there is no experimental or numerical tool at hand to study the manipulation of microparticles by droplets in digital microfluidics. Although some phenomenological results have been obtained from experimental studies, to reveal details such as flow fields inside a droplet and forces on microparticles, current experimental technologies are not capable to quantify them in such small length scales. In contrast, using numerical tools can always show the desired flow variables as long as the numerical model applied is physical and suitable, while the difficulty now is to develop such an appropriate model.

Therefore, in this work numerical approaches are used to study interactions among microparticles, droplets, and substrates. To solve the four types of numerical problems in a coupled fashion, including moving contact lines, flow past moving rigid bodies, thermal fluctuations, and contact mechanics, DPD is chosen as the basic framework according to its advantages introduced in the previous subsection, which are summarized here:

1. As a particle method, DPD can be easily applied to solve three-phase contact line dynamics and interface dynamics. The advantage of particle methods over conventional grid-based methods is that there is no need to explicitly track the interface dynamics or to model the interface motion, because the interface moves naturally with particles. So the contact line dynamics are implicitly handled and controlled by modeling fluid-fluid and fluid-solid particle-particle interactions. In recent studies, DPD has been successfully used to simulate capillary wetting [116, 117] and multiphase flows [118, 119].

2. Also due to the nature of particle methods, DPD can easily deal with multiphase flows, or flow past moving rigid bodies [87–89]. Both liquid and solid phases are represented and solved by Lagrangian particles, with rigid bodies formed by a group of particles fixed at

their relative positions to the body centroid. Then, the motion of each rigid body is updated according to hydrodynamics forces from surrounding fluid particles.

3. DPD is a mesoscopic tool with consideration of thermal fluctuations, which could be a crucial factor for hydrodynamics at nano-scale and micro-scale. For hydrodynamics in microscopic or mesoscopic scales, effects of thermal fluctuations on the droplet, nanojets, and other wetting phenomena have been studied both experimentally and numerically [82, 90–93]. The thermal fluctuations are incorporated into the DPD scheme by applying the stochastic force between each pair of particles. DPD has already been used to show that thermal fluctuations are beneficial for the transportation of the droplet [82].

However, the current DPD method is not capable of solving a problem coupled with both air-liquid interface and moving rigid bodies, let alone contact mechanics between two solid objects. So, the first objective of the present study is to develop such a tool to simulate interactions among microparticles, droplets, and substrates. Then, based on this tool, we can determine what is happening during the droplet microparticle interaction, from among several possible scenarios shown in Fig. 1.12. Besides phenomenological results, flow fields inside a droplet containing microparticles and relevant forces on microparticles will also be analyzed. Based on these, we can have more flexible manipulation of microparticles by droplets. A setup will be designed to control the delivery location of microparticles without any other assistant devices or external forces, which is of much importance for chemical and biological applications. The itemized step-by-step research objectives are briefly outlined below:

1. Literature review for applications and research on the manipulation of microparticles by droplets in digital microfluidics.

2. Use of an in-house DPD code package to simulate benchmark cases and validate the results.

3. Develop a numerical model based on the current DPD method to study the manipulation of microparticles by droplets.

4. Analyze effects from different factors on the manipulation of microparticles by droplets.

5. Design a setup to actively manipulate microparticles by droplets, e.g., control the pickup, transport and delivery of microparticles by droplets.

The numerical results to be obtained from the present work will have a guidance for the design of an effective sampling and monitoring system [40–43]. Based on this new model, the sampling performance for different types of microparticles under different conditions can be analyzed and predicted. Besides that, the flow physics during the transport of a droplet containing a microparticle between neighbor electrodes will be revealed. These results will be beneficial for the control of multi-step biological or chemical processes [27, 28], even without the introduction of magnetic fields. For future work, the magnetic force, which is simply one type of body force, can be easily added into this new model to study and analyze more biological or chemical processes.

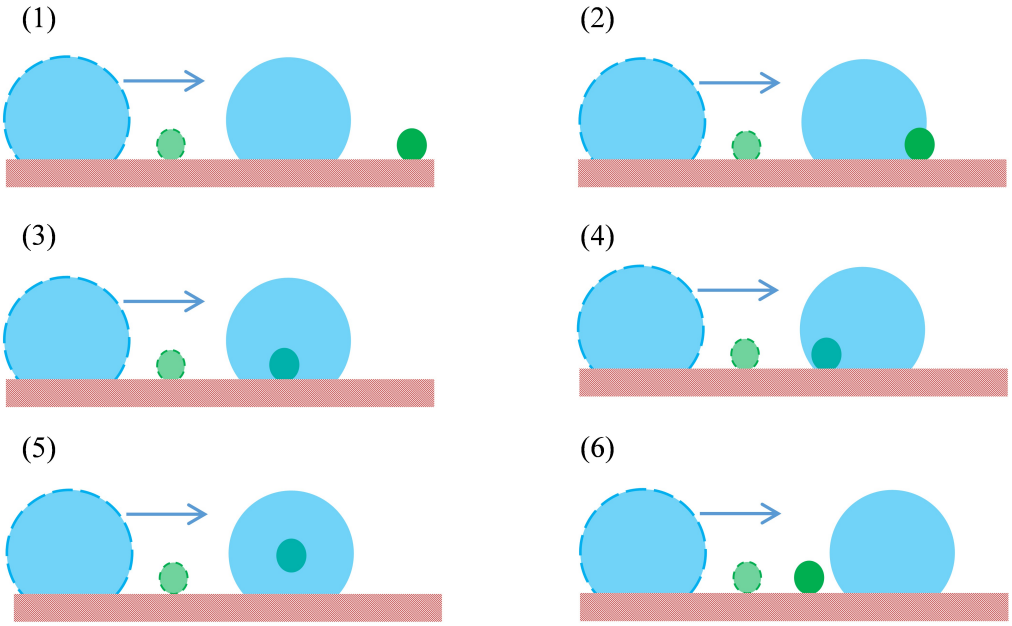

Figure 1.12: Six possible scenarios during the interaction between the droplet (blue) and the microparticle (green). Spheres with boundary in dashed lines represent initial positions, spheres without boundary lines represent the positions afterwards, and the arrow shows the direction of motion. (1) The microparticle is bounced away by the droplet; (2) the microparticle is pushed forward by the front of the droplet; (3) the microparticle is picked up and contained in the bottom middle of the droplet; (4) the microparticle is pushed forward by the rear interface of the droplet; (5) the microparticle is picked up and suspended in the middle of the droplet; and (6) the droplet passed the microparticle and moved away with itself.

1.4 Outline

- In Chapter 2, algorithms and implementation of the current DPD method will be introduced, and validation of the in-house DPD code package will be conducted using benchmark cases.
- In Chapter 3, models of solid microparticles will be designed based on the current DPD framework, and manipulation of a single microparticle by a droplet will be studied.
- In Chapter 4, a parametric study will be conducted of the effects of different factors on the manipulation of microparticles, such as droplet sizes and microparticle properties. Then, a setup which can control the delivery of the microparticle will be designed and demonstrated.
- In Chapter 5, the conclusions of this dissertation will be given by summarizing important achievements in this work and proposing some research topics for the future.

Chapter 2

Dissipative Particle Dynamics

In this chapter, the features of dissipative particle dynamics are presented in the beginning. After that, the theoretical fundamentals and the governing equations of this simulation tool are introduced. The link between DPD and MD, as well as the link between DPD and the Navier-Stokes equations is explained to show that DPD is a method applicable to fluid dynamics, which is specially designed for the mesoscale (between the size of a quantity of atoms and of materials measuring micrometres). Finally, the numerical implementation of the DPD method is introduced, with benchmark validation cases using Poiseuille flow and a moving droplet driven by wettability gradient.

2.1 Fundamentals of Dissipative Particle Dynamics

In this section, the development of mesoscopic simulations tools, especially dissipative particle dynamics, is briefly reviewed, with discussion on the resemblance and difference with other traditional numerical methods.

2.1.1 Mesoscopic particle method by coarse graining

In recent decades, as a powerful particle method solving equations of motion of atoms, MD simulation has been developed to facilitate the understanding of nano-scale physics from the numerical point of view. It is a technique for simulating the movements of atoms and molecules in a classical many-body system, computing the equilibrium and transport properties of the system. The motion of the constituent particles is due to mutual interactions between each pair of them, obeying the laws of classical mechanics. This is an excellent approximation when the frequency of translational, rotational, or vibrational motion is not high enough to cause quantum effects, as well as when the speed is not comparable with the speed of light. To conduct a MD simulation, a model system of N particles needs to be initialized first, by specifying initial temperature, number of particles, initial positions and velocities of particles, density, time step and so on. Then, at each time step, the forces on each particle are calculated, based on which the position and velocity of each particle are integrated using Newton's equations of motion. After the designated time step is finished, quantities of interest are measured for the particular system [120, 121].

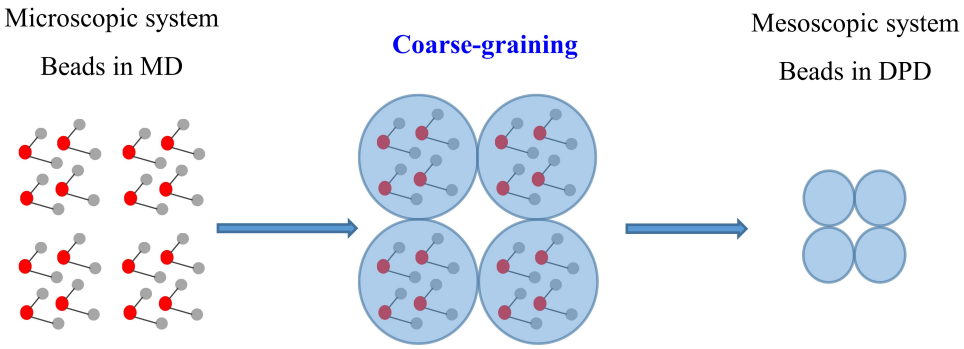

Figure 2.1: Coarse graining from MD beads into DPD beads

With the capability to predict properties and behavior of various molecular systems, MD is limited by its characteristic length and time scales, even with the rapid development of computational power. Current state-of-the-art MD simulations on supercomputers can deal with million-atom systems, amounting to a volume of less than a cubic micron, for a short period of time less than 100 ns [122]. However, in soft matter, many interesting and important technologies are focused on complex fluids at mesoscopic scales, such as suspended macromolecules, bubbles, droplets, lubricants, liquid crystals, and so on. To capture essential features of such systems with limited computational resources, different coarse graining (CG) models have been developed to represent a system with fewer degrees of freedom than those actually present in an atomic system [123]. One way is to assume atomic-scale homogeneous deformations to reduce the degrees of freedom of the systems, however the computational time step in such CG models cannot be increased since atomic interactions are still calculated. Another way is to apply a field representation based on the invocation of a continuum field assumption, which at the same time brings in limitations due to the continuum assumption of the microstructure and micromotion of the material particles [124, 125]. The third way is based on grouping several atoms or molecules into one CG bead, representatives of which are DSMC, PIC, and DPD (see Fig. 2.1). An effective force or interaction model between CG beads needs to be constructed to match the structure or thermodynamics properties with those of the atomic model.

To study a multiphase fluids problem at the mesoscopic scale, several popular numerical methods have been developed in recent decades, including smoothed particle hydrodynamics (SPH), lattice Boltzmann method (LBM), dissipative particle dynamics (DPD), and so on. Originating from the lattice gas automata (LGA) method, the LBM method models fluids using fictive particles. These particles can perform consecutive propagation and collision processes over a discrete lattice mesh. The LBM method has already been applied to various complex fluid systems, such as bubble/droplet dynamics, wetting, and interfaces [126, 127]. However, due to the introduction of a discrete lattice mesh, this may induce spurious dynamics due to the absence of perfect isotropy, when dealing with complex flows in complex boundaries [127]. Also, for multiphase/multicomponent models, the interface thickness is usually large and the density ratio across the interface is small when compared

with real fluids, such as the air/liquid interface. Therefore, a grid-free method is desirable to overcome these problems. SPH is a Lagrangian grid-free method for obtaining approximate numerical solutions of continuum equations [128, 129]. By interpolating flow properties over a discrete set of points, the macroscopic governing equations are discretized without the use of a spatial mesh. In contrast with complicated interface-tracking techniques in grid-based methods, the interfaces in SPH are naturally formed by the distribution of particles, regardless of the number of phases involved. However, in numerical computations using traditional SPH, several shortcomings are generally encountered, such as tensile instability, interpolation inconsistency, zero-energy mode, and difficulty in enforcing essential boundary conditions [130, 131].

DPD is another popular grid-free method, which incorporates thermal fluctuations. Compared with other mesoscopic methods, the DPD method is flexible for modeling different rigid structures by simply freezing DPD beads located inside the solid domain and letting them interact with fluid beads. Studies show that the DPD method can give equivalent or more accurate results in some simple flow problems, though taking much more time due to the calculation of thermal fluctuations [132]. One shortcoming of the DPD method is a lack of direct connection between model parameters and physical parameters of a system. Some efforts have been done for the connection of parameters, using kinetic and transport theories based on statistical mechanics [133–136]. A greater shortcoming of the DPD method is absence of physical scales at which a DPD simulation operates. Special efforts are needed to identify the scales of the simulation, which will be addressed in detail later.

To overcome these shortcomings in various numerical methods, a new mesoscopic method, known as Smooth Dissipative Particle Dynamics (SDPD), recently has been developed via the addition of thermal fluctuations into the SPH model [137]. The SDPD method is thermodynamically consistent and allows for a direct specification of transport coefficients. In spite of these attractive advantages over other methods, the applications of the SDPD method are still limited so far, because it is not capable of generating boundary conditions past surfaces [138, 139].

From the discussion above, in spite of the shortcomings for scaling, DPD is still a promising method due to the incorporation of thermal fluctuations and the capability to implement complex boundary conditions in a flexible way, as applied in many applications of complex fluids. These features make DPD a preferred choice over other mesoscopic numerical methods for the focuses in this work.

2.1.2 Governing equations of DPD

In DPD, the actual atoms or molecules are packed together by coarse-graining to form virtual beads. The motion of each DPD bead is governed by Newton's laws given by

$$\begin{aligned} \frac{d\vec{r}_i}{dt} &= \overrightarrow{v_i} \\ m_i \frac{d\vec{v}_i}{dt} &= \overrightarrow{f_i} = \sum_{i \neq j} (\overrightarrow{F_{ij}^C} + \overrightarrow{F_{ij}^D} + \overrightarrow{F_{ij}^R}) \end{aligned} \tag{2.1}$$

where $\overrightarrow{r_i}$, $\overrightarrow{v_i}$, and $\overrightarrow{f_i}$ denote the i^{th} bead's position, velocity, and the total force that acts on it, respectively. The interaction force between DPD beads is composed of three components, namely

conservative force $\overrightarrow{F_{ij}^C}$, dissipative force $\overrightarrow{F_{ij}^D}$, and random force $\overrightarrow{F_{ij}^R}$. The conservative force is responsible for thermodynamic behaviors of a DPD system, which is a repulsive force given as $\overrightarrow{F_{ij}^C} = a_{ij}\omega_c(r_{ij})\overrightarrow{e_{ij}}$, with weight function as [103]

$$\omega_c(r_{ij}) = \begin{cases} (1 - r_{ij}/r_c), & (r_{ij} < r_C) \\ 0, & (r_{ij} \geq r_C) \end{cases} \tag{2.2}$$

where a_{ij} is the repulsion force amplitude between bead i and j, $r_{ij} = |\overrightarrow{r_{ij}}|$, $\overrightarrow{r_{ij}} = \overrightarrow{r_i} - \overrightarrow{r_j}$, $\overrightarrow{e_{ij}} = \overrightarrow{r_{ij}}/r_{ij}$, and r_C is the cutoff radius. From this expression, the DPD potential can be obtained as

$$U(r_{ij}) = \begin{cases} \frac{a_{ij}r_C}{2}\left(1 - \frac{r_{ij}}{r_C}\right)^2, & (r_{ij} < r_C) \\ 0, & (r_{ij} \geq r_C) \end{cases} \tag{2.3}$$

which has a slope much shallower than the slope of the Lennard-Jones (L-J) potential commonly used in MD simulations (see Fig 2.2). The L-J potential is very well established, but it is difficult to apply a large time step due to the sharp increase of the potential at closer distance. This is the main motivation to design such a DPD potential with a much shallower slope as in Eq. (2.3), which overcomes the constraint of time step and allows a much larger time step than that used in MD simulations. Due to the lack of attraction, this DPD potential can only be used to simulate single phase flow, by matching the macroscopic properties of the system. Recently, some enhanced DPD methods incorporating both attraction and repulsion in the potential have been developed, and this will be introduced in the future Section 2.4.

The dissipative force is responsible for viscous effects due to relative velocity between each pair of DPD beads, and the random force acts like thermal fluctuations to account for the lost degrees of freedom during coarse-graining, as given by

$$\begin{aligned} \overrightarrow{F_{ij}^D} &= -\gamma\omega_D(r_{ij})(\overrightarrow{e_{ij}} \cdot \overrightarrow{v_{ij}})\overrightarrow{e_{ij}} \\ \overrightarrow{F_{ij}^R} &= \varphi\omega_R(r_{ij})\zeta_{ij}\Delta t^{-1/2}\overrightarrow{e_{ij}} \end{aligned} \tag{2.4}$$

where $\overrightarrow{v_{ij}} = \overrightarrow{v_i} - \overrightarrow{v_j}$, ω_D and ω_R, are weight functions for dissipative and random forces, respectively, ζ_{ij} is the Gaussian white noise with zero mean and unit variance, i.e., $\langle\zeta_{ij}\rangle = 0$ and $\langle\zeta_{ij}\zeta_{i'j'}\rangle = (\delta_{ii'}\delta_{jj'} + \delta_{ij'}\delta_{ji'})$, and γ and φ are amplitudes of dissipative and random forces, respectively. The factor $\Delta t^{-1/2}$ is included in the random force to make sure there is no dependence of the random force on the stepsize of integration [103]. To have a Gibbs canonical ensemble (NVT ensemble) for the steady state solution at equilibrium, Espanol et al. [134] demonstrated that the coefficients and weight functions in the dissipative and random forces have to satisfy the conditions

$$\begin{aligned} \omega_D(r_{ij}) &= [\omega_R(r_{ij})]^2 \\ \varphi^2 &= 2\gamma k_B T \end{aligned} \tag{2.5}$$

where k_B is the Boltzmann constant and T is the temperature of the system. This is the fluctuation-dissipation theorem (FDT) for the DPD method. The weight functions for the dissipative and ran-

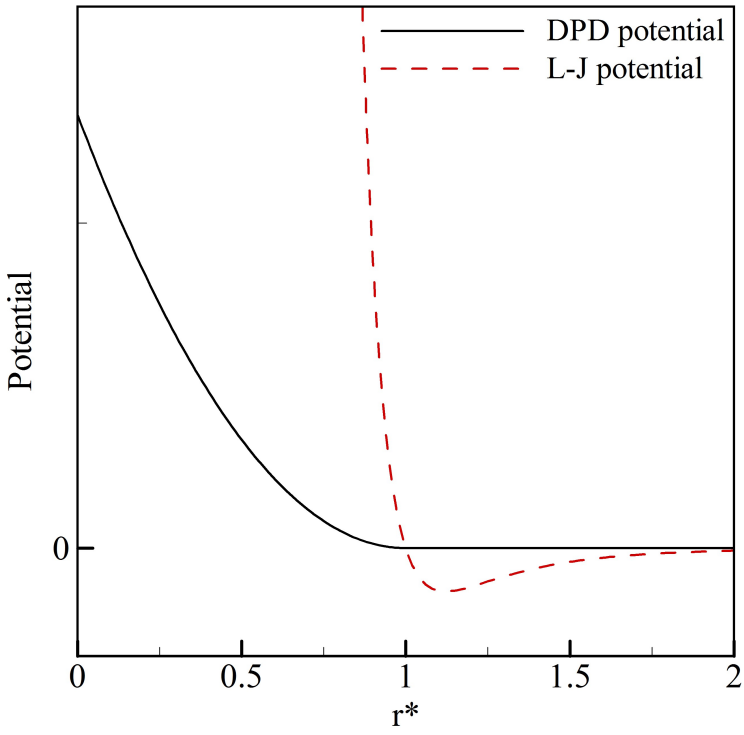

Figure 2.2: The comparison of DPD potential and Lennard-Jones (L-J) potential. $r^* = r/r_C$ for DPD and $r^* = r/\sigma_0$ for L-J potential. σ_0 is the distance at which the L-J potential reaches its minimum.

dom forces are taken to be

$$\omega_D(r_{ij}) = [\omega_R(r_{ij})]^2 = \begin{cases} \left(1 - \frac{r_{ij}}{r_C}\right)^2, & (r_{ij} < r_C) \\ 0, & (r_{ij} \geq r_C) \end{cases} \tag{2.6}$$

Due to the fact that each force is pairwise additive, conservation of momentum is satisfied naturally. On the other hand, the use of relative positions and velocities for the pairwise forces makes the DPD method fully isotropic. From the DPD equations of motion, the transport properties of a DPD fluid with specified simulation parameters, as well as the macroscopic conservation equations, can be derived systematically [133, 136, 140].

2.1.3 From DPD to Navier-Stokes equations

As mentioned in the previous subsection, the macroscopic conservation equations can be derived from the DPD equations of motion. The detailed derivation process is provided by Satoh and Majima [141]. A brief summary is given in this subsection to show that the solution obtained by the DPD method agrees well with that obtained from the Navier-Stokes equations.

By substituting the conservative, dissipative, and random force into Eq. (2.1), the set of Langevin equations for DPD beads can be obtained as

$$\begin{aligned}
&\frac{d\vec{r}_i}{dt} = \overrightarrow{v_i} \\
&m_i \frac{d\vec{v}_i}{dt} = \sum_{i\neq j} a_{ij}(1-\frac{r_{ij}}{r_C}) - \sum_{i\neq j} \gamma\omega_D(r_{ij})(\overrightarrow{e_{ij}}\cdot\overrightarrow{v_{ij}})\overrightarrow{e_{ij}} + \sum_{i\neq j}\varphi\omega_R(r_{ij})\zeta_{ij}\Delta t^{-1/2}\overrightarrow{e_{ij}}.
\end{aligned} \tag{2.7}$$

By integrating Eq. (2.7) over a small time interval from t to $t+\Delta t$, finite difference equations can be obtained as

$$\begin{aligned}
&\Delta\vec{r}_i = \overrightarrow{v_i}\Delta t \\
&\Delta\overrightarrow{v_i} = \frac{1}{m_i}\left(\sum_{i\neq j} a_{ij}(1-\frac{r_{ij}}{r_C}) - \sum_{i\neq j}\gamma\omega_D(r_{ij})(\overrightarrow{e_{ij}}\cdot\overrightarrow{v_{ij}})\overrightarrow{e_{ij}}\right)\Delta t + \frac{1}{m_i}\sum_{i\neq j}\varphi\omega_R(r_{ij})\overrightarrow{e_{ij}}\Delta W_{ij}
\end{aligned} \tag{2.8}$$

where $\Delta W_{ij} = \zeta_{ij}\sqrt{\Delta t}$.

To derive the macroscopic conservation equations, the Fokker-Planck equation for the DPD method needs to be introduced. The probability that a bead position and velocity are found within the range from $(\vec{r},\vec{v})$ to $(\vec{r}+\Delta\vec{r},\vec{v}+\Delta\vec{v})$ is denoted by $W(\vec{r},\vec{v},t)d\vec{r}d\vec{v}$, then the probability density function $W(\vec{r},\vec{v},t)$ satisfies the following stochastic formula, i.e., the Chapman-Kolmogorov equation

$$W(\vec{r},\vec{v},t) = \int\int W(\vec{r}-\Delta\vec{r},\vec{v}-\Delta\vec{v},t-\Delta t)\times\Psi(\vec{r}-\Delta\vec{r},\vec{v}-\Delta\vec{v};\Delta\vec{r},\Delta\vec{v})d(\Delta\vec{r})d(\Delta\vec{v}) \tag{2.9}$$

where $\Psi(\vec{r}-\Delta\vec{r},\vec{v}-\Delta\vec{v};\Delta\vec{r},\Delta\vec{v})$ is the transition probability for the state $(\vec{r}-\Delta\vec{r},\vec{v}-\Delta\vec{v})$ transferring to another state during a short time interval Δt, which does not depend on the time t. If the velocity $\vec{v}$ does not change appreciably during the short time interval Δt, then Ψ can be given as

$$\Psi(\vec{r}-\Delta\vec{r},\vec{v}-\Delta\vec{v};\Delta\vec{r},\Delta\vec{v}) = \psi(\vec{r}-\Delta\vec{r},\vec{v}-\Delta\vec{v};\Delta\vec{v})\delta(\Delta\vec{r}-\vec{v}\Delta t) \tag{2.10}$$

where ψ is the transition probability and is independent of $\Delta\vec{r}$. By substituting Eq. (2.10) into Eq. (2.9) and reforming the result in terms of Taylor series expansions with Eq. (2.8), the final result for the Fokker-Planck equation in phase space can be achieved as [142]

$$\begin{aligned}
&\frac{\partial W}{\partial t} + \sum_i \vec{v_i}\cdot\frac{\partial W}{\partial\vec{r_i}} + \sum_i\sum_j^{(i\neq j)}\frac{a_{ij}(1-\frac{r_{ij}}{r_C})\overrightarrow{e_{ij}}}{m_i}\cdot\frac{\partial W}{\partial\vec{v_i}} = \sum_i\sum_j^{(i\neq j)}\overrightarrow{e_{ij}}\cdot\frac{\partial}{\partial\vec{v_i}}\left\{\frac{1}{m_i}\gamma\omega_D(r_{ij})(\overrightarrow{e_{ij}}\cdot\overrightarrow{v_{ij}}W)\right\} \\
&+\frac{1}{2}\sum_i\sum_j^{(i\neq j)}\frac{1}{m_i^2}\sigma^2\omega_R^2(r_{ij})\times\overrightarrow{e_{ij}}\cdot\frac{\partial}{\partial\vec{v_i}}\left(\overrightarrow{e_{ij}}\cdot\frac{\partial}{\partial\vec{v_i}} - \overrightarrow{e_{ij}}\cdot\frac{\partial}{\partial\vec{v_j}}\right)W
\end{aligned} \tag{2.11}$$

For an arbitrary physical quantity $A(\vec{r},\vec{v})$, not dependent on time explicitly, the time average $\langle A\rangle$ can be obtained based on the probability density function W, given as

$$\langle A\rangle = \int\int AW(\vec{r},\vec{v},t)d\vec{r}d\vec{v} \tag{2.12}$$

where $\int\int AW(\vec{r},\vec{v},t)d(\vec{r})d(\vec{v}) = 1$. So from Eq. (2.11), the time variation of $\langle A\rangle$ can be expressed as

$$\frac{\partial}{\partial t}\langle A\rangle = \int\int A\Big\{\frac{1}{2}\sum_i\sum_j^{(i\neq j)}\frac{1}{m_i^2}\sigma^2\omega_R^2(r_{ij})\times\overrightarrow{e_{ij}}\cdot\frac{\partial}{\partial\vec{v_i}}\left(\overrightarrow{e_{ij}}\cdot\frac{\partial}{\partial\vec{v_i}}-\overrightarrow{e_{ij}}\cdot\frac{\partial}{\partial\vec{v_j}}\right)W-\sum_i\vec{v_i}\cdot\frac{\partial W}{\partial\vec{r_i}}$$
$$+\sum_i\sum_j^{(i\neq j)}\overrightarrow{e_{ij}}\cdot\frac{\partial}{\partial\vec{v_i}}\Big(\frac{1}{m_i}\gamma\omega_D(r_{ij})(\overrightarrow{e_{ij}}\cdot\overrightarrow{v_{ij}}W)\Big)-\sum_i\sum_j^{(i\neq j)}\frac{a_{ij}(1-\frac{r_{ij}}{r_C})\overrightarrow{e_{ij}}}{m_i}\cdot\frac{\partial W}{\partial\vec{v_i}}\Big\}d\vec{r}d\vec{v} \tag{2.13}$$

which can be simplified using integration by parts, as

$$\frac{\partial}{\partial t}\langle A\rangle = \Big\langle\sum_i\vec{v_i}\cdot\frac{\partial A}{\partial\vec{r_i}}-\sum_i\sum_j^{(i\neq j)}\frac{a_{ij}(1-\frac{r_{ij}}{r_C})\overrightarrow{e_{ij}}}{m_i}\cdot\frac{\partial A}{\partial\vec{v_i}}-\sum_i\sum_j^{(i\neq j)}\frac{\gamma}{m_i}\omega_D(r_{ij})(\overrightarrow{e_{ij}}\cdot\overrightarrow{v_{ij}})\overrightarrow{e_{ij}}\cdot\frac{\partial A}{\partial\vec{v_i}}$$
$$+\frac{1}{2}\sum_i\sum_j^{(i\neq j)}\frac{1}{m_i^2}\sigma^2\omega_R^2(r_{ij})(\overrightarrow{e_{ij}}\cdot\frac{\partial}{\partial\vec{v_i}})\times\left(\overrightarrow{e_{ij}}\cdot\frac{\partial}{\partial\vec{v_i}}-\overrightarrow{e_{ij}}\cdot\frac{\partial}{\partial\vec{v_j}}\right)A\Big\rangle. \tag{2.14}$$

Now, we are ready to derive the continuity equation and the momentum equation. If A is defined as

$$A = \sum_{i=1}^{N} m_i\delta(\vec{r}-\vec{r_i}) \tag{2.15}$$

then the average given from Eq.(2.12) is equal to a local density, as

$$\langle A\rangle = \left\langle\sum_{i=1}^{N} m_i\delta(\vec{r}-\vec{r_i})\right\rangle = \rho(\vec{r}). \tag{2.16}$$

By substituting Eq. (2.15) into Eq. (2.14), the whole equation can be simplified to

$$\frac{\partial\rho}{\partial t}+\frac{\partial}{\partial\vec{r}}\cdot(\rho\vec{u}) = 0 \tag{2.17}$$

which is the equation of continuity.

If A is defined as

$$A = \sum_{i=1}^{N} m_i\vec{v_i}\delta(\vec{r}-\vec{r_i}) \tag{2.18}$$

then the average given from Eq.(2.12) is

$$\langle A \rangle = \left\langle \sum_{i=1}^{N} m_i \vec{v_i} \delta(\vec{r} - \vec{r_i}) \right\rangle = \rho(\vec{r}) \vec{u}(\vec{r}). \tag{2.19}$$

where $\vec{u}(\vec{r})$ is the macroscopic fluid velocity at position $\vec{r}$. Then, by substituting Eq. (2.18) into Eq. (2.14), after simplification, the result can be obtained as

$$\frac{\partial}{\partial t}(\rho \vec{u}) = -\frac{\partial}{\partial \vec{r}} \cdot (\rho \vec{u} \vec{u}) + \frac{\partial}{\partial t} \cdot (\tau^K + \tau^U) \tag{2.20}$$

where

$$\begin{aligned} \tau^K &= -\langle \sum_i m_i (\vec{v_i} - \vec{u})(\vec{v_i} - \vec{u}) \delta(\vec{r} - \vec{r_i}) \rangle \\ \tau^U &= -\frac{1}{2} \left\langle \sum_i \sum_j^{(i \neq j)} (\overrightarrow{F_{ij}^C} + \overrightarrow{F_{ij}^D}) \overrightarrow{e_{ij}} \overrightarrow{e_{ij}} \int_0^{r_{ij}} \delta(\vec{r} - \vec{r_i} + \xi \overrightarrow{e_{ij}}) d\xi \right\rangle \end{aligned} \tag{2.21}$$

Based on Eq. (2.17), Eq. (2.20) can be reduced to

$$\rho \left(\frac{\partial \vec{u}}{\partial t} + \vec{u} \cdot \frac{\partial \vec{u}}{\partial \vec{r}} \right) = \frac{\partial}{\partial \vec{r}} \cdot (\tau^K + \tau^U) \tag{2.22}$$

where τ^K and τ^U are stress tensors due to the bead momentum and the forces between beads, respectively. Now, it has been demonstrated that the solution from the equation of motion in DPD is consistent with the solution from the momentum conservation law in macroscopic fluid mechanics.

2.1.4 Temporal integration

In the original DPD model developed by Hoogerbrugge and Koelman [102], the Euler scheme is used for the implementation of the equations of motion. Actually, more accurate schemes can be used for the temporal integration. However, this will lead to a great complexity and more iteration times for the forces at each time step, which is the main portion for computational time (consumes more than 50%). This will also lead to a great complexity for the coding and debugging. Therefore, although we have options for higher temporal accuracy, but they are not recommended to be used here. Based on the Euler scheme, the new velocities and positions at time $t + \Delta t$ are calculated based on information at time t, after which the forces at time $t + \Delta t$ are calculated based on the new velocities and positions, given as

$$\begin{aligned} \overrightarrow{r_i}(t + \Delta t) &= \overrightarrow{r_i}(t) + \Delta t \overrightarrow{v_i}(t) \\ \overrightarrow{v_i}(t + \Delta t) &= \overrightarrow{v_i}(t) + \Delta t \frac{\overrightarrow{f_i}(t)}{m_i} \\ \overrightarrow{f_i}(t + \Delta t) &= \overrightarrow{f_i} \left(\overrightarrow{r_i}(t + \Delta t), \overrightarrow{v_i}(t + \Delta t) \right) \end{aligned} \tag{2.23}$$

However, the Euler-type algorithm is not time reversible [143], since the probability to move one particle from $\vec{r_i}$ to $\vec{r_i} + \Delta\vec{r}$ is determined by the force acting on that particle at its initial position $\vec{r_i}$, but the probability to move one particle from $\vec{r_i} + \Delta\vec{r}$ to $\vec{r_i}$ is determined by the force acting on that particle at its initial position $\vec{r_i} + \Delta\vec{r}$. In MD simulations, a standard Verlet-style algorithm can be used for integration, such as the leap-frog scheme, satisfying time reversibility. In the leap-frog scheme, the velocities are defined at half the time interval, and the values for the next time step are calculated based on the positions at the previous time step, given as [143]

$$\begin{aligned}
\overrightarrow{v_i}(t + \frac{\Delta t}{2}) &= \overrightarrow{v_i}(t - \frac{\Delta t}{2}) + \frac{\overrightarrow{f_i}(t)}{m_i}\Delta t \\
\overrightarrow{r_i}(t + \Delta t) &= \overrightarrow{r_i}(t) + \overrightarrow{v_i}(t)\Delta t + \frac{\overrightarrow{f_i}(t)}{2m_i}(\Delta t)^2
\end{aligned} \tag{2.24}$$

In this implementation, the velocities at the intermediate time step are given by $\vec{v}(t) = \frac{1}{2}(\vec{v}(t - \Delta/2) + \vec{v}(t + \Delta/2)$, which means that the force term in Eq. (2.24) depends linearly on both $\vec{v}(t - \Delta/2)$ and $\vec{v}(t + \Delta/2)$. The velocity-Verlet scheme is time reversible and also simple enough to implement.

Unlike in the MD model, the forces in DPD depend on the velocities−to be specific, the dissipation force. To account for this complication, a modified velocity-Verlet integrator has been proposed by Groot and Warren [103]. The dissipative force is evaluated based on intermediate predicted velocities, instead of the old velocities at time t. The forces are still updated once during one time step, thus there is little increase in computational cost, with details given as [103]

$$\begin{aligned}
\overrightarrow{r_i}(t + \delta t) &= \overrightarrow{r_i}(t) + \delta t\overrightarrow{v_i}(t) + \frac{1}{2}(\delta t)^2\frac{\overrightarrow{f_i}(t)}{m_i} \\
\widetilde{v_i}(t + \delta t) &= \overrightarrow{v_i}(t) + \lambda\delta t\frac{\overrightarrow{f_i}(t)}{m_i} \\
\overrightarrow{f_i}(t + \delta t) &= \overrightarrow{f_i}\left(\overrightarrow{r_i}(t + \delta t), \widetilde{v_i}(t + \delta t)\right) \\
\overrightarrow{v_i}(t + \delta t) &= \overrightarrow{v_i}(t) + \delta t\frac{\overrightarrow{f_i}(t) + \overrightarrow{f_i}(t + \delta t)}{2m_i}
\end{aligned} \tag{2.25}$$

where λ denotes an empirical parameter. If the forces are independent of velocities, then actual velocity-Verlet scheme [144] would be recovered for $\lambda = 1/2$. The optimal value is found by Groot and Warren as $\lambda = 0.65$, though still empirical.

A thorough comparison of different integrators [145–147] has shown that the approaches above still exhibit systematic drift in temperature, but not pronounced with a short time step as 0.01 (dimensionless). Some other self-consistent approaches show better performance, but are more cumbersome to implement and time consuming. In later DPD studies, this modified velocity-Verlet integrator using Eq. (2.25) was widely applied, mainly due to its simplicity and sufficient accuracy and efficiency. Consequently, this study will adopt this approach as well.

Table 2.1: Conversion from reduced units to real units for Lennard-Jones argon [120]

Quantity	Reduced units	Real units
Length	$r^* = 1$	$r = 3.405 \times 10^{-10} m$
Temperature	$T^* = 1$	$T = 119.8K$
Density	$\rho^* = 1$	$\rho = 1680 kg/m^3$
Time	$\Delta t^* = 0.005$	$\Delta t = 1.09 \times 10^{-14} s$
Pressure	$P^* = 1$	$P = 41.9MPa$

2.1.5 Scaling from DPD units to physical units

In MD simulations, it is more convenient to use quantities in reduced (nondimensional) units for numerical implementation, such as temperature, density, pressure, and so on. With a convenient unit of energy, length and mass, all other quantities can be expressed in terms of these basic units [120]. There are two main advantages of using reduced units instead of real (SI) units in simulations. First, many combinations of density, temperature, length, and energy in real units may correspond to the same state in reduced units, by the principle of corresponding states. Second, the absolute numerical values of the quantities expressed in real units are either much less or much larger than one. This may create an overflow or underflow in numerical integration when several such quantities are multiplied together using standard floating-point multiplication. After simulations, results obtained in reduced units can always be converted back into real units, as one example for the simulation of Lennard-Jones argon shows in Table 2.1 [120].

Similarly, as a mesoscopic particle method, it will also be convenient to use a set of reduced units in the DPD simulations. The characteristic length and mass in the DPD simulations can be related to those in the MD simulations or other physical units with careful choice. As an example, a simple and direct scaling method from MD units to DPD units is first given as

$$m_{DPD} = n \cdot m_{MD} \tag{2.26}$$

where m_{DPD} is the mass of one DPD bead, m_{MD} is the mass of one molecule or atom in the MD scheme. Their ratio depends on coarse-graining level n, which means the number of molecules grouped into one DPD bead. By equaling the mass densities of MD and DPD system

$$\frac{m_{DPD} \cdot \rho_{bead}}{r_C^3} = \frac{m_{MD}}{r_{MD}^3} \tag{2.27}$$

the cut-off radius r_C can be determined as

$$r_C = \left(\frac{m_{DPD} \cdot \rho_{bead}}{m_{MD}} \right)^{1/3} r_{MD} \tag{2.28}$$

where ρ_{bead} is bead density (number density), which means the number of DPD beads inside unit volume r_C^3. r_{MD} is the radius of one molecule or atom in the MD scheme. After that, a time scale is also needed. By equaling viscosities (or some other key property for the specific study) of DPD

and MD fluids, t_{DPD} is determined as

$$t_{DPD} = \frac{\nu_{DPD}}{\nu_{MD}} \left(\frac{r_C}{r_{MD}} \right)^2 t_{MD} \tag{2.29}$$

where ν_{DPD} and ν_{MD} are kinetic viscosities of DPD and MD fluids respectively, t_{MD} is a characteristic time in the MD scheme.

After establishing a set of fundamental units, including mass, length, and time scale, other derived units can be built accordingly. However, to match a full set of physical properties for some specific problems remains a challenging task in DPD, such as one example given below from the work by Groot and Warren [103], discussing the compressibility and Schmidt number. In their study, the repulsion parameter is specially chosen to make sure the compressiblily of the liquid system is satisfied. However, with these parameters, the Schmidt number, characterizing the ratio of particle diffusion to momentum diffusion, is calculated to be $Sc = 1.00 \pm 0.03$, which is about three orders of magnitude lower than that of a real fluid [103, 135, 136].

In another work by Kumar et al. [148], by matching the density and viscosity of water and Reynolds number of the flow, they successfully obtain the hydrodynamics of water using $N_m = 10^7 - 10^9$, though having low diffusivity and high Schmidt number. Similar procedures have been used by many researchers to match the desired properties with experimental or physical values, such as dimensionless compressiblity [140, 149], diffusion constant [150], mechanical property [151], or material structure [152].

As for another concern regarding the upper limit for the coarse-graining level in the DPD method, it has been demonstrated by Füchslin et al. [153] that, the DPD method is scale-free for equilibrium systems by the usage of an appropriate scaling scheme for the usual DPD interactions as given in Eq. (2.1), Eq. (2.2) and Eq. (2.4). Two systems with different coarse-graining levels in DPD can be chosen in such a manner that the different physical systems represented by the reduced DPD dynamics share some physical properties, such as compressibility.

In this work, the simulation results will be represented in DPD units if there is no scaling methodology specified.

2.2 Boundary Conditions in DPD

As a particle model, the issue of boundary conditions has to be addressed in DPD scheme with special efforts, which is different from the implementation of boundary conditions in macroscopic computational fluid dynamics. Two main types of boundary conditions are periodic boundary conditions [120] and wall boundary conditions, modeled by different research groups in many different ways [154–164]. Recently, a symmetric boundary condition is also developed for DPD scheme [165]. The details for different implementation methods, especially for the no-slip wall boundary condition, are introduced in this subsection.

2.2.1 Periodic boundary condition

In particle-based simulation models, whether DPD or MD, the number of particles under simulation, even with the use of supercomputers, is still far away from the thermodynamic limit. In

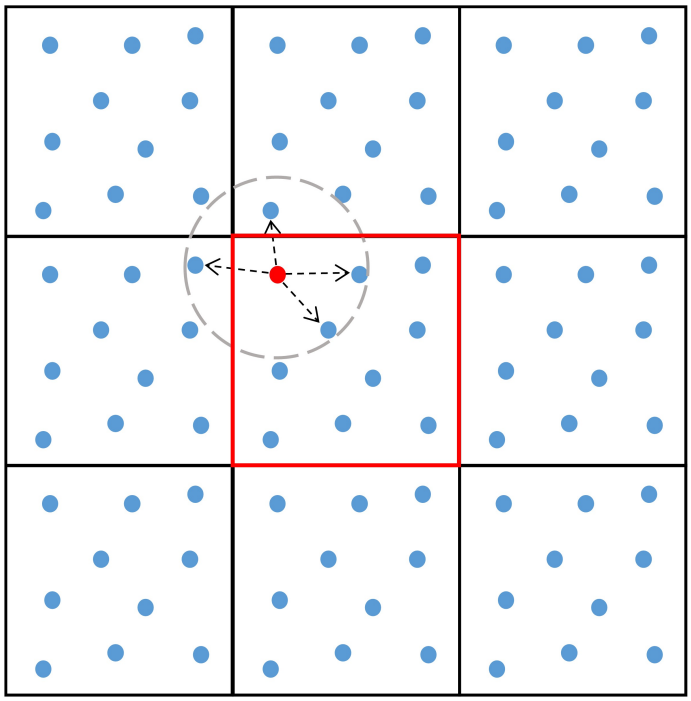

Figure 2.3: Schematic representation of periodic boundary condition in two-dimensional system. The particles in the middle (red) primitive cell can interact with with all other neighbor particles within cutoff radius in both primitive cell and neighbor cells.

order to simulate bulk phases, it is essential to apply boundary conditions that mimic the presence of an infinite bulk surrounding the simulation system with a limited number of particles. This objective is achieved by applying periodic boundary conditions, with the use of periodic mirror images (Fig. 2.3). In two dimensional situations, the native simulation cell is mirrored to all the eight neighbor cells (in three-dimensional, 26 neighbor cells), and a given particle can interact with all other neighbor particles within cutoff radius in both native cell and neighbor cells. Whenever a particle leaves the primitive cell during integration, it will enter the neighbor cell in that outgoing direction, and there is another particle entering the primitive cell from the opposite side, maintaining the total number of particles constant during the entire simulation.

Although the periodic boundary condition is an effective way to simulate homogeneous bulk systems, it may lead to spurious correlations not present in a truly macroscopic bulk system. One possible deficiency is, with the use of periodic boundary condition, only those fluctuations that have a wavelength shorter than the primitive cell dimension can be captured. Another deficiency is that the radial distribution function is not exactly isotropic for a system with high density [166].

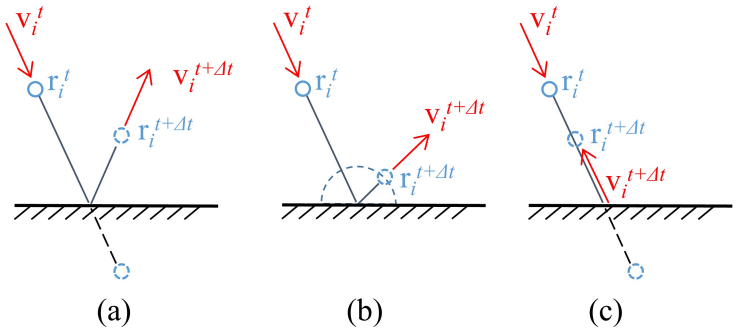

Figure 2.4: A comparison of reflection modes for fluid particles traversing through the solid wall: (1) Specular reflection; (2) Maxwellian reflection; and (3) Bounce-back reflection.

2.2.2 Wall boundary condition

One of the major factors determining the correctness of DPD simulation is the accurate implementation of physical boundary conditions. So far, significant research has been performed on the implementation of the commonly encountered solid wall boundary condition in flow systems. Lees-Edwards boundary condition can be used for simulating simple shear flow with a linear velocity profile [144]. However, this treatment is not applicable for more complex flow patterns or impenetrable boundaries, which requires real solid walls. Three conditions have to be satisfied for a real solid wall: (1) impenetrability, which means no particles are allowed to penetrate the wall; (2) no slip; and (3) the wall should not affect the fluid properties in the system.

Due to the soft interaction between DPD particles, it is difficult to prevent particles from penetrating a solid wall boundary by utilizing only the repulsive forces from wall particles. So, different reflection modes have been used to achieve the wall impenetrability by returning the particles traversing the solid boundary back into the fluid domain. Traditionally, three reflection modes have been proposed for particle methods [154]: (1) Specular reflection; (2) Maxwellian reflection; (3) Bounce-back reflection (see Fig. 2.4). In specular reflection, the normal component of the particle velocity is inverted, and the tangential component is unchanged. In Maxwellian reflection, the particles that penetrate the solid boundary are introduced back with a velocity following a Maxiwellian distribution centered around the wall velocity. In the bounce-back reflection, both the normal and tangential velocity are reversed. According to Revenga et al. [154], the specular and Maxwellian reflections produce an excessive slip velocity at the wall while the bounce-back reflection satisfies the no-slip condition. However, to satisfy the no-slip condition, a high wall density is required, which produces undesirable density distortions near the wall, affecting fluid behavior near the wall.

In later work by Visser et al. [158], an improved reflection mechanism has been designed to make the wall impenetrable without causing side effects (see Fig. 2.5). By a thorough analysis of the bounce-back method, they found that the no-slip action solely relies on the velocity treatment and perpendicular positioning to the wall. So in their method, the displacement tangential to the wall during a reflection is preserved, while the position perpendicular to the wall and the velocity

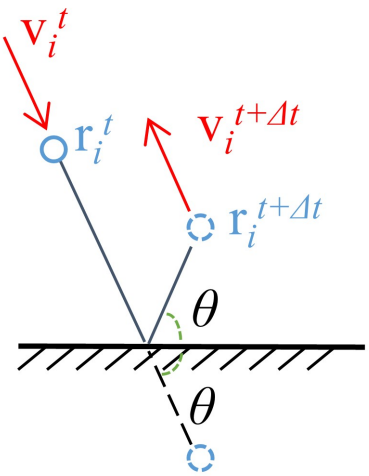

Figure 2.5: Bounce-forward reflection for a particle i that jumps out of the solid boundary in a time step Δt.

change is same as the original bounce-back reflection method. In this "bounce-forward" method, the unrealistic accumulation of particles in the corner is canceled.

Some other new boundary conditions have also been developed based on different techniques, such as combination of bounce back and Maxwellian reflections [159], addition of a weak external repelling force on liquid particles penetrating the solid boundary [160] or construction of probability distribution functions of different DPD force components [161]. Though the density fluctuations near the solid boundaries is well controlled, the complexity for these new methods requires more effort for the implementation of complex geometry. In the new boundary condition designed by Ranjith et al. [163, 167], fixed wall particles are no longer used. Instead, the wall interacts with each fluid particle within the cut-off radius r_C as if there is a wall particle on the boundary located at the shortest distance from the fluid particle (see Fig. 2.6). These "instantaneous frozen particles (IFP)" appear on the boundary at each time step and disappear after interactions with each corresponding fluid particle. With fewer wall particles to be considered, this method is computationally more efficient than other previous boundary methods. By tuning the lateral dissipation (friction) between the fluid particles and their corresponding IFP, no slip or controllable slip boundary conditions can be obtained.

2.2.3 Symmetric boundary condition

A very common boundary condition for the simulation of macroscopic fluid systems is symmetric boundary condition. The application of symmetric boundary condition (SBC) allows for modeling only a part of the system, e.g., one half or one quarter, thus significantly reducing computer memory requirement and computational time. For instance, for Poiseuille flow between two

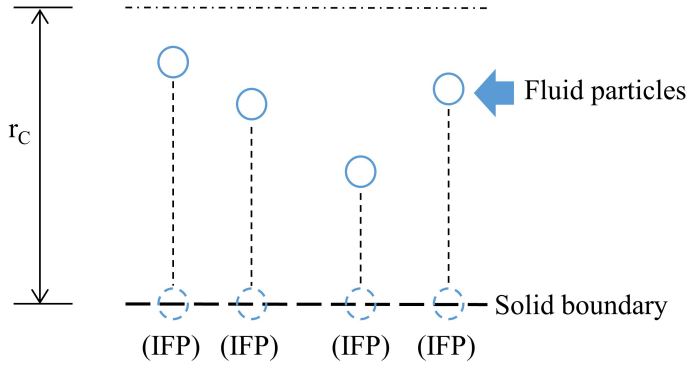

Figure 2.6: Each fluid particle within cut-off radius r_C interacts with its corresponding IFP. The size of IFP is that of the fluid particle, its angular velocity is zero, and its linear velocity is that of a solid wall [163].

parallel plates, the resulting flow field is symmetric with respect to the central plane between the two plates.

In our recent study [165], a numerical scheme for the implementation of the symmetric boundary condition is proposed using a combination of ghost particles and specular reflection method (see Fig. 2.7). A layer of ghost particles is introduced, which is just the mirror image of the layer of real fluid particles above the boundary. In this way, the particle distribution becomes exactly symmetric in a region on both sides of the symmetric boundary. Specular reflection method is used whenever the penetration into the symmetric boundary occurs. The results demonstrate that this method can accurately reproduce the system properties, such as shape, velocity, and viscosity of a full system by simulating just a subsystem. By reducing the original full system one to half, or even quarter in some cases, significant savings in computation time is achieved.

2.3 Validation Case 1 – Poiseuille flow

Poiseuille flow is a benchmark case for traditional computational fluid dynamics (CFD) modeling and validation case. It is also a good candidate for code validation of the DPD scheme, which as well demonstrates the capability of DPD for typical problems solved by Navier Stokes solvers on grid methods previously. The first study for Poiseuille flow in DPD has been tested by Fan et al. [168], where the DPD fluids are found to behave just like a Newtonian fluid in three-dimensional computational domain, and the quadratic velocity profile matches excellently with the analytical solution. The following studies have compared their results with that and showed a good agreement as a validation in three-dimensions [169], and even two-dimensions [148]. In the DPD method, liquid viscosity is not a direct input parameter, but has to be obtained from necessary derivations. However, based on the studies on static and dynamic fluid properties in DPD [135, 136, 141], the theoretical prediction for viscosity should be different when in two-dimensional and three-dimensional configurations applying the same set of simulation parameters and weight functions. So, the maximum

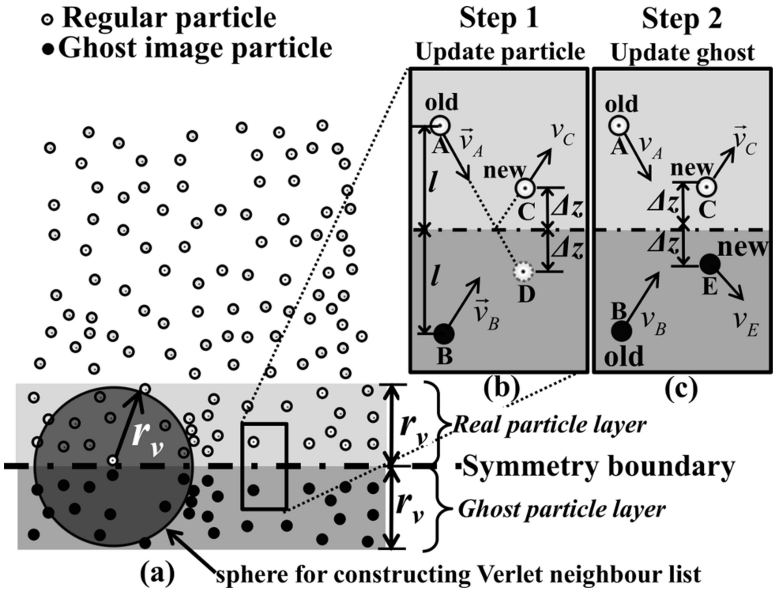

Figure 2.7: Schematic representation of Symmetric boundary condition [165]. (a) The configuration of DPD particles and their ghost images are presented. The real particle layer and ghost particle layer are marked; (b) the specular reflection mechanism for updating fluid particle position is illustrated; and (c) the updating mechanism for ghost particle position.

velocity for Poiseuille flow using the same parameters should be different in 2D and 3D simulations according to different predictions for viscosity, which have been applied successfully in other 2D [143] and 3D [168] DPD simulations. So far, there is still no study to include both 2D and 3D simulations in one work and compare the difference.

In the following subsections, the Poiseuille flows in both 2D and 3D configurations are studied to analyze the difference and relation between 3D and 2D simulations in DPD. Reduced units are used for DPD in a standard way, i.e., length in r_C, energy in k_BT and mass in m of single DPD bead.

2.3.1 Poiseuille flow in 3D configuration

To validate the code for the Poiseuille flow first, the computational domain used by Fan et al. [168] is applied for the simulation (see Fig. 2.8). The fluid domain is set as $-30 < x < +30$ and $-1.5 < y < +1.5$, and periodic boundary condition is applied in both the x direction and the y direction. For the z direction, the two walls are located at $z = \pm 15.25$. The bounce-forward

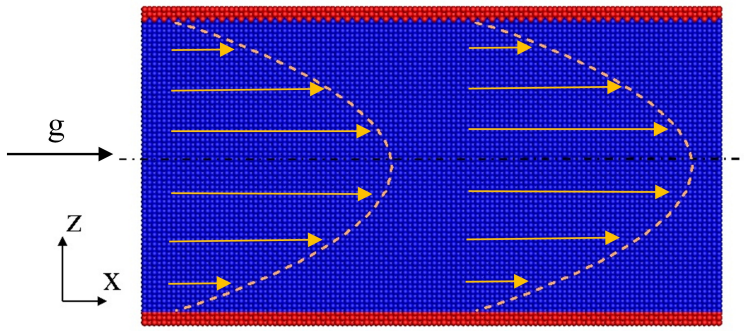

Figure 2.8: Computational setup for Poiseuille flow

reflection boundary condition is applied to obtain a no-slip wall boundary [156–158]. The gravity force in x direction or the external body force $g = 0.02$ is applied to each fluid bead to mimic the pressure-driven flow. The bead density is chosen as $\rho_{bead} = 4$, leading to a unity period of the face-centered-cubic (fcc) lattice. To satisfy the compressibility of water [103], the coefficient of the conservative force for interaction between liquid beads should be

$$a_{ij} = 75k_BT/\rho_{bead} \tag{2.30}$$

Then $a_{ij} = a_{ll} = 18.75$, $\varphi = 3$ with $\lambda = 0.5$ in the velocity Verlet scheme when $\Delta t = 0.02$. Subscripts l and w represent the liquid and wall beads, respectively. The coefficient of the conservative force between wall beads is $a_{ww} = 5.0$, thus leading the force parameter between liquid bead and wall bead to be $a_{lw} = \sqrt{a_{ll} \cdot a_{wwl}} = 9.68$.

For the Newtonian fluid, the velocity profile is known to be quadratic, where the maximum velocity happens in the center of the channel

$$u(z) = u(0)[1 - (\frac{z}{h})^2], \qquad u(0) = \frac{\rho_{bead} g h^2}{2\mu_{3D}} \tag{2.31}$$

where h is the half channel width $h = 15.25$, and μ_{3D} is the viscosity of fluid in 3D, which can be obtained as [103, 135, 136]

$$\mu_{3D} = \frac{45k_BT}{4\pi\gamma r_C^3} + \frac{2\pi\gamma\rho_{bead}^2 r_C^5}{1575} \tag{2.32}$$

where the first term is kinetic contribution and the second term comes from the dissipative contribution, with the contribution from conservative forces neglected. Based on the parameters given above, the viscosity of fluid should be $\mu_{3D} = 1.077$ from Eq. (2.31), thus leading to the maximum velocity to be $u_{max} = 8.63$.

To get the velocity profile, the simulation runs for 130,000 time steps to make sure the the flow reaches steady state, after which 20000 more time steps are taken to perform the temporal

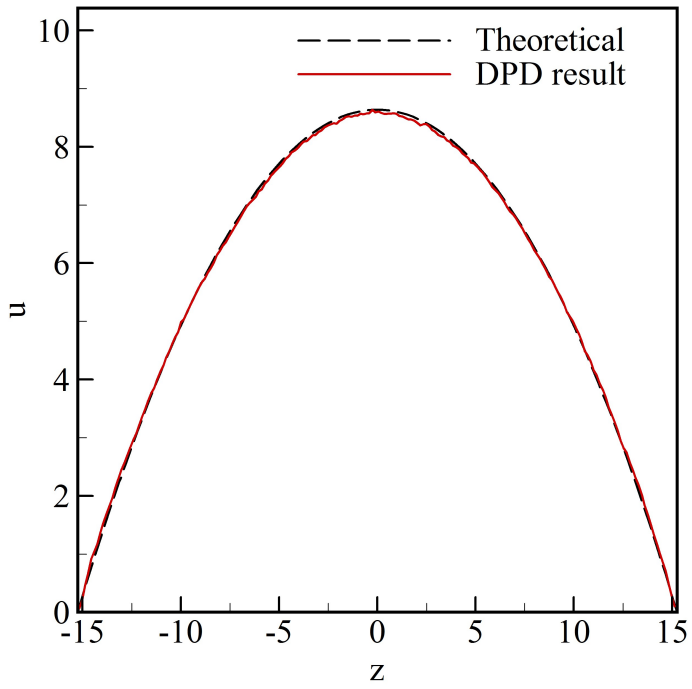

Figure 2.9: Velocity profiles for 3D Poiseuille flow by theoretical prediction and DPD simulation

averaging to get rid of the random effect. Besides that, to get the Eulerian velocity distribution from the lagrangian system, the region is divided into 300 bins in z direction, 60 bins in x direction, and 3 bins in y direction to perform spatial averaging, since the velocity variation mainly happens in z direction. The beads located at each individual cubic unit are summed and then averaged to get the velocity vector for that unit. Then, the velocity profile along z direction is obtained by extracting at the center of x direction and averaging over y direction, as shown in Fig. 2.9. The result from the simulation is in good agreement with theoretical prediction, though it still exhibits slight fluctuations. The maximum velocity by simulation is 8.60, which is less than a 1% difference from the theoretical value, thus validating the algorithms and implementation of the in-house program.

2.3.2 Poiseuille flow in 2D configuration

As mentioned above, some previous studies claimed that they regenerated the 2D simulation result to be the same as the 3D simulation using the same parameters. However, based on earlier theoretical work [135, 136, 141], the viscosity of fluid in 2D from statistical analysis should be

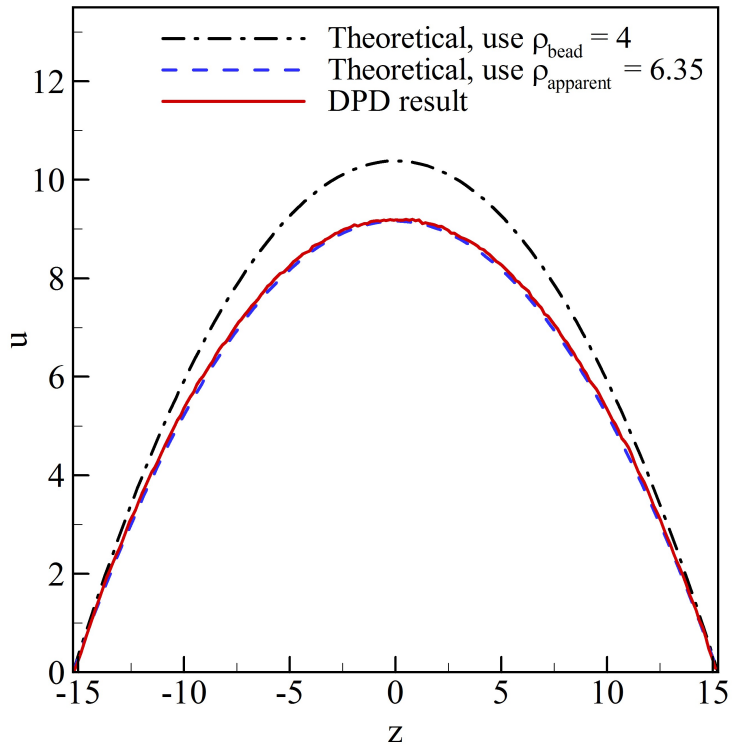

Figure 2.10: Velocity profiles for 2D Poiseuille flow by theoretical prediction and DPD simulation

different from the expression in 3D, which is given as

$$\mu_{2D} = \frac{6k_BT}{\pi\gamma r_C^2} + \frac{\pi\gamma\rho_{bead}^2 r_C^4}{480} \tag{2.33}$$

when the same weight functions for conservative forces are used. With the parameters given in the previous subsection, the viscosity of fluid in 2D is $\mu_{2D} = 0.896$ by Eq. (2.33). So, a maximum velocity of 10.39 is expected from Eq. (2.31), which is larger than that in the previous subsection.

Using the same parameters, the 2D simulation result is shown in Fig. 2.10. The maximum velocity from simulation is 9.18, which is far below the theoretical prediction represented by the black dash dotted line. The reason for this discrepancy is that the apparent density in 2D simulation is not 4, as the number directly means. The $\rho_{bead} = 4$ in 3D and 2D simulations has different physical meanings, since one means 4 DPD beads in unit volume r_C^3, and the other means 4 DPD beads in unit area r_C^2, which is more dense.

To have a reasonable comparison and conversion between density in 3D and 2D simulation, the bead density in each dimension should be same. Since the beads are arranged in fcc lattice, which has 4 entire beads in unit volume r_C^3, the 2D bead density can be converted to apparent

density in 3D following

$$\frac{\rho_{apparent}}{\rho_{fcc}} = \frac{\rho_{2D}}{\rho_{fcc}^{2/3}} \tag{2.34}$$

where ρ_{fcc} is 4 as discussed above. In this way, the apparent density should be $\rho_{apparent} = \frac{\rho_{fcc}}{\rho_{fcc}^{2/3}} \cdot \rho_{2D} = 6.35$. By substituting this number into Eq. (2.33) and Eq. (2.31), a new prediction result can be achieved, per the blue solid line shown in Fig. 2.10, which almost overlaps with the simulation result.

From these results, the simulations results in both 3D and 2D configurations are validated, with the introduction of apparent density.

2.4 Validation Case 2 – Droplet driven by wettability gradient

After the validation of Poiseuille flow simulations, a moving droplet driven by the wettability gradient is studied as a second case for validation for two reasons. First, the many-body DPD (MDPD) scheme, which is designed to model liquid-air interfaces, will be introduced and validated in this simulation. Second, the manipulation of a droplet will serve as a prerequisite case for our ultimate goal, manipulation of microparticles by a droplet. To initiate the motion of the droplet, the wettability of the wall is specially designed to change from hydrophobic to hydrophilic. Here, the "hydrophobic" refers to the physical property of a substance that is seemingly repelled from a mass of water, and the "hydrophilic" refers to the physical property of a substance that tends to be attracted to a mass of water. So, the droplet will move from hydrophobic end to hydrophilic end due to the wettability gradient, which is the mechanism for droplet manipulation in EWOD as well as other experimental studies with permanent surface coatings [24, 170]. By setting two neighbor electrodes with different voltages, the droplet in contact with both electrodes will be actuated towards the more hydrophilic side. In the following, the governing equations of MDPD scheme will be introduced in the first subsection. Then, a surface with wettability gradient will be specially designed. After these, the motion of droplets will be simulated and compared with theoretical approximations.

2.4.1 Governing equations of MDPD

The main advantage of the DPD method is the adoption of soft repulsive potentials, which is in contrast to the common use of interaction potentials with hard cores in molecular dynamics. However, the DPD method with repulsive force only is not applicable to free surface fluid dynamics problems, such as wetting, spreading, and capillary problems. To capture vapor-liquid coexistence, MDPD has been developed, which uses both repulsive and attractive conservative forces between beads [171]. The vapor-liquid interface can be formed by using different cut-off radius for attractive and repulsive forces. Another model simulating phase segregation based on mean-field theory has also been used to generate an equation of state with a van der Waals loop [119]. Using MDPD, surface tension calculations have shown good agreement with atomistic simulations [117, 160, 172–174]. The dynamic wetting process has also been simulated with different constructions of the conservative force and wall model [82, 117, 160, 173].

To capture the free surface fluid dynamics problem, Warren [171] has proposed a new conservative force including both attractive and repulsive components instead of purely repulsive force in standard DPD, given as

$$\overrightarrow{F_{ij}^{C}} = \left[A_{ij} \cdot \omega_C(r_{ij}) + B_{ij} \cdot (\overline{\rho_i} + \overline{\rho_j}) \cdot \omega_d(r_{ij})\right] \overrightarrow{e_{ij}} \tag{2.35}$$

where the repulsive part $B_{ij} \cdot (\overline{\rho_i} + \overline{\rho_j}) \cdot \omega_d(r_{ij})$ depends on a weighted average of bead density, while the attractive part $A_{ij} \cdot \omega_C(r_{ij})$ is density independent. The A_{ij} and B_{ij} are the amplitudes of attractive and repulsive forces, respectively. The values of A_{ij} are negative and the values of B_{ij} are positive. The weight function $\omega_c(r_{ij})$ is same as Eq. (2.2), and $\omega_d(r_{ij})$ is in a similar form as

$$\omega_d(r_{ij}) = \begin{cases} (1 - r_{ij}/r_d), & (r_{ij} < r_d) \\ 0, & (r_{ij} \geq r_d) \end{cases} \tag{2.36}$$

where r_d is a cut-off radius for the repulsive component, set to be a shorter range than r_c. The density for each bead $\overline{\rho_i}$ is defined as

$$\overline{\rho_i} = \sum_{j \neq i} \omega_\rho(r_{ij}) \tag{2.37}$$

where weight function ω_ρ vanishes for $r > r_d$. For convenience, it is normalized so that $\int \omega_\rho(r_{ij}) dV = 1$, where V is volume. The weight function is given as

$$\omega_\rho(r_{ij}) = \begin{cases} \frac{15}{2\pi r_d^3}(1 - r_{ij}/r_d)^3 & \text{three dimensional} \\ \\ \frac{12}{2\pi r_d^2}(1 - r_{ij}/r_d)^2 & \text{two dimensional} \end{cases} \tag{2.38}$$

2.4.2 Design of wettability gradient

A droplet on a surface can be moved by the wettability gradient of the surface, which means gradient of surface energy along the surface or explicitly refers to the contact angle variation along the surface. For experimental designs, to induce wettability gradient and move the droplet by electrowetting (EWOD), a difference in the applied voltage on neighbor electrodes is needed. In the pioneering work by Cho et al. [23], the applied voltage is 25V and the contact angle changes from 117° to 90° over a distance of $154\mu m$. In recent works [46, 49], the applied voltage is 62.5V and the contact angles ranges from 160° and 50°. In some other numerical works [175], the contact angle applied to drive the droplet ranges from 20° to 120°.

In the present work, the range of contact angle is chosen as from 150° to 40°, corresponding to a voltage of 63V based on the design by Jönsson-Niedziółka et al. [49]. In the MDPD method, to have a wettability gradient on the wall, or a difference in contact angle along the wall, interaction parameters between liquid and solid wall can be adjusted accordingly along the wall. After fixing the repulsion parameter for liquid wall interaction B_{lw}, the static contact angle θ depends solely on the attraction parameter for liquid wall interaction A_{lw}, and the relation between them needs to be established first.

Table 2.2: Computational parameters for calculation of contact angle

Parameter	Symbol	Value
Fluid bead density	ρ_{bead}	6.00
Attractive force range	r_c	1.00
Repulsive force range	r_d	0.75
Amplitude of random force	φ	6.00
Amplitude of attractive force	A_{ll}	−40.00
Amplitude of repulsive force	B_{ll}	25.00
Amplitude of repulsive force	B_{lw}	25.00
Time step	Δt	0.01

To measure the solid-liquid contact angle at certain A_{lw}, one way is to extract it from a meniscus shape. Liquid beads are initially positioned inside a rectangular cube between two parallel infinitely large plates and then form a stable meniscus shape after equilibrium. The whole computational domain is 40 by 40 by 40 (dimensionless length). The 128,000 liquid beads fill the whole domain in the y and z directions, and occupy the middle half in the x direction. A periodic boundary condition is applied in the y direction. To avoid penetration of liquid beads, bounce-back reflection is used for the wall, which is constructed by three frozen layers of wall beads. The interaction parameters between liquid beads are shown in Table 2.2 [82, 117, 171]. B_{ll} represents the repulsion between liquid (l) and liquid (l) beads, while B_{lw} represents the repulsion between liquid (l) and wall (w) beads. Reduced units are used for DPD in a standard way, i.e., length in r_c, energy in k_BT, and mass in m.

To extract the contact angle from the equilibrium shape, the bead density is calculated and selected to extract the outer layer of the shape, as one representative case shows in Fig. 2.11a. The bead density, ranging from 6 to 7, mainly distributes at the inner region, and the bead density gradually reduces to the range of 4 to 6 while approaching the outer surface. So the bead density raging from 4 to 6, which is shown in green in Fig. 2.11b, can be used to extract the contact angle. The top and bottom layers of these selected beads are removed, and only the curvature part is used to find the best fit circle and contact angle, including about 20% of the total liquid beads. In this way, the contact angle using the different liquid wall interaction parameter A_{ls} can be obtained.

Another way to get the contact angle is to use the sessile droplet method (see Fig. 2.12), which means capturing the profile of a pure liquid droplet on a solid substrate. The initial setup is a spherical droplet merely in contact with a solid wall. Periodic boundary conditions are applied in both x and y directions parallel to the wall. Bounce-back reflection is also used for the wall. Due to the attraction between solid liquid beads, the droplet will attach to the wall and finally form a stable shape on it. After that, a similar approach used in the meniscus case can be applied here to extract the contact angle by detecting the boundary shape from bead density distribution.

By applying the same parameters in Table 2.2, a comparison of contact angle between sessile droplet and meniscus can be obtained. A droplet of radius 12 is simulated for 20,000 time steps and then sampled for every 2,000 time steps. By averaging 20 samples, the contact angle for A_{lw} is calculated to be 143.43°. Using the meniscus simulation, the contact angle for $A_{lw} = -10.00$ is

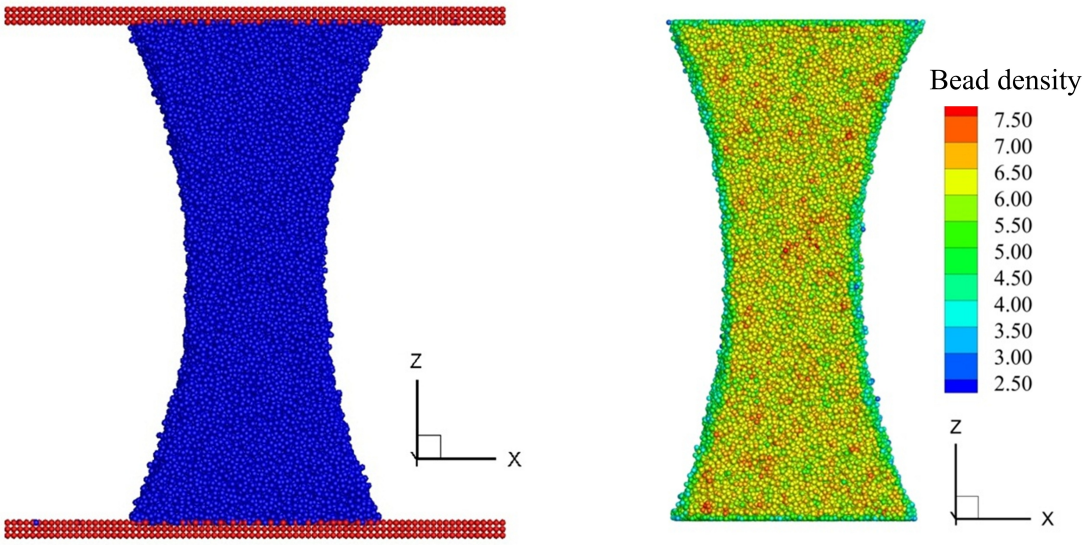

(a) (b)

Figure 2.11: The meniscus between two parallel walls: a) meniscus shape after reaching the equilibrium state-water beads are in blue and solid wall in red; b) bead density distribution inside the meniscus.

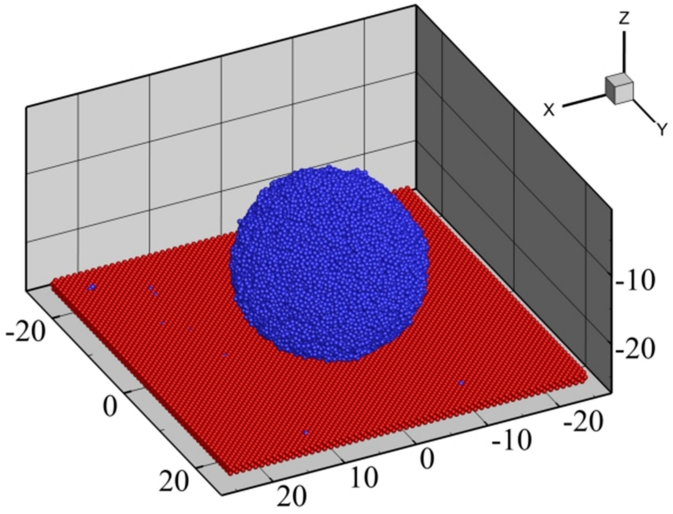

Figure 2.12: Computational configuration for a sessile droplet on a solid wall

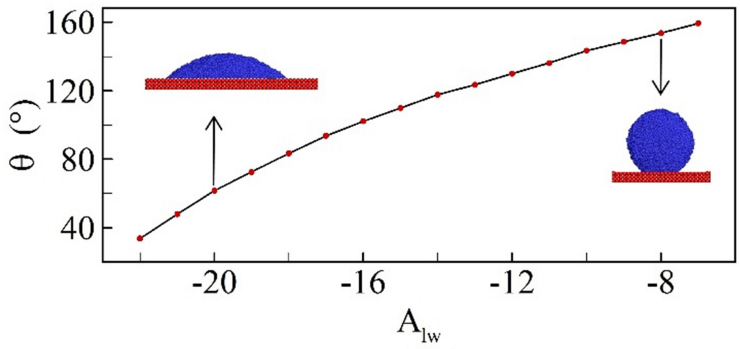

Figure 2.13: Relation between static contact angle θ and liquid wall interaction parameter A_{lw}; error bar is not shown since the standard error is always less than 1%.

140.53° after averaging 20 samples. These 20 samples are also sampled for every 2000 time steps after the 10000 time steps needed for the equilibrium of the meniscus shape. From the comparison between these two methods, there is only 2% difference in the measurement of contact angles. So this matched result validates the implementation for the meniscus simulation and contact angle calculation. This 2% difference can be further reduced by taking more samples from more time steps, since it is a statistical method. Another way to reduce the error is use more beads in a larger computational domain. Both will improve the accuracy for the result, but at the same time increase the computational time.

After the method for contact angle calculation is validated, the relation between static contact angle θ and attraction parameter for liquid wall interaction A_{lw} can be established by a series of simulations using the sessile droplet with different A_{lw}. The results are shown in Fig. 2.13, as 20 measurements are repeated and averaged for each value. Once the relation is known, we can change the wettability of the wall from hydrophobic to hydrophilic gradually, by tuning A_{lw} along the wall surface in x direction. A location-dependent A_{lw} is specially designed to make contact angle θ change linearly with x position, expressed as

$$A_{lw} = \begin{cases} 8.765 & x < x_0 \\ -1.211 - \sqrt{552.125 - 3.30033 \times \theta_0 + 3.300 \times \frac{\theta_0 - \theta_f}{x_f - x_0}(x - x_0)} & x_0 \le x \le x_f \\ 21.707 & x > x_f \end{cases} \tag{2.39}$$

where x_0 and x_f are the initial position (hydrophobic end) and final position (hydrophilic end) of the region with wettability gradient, θ_0 and θ_f are static contact angles at x_0 and x_f respectively. A droplet is dropped at x_0, and will move in x direction to x_f in the end, due to the unbalanced surface energy caused by the wettability gradient [176–178].

Table 2.3: Scaling between nondimensional MDPD units and physical units for the manipulation of droplets

Variable	Symbol	MDPD system	Physical value
length	r_c	1.0	$10.0\mu m$
mass	m_{MDPD}	1.0	$7.0 \times 10^{-13} kg$
surface tension	γ	7.53	$0.073 N/m$
time	t	1.0	$8.5\mu s$

2.4.3 Results and validation

After the preparation of the wall surface with a wettability gradient, a droplet of radius 10 is simulated to study the motion driven by a linear wettability gradient as given by Eq. (2.39) (see Fig. 2.14). The initial and final positions of the wettability gradient region are chosen as $x_0 = -40$ and $x_f = +40$. The contact angles at these two locations are $\theta_0 = 150°$ and $\theta_f = 40°$. Other parameters are the same as those given in Table 2.2. The simulation is conducted by using a constant $A_{lw} = -8.765$ for the first 20,000 time steps, in order to have the droplet reach equilibrium state from the initial lattice arrangement. After that, the linear wettability gradient is applied, and the simulation is continued for another 300,000 time steps, which is enough for the droplet to travel the whole path.

In experiments, the typical range for a droplet size to be studied in digital microfluidics is from 3 nl to 3 μl, or even larger [179]. Also, the typical range for gap distance between electrodes in digital microfluidics is from 150 μm to 1.5 mm [179]. To match with experimental works, the unit length in simulations is set to $10\mu m$, thus the volume of the droplet is $4.19nL$. The region of wettability gradient is $800\mu m$ long, which corresponds to the physical value of the gap between two neighbor electrodes with different voltages. To match the density and surface tension of water, the unit mass is $7.0 \times 10^{-13} kg$ and the unit time is $8.5\mu s$. So, the wettability gradient in Eq. (2.39) corresponds to a voltage of 63V over a distance of 800 micrometer. The summary for the scaling between nondimensional MDPD units and physical units is shown in Table 2.3.

The time history of the droplet center is shown in Fig. 2.15. The position of the droplet center is recorded for every 10 time steps, corresponding to every 0.1 time unit. It takes about 1800

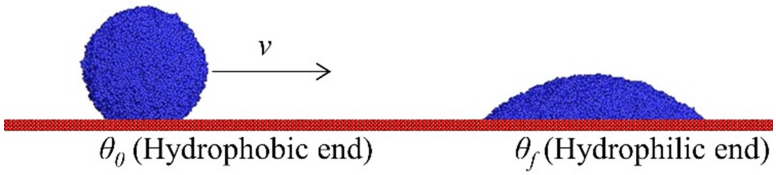

Figure 2.14: Motion of liquid droplet on a substrate with wettability gradient

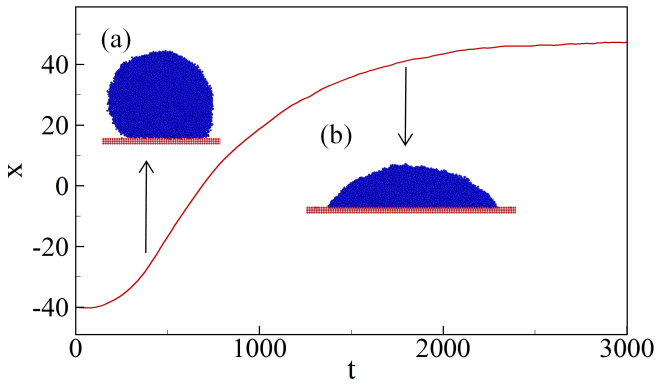

Figure 2.15: Time history of the position of droplet

DPD time units to travel from hydrophobic end to hydrophilic end, as the velocity of the droplet increases first and decreases after it reaches about $x = 10$. As the droplet moves, it spreads out from a spherical shape to a wide cap.

To validate the numerical method for obtaining the droplet velocity, a series of cases are simulated for a droplet at different local equilibrium contact angles. The wettability gradient (WG) is set as a constant $WG = \frac{\Delta\theta}{\Delta x} = \frac{\theta_0-\theta_f}{x_0-x_f} = \frac{150-40}{(-40)-40} = -\frac{11}{8}$. Based on the wedge approximation of Subramanian et al. [180], the droplet velocity can be predicted according to the equilibrium contact angle at different locations as:

$$U = \frac{\gamma R\theta_e^2}{6\mu \ln(2\epsilon)} \frac{d\theta_e}{dx} \tag{2.40}$$

where γ is liquid-gas interfacial tension, R is the radius of the droplet footprint, θ_e is the equilibrium contact angle, and ϵ represents the ratio of the length of the slip region to the radius of the footprint of the droplet. To examine the overall velocity of the moving droplet from simulations, the thermal fluctuation in velocity has to be removed from the transient numerical results. A post-processing method using quasi-stationary state can be applied, proposed by Li et al. [82]. In this method, the droplet is forced to move at a constant speed without changing shape. This is implemented by applying and keeping a fixed wettability gradient on the moving droplet. The position of the droplet is recorded, and the wettablity gradient moves at the same pace as the droplet to maintain this quasi-stationary state. The slope of the trajectory represents the overall velocity of the moving droplet.

The comparison of droplet velocity obtained by wedge approximation and numerical simulation is shown in Fig. 2.16, where 5 measurements are repeated and averaged for each value obtained from the above-mentioned quasi-stationary method. Both numerical results and theoretical approximations show a decreasing velocity. The theoretical approximation is always higher than

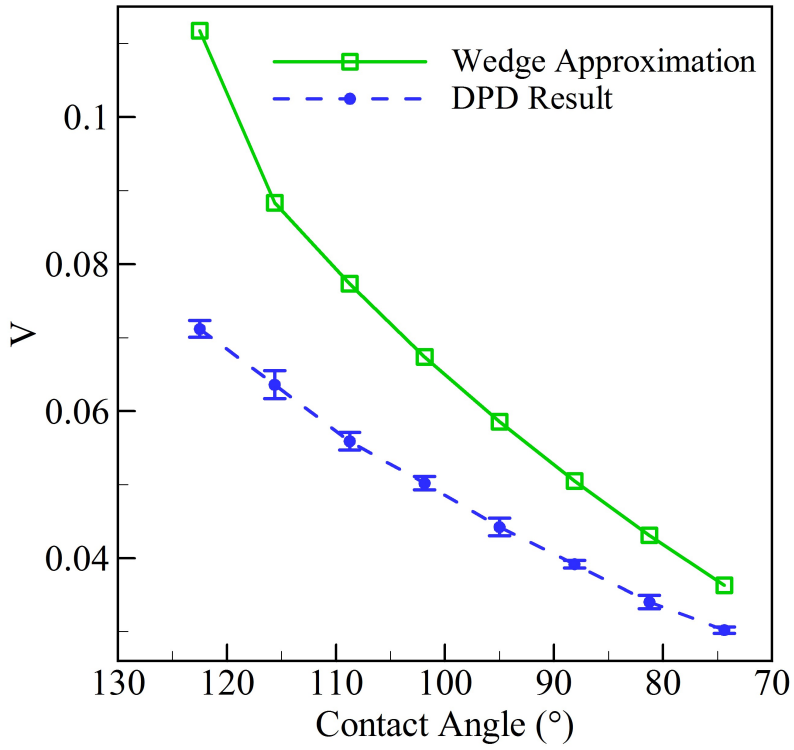

Figure 2.16: Comparison of droplet velocity at different equilibrium contact angles.

the numerical simulation, but their difference diminishes as θ_e decreases. The observed differences between the simulation and prediction are the result of several factors. First, the theoretical prediction is approximate since the governing equations for the driving force and viscous force are not solved based on a complete numerical solution. As noted by Subramanian et al. [180], an exact solution should predict a larger resistance than the value based on wedge approximation, which would reduce the difference between simulation and theoretical results. Second, in the wedge approximation, the shape of the droplet is assumed to be a spherical cap, and the footprint is assumed to be a circle. However, the shape in simulation can be affected by hydrodynamic effects, and the footprint is wider in y direction than in x direction since the wettability gradient is actually stripped in x direction. Third, the theoretical model is developed using small contact angles and approximation, so the value predicted at small contact angles should be more accurate to the real physical values. This also explains well the decreasing difference between theoretical and simulation results as the contact angle decreases.

To obtain internal flow fields, the computational domain is divided into cubical cells, and the local velocity of each cell is obtained by averaging all the beads at each sample time step in each

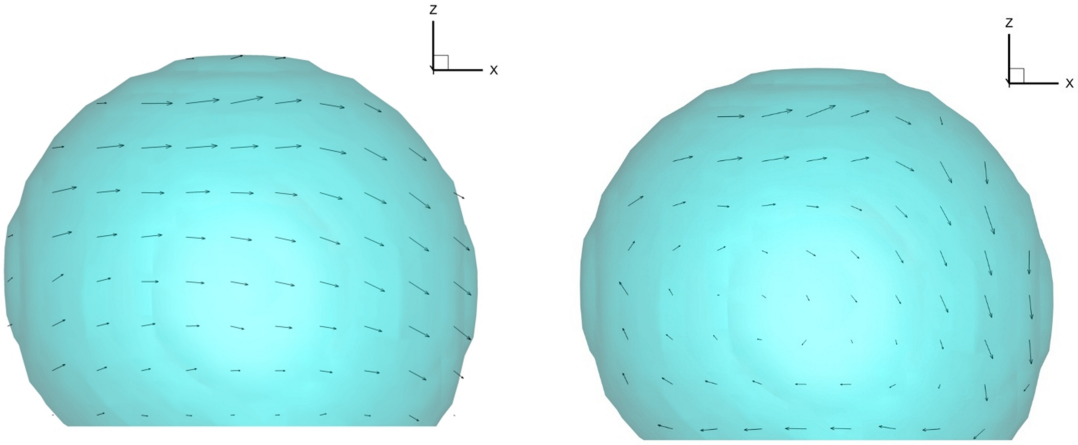

(a) (b)

Figure 2.17: The flow vectors of the droplet and relative flow to the droplet center

cubic cell using the quasi-stationary method mentioned above. One result is shown in Fig. 2.17a, which is the flow field at $t = 500$. The absolute velocity near the wall is relatively small compared with the velocity of the upper portion. By subtracting the velocity of droplet center, the relative motion to the droplet center is shown in Fig. 2.17b, which exhibits the rotational motion clearly.

2.5 Conclusion

In this chapter, we have briefly reviewed the development and basics of the DPD method. The difference and resemblance between the DPD method and other typical CFD tools, such as MD and Navier-Stokes solvers, were also discussed. Different methods to implement the no-slip wall boundary conditions in the DPD scheme were compared, and our newly designed symmetric boundary condition was also introduced. By using this symmetric boundary condition, the computational time required can be greatly reduced. After that, to validate our in-house codes, Poiseuille flow and a moving droplet driven by wettability gradient were simulated, and the results were found to agree well with theoretical predictions.

Chapter 3

Modeling of solid microparticles in MDPD

In this chapter, we investigate the interaction of a single microparticle with a liquid droplet on a flat substrate using many-body dissipative particle dynamics (MDPD). The modeling of a solid microparticle in the MDPD scheme is introduced first. Then, the manipulation processes for a hydrophobic microparticle by a droplet are studied in detail, including pickup and transport of the microparticle.

3.1 Modeling of solid microparticle

To model the solid microparticle, relevant forces must be included to capture enough physical details. For an object of such small size, the dominant forces are the surface adhesion force viz. van der Waals (vdW) force, liquid-solid interfacical force, normal force, and resistance (friction) forces between two solid phases in contact. Other forces like gravity turn out to be much smaller than these [181–184]. A comparison of the adhesion force and gravity force of different particles is given in Table 3.1 [184], showing that the gravity force is always several orders of magnitude smaller than the adhesion force. Without consideration of the negligible gravitational body force in this study, the forces to be considered and modeled are either due to droplet microparticle interactions or wall microparticle interactions. So, from these two aspects, the details for the modeling of a microparticle are introduced in the following subsections. The geometrical formation of a spherical microparticle is represented first. After that, the droplet microparticle interaction is modeled to avoid unphysical penetration of liquid bead into the solid microparticle. Then, the wall microparticle interaction is designed based on contact mechanics. In the end, the algorithm for updating the motion of the microparticle is given.

3.1.1 Solid spherical shell

As for the shape of a microparticle, the spherical shape will be ideal for experimental manipulation due to its isotropy and low resistance. From the numerical perspective, a microsphere will

Table 3.1: Comparison of adhesion force and gravity force for particles of different sizes and materials [184]

Particle	Adhesion force (N)	Gravity force (N)
32 μm glass particles	1.83×10^{-6}	4.03×10^{-10}
72 μm glass particles	4.21×10^{-6}	4.60×10^{-9}
70 μm glass particles	1.59×10^{-6}	1.40×10^{-8}

also be an ideal start to test the algorithms of modeling before considering any complex geometries or surface roughness.

To generate a solid sphere in the MDPD method, there are two natural choices. First, one "large" bead can be used to represent a sphere with a certain core radius. The interaction between the sphere and other fluid beads is then determined by the surface-to-surface distance, rather than the natural center-to-center distance in this particle method. In this way, the advantage is that the sphere can be perfectly smooth, but the critical disadvantage is not being able to easily model a microparticle of any shape. The other way for modeling a sphere is to pack its surface or volume with uniformly distributed beads, which are fixed at their relative positions to the sphere center. The interaction between beads composing the sphere and other fluid beads is determined by the center-to-center distance, which is the natural implementation in this particle method. The disadvantage of this spherical packing modeling is lack of isotropy, but the situation can be improved by packing more beads and doing so more evenly. On the other hand, a great advantage of this model is the capability to be extended to other complex geometries by simply filling the beads into the geometry. In this study, a spherical shell is used to represent the microparticle, formed by 612 beads uniformly distributed on the shell surface [185]. The reasons for choosing this shell structure and this number will be given in the following subsection, in consideration of computation cost, spherical isotropy, and liquid microparticle interaction.

3.1.2 Microparticle liquid interaction

In multiphase DPD simulations involving liquid microparticle interactions, both liquid phase and solid microparticles are composed of soft beads that by default allow overlap and penetration between different kinds of beads. For solid objects without any porosity, this penetration process is not a physical phenomenon. To prevent the undesired penetration of liquid beads into solid bodies, intuitively, a spherical reflection boundary condition can be applied at the sphere surface. However, since both liquid beads and solid microparticles are free to move, it will require great effort to deal with multi-body collisions to conserve the momentum and represent the details during collisions. This will also lead to an increase in computational time, since an iterative method for this multi-body collision problem will be required for each time step. To avoid this complicated and time-consuming reflection method, the liquid beads can be prevented from penetrating solid boundaries by utilizing the repulsive conservative force in the DPD method. Following this idea, there are two schemes reported in the literature to avoid penetration of liquid beads into spherical microparticles, as shown in Fig. 3.1.The first scheme is to configure a solid DPD microsphere by arranging

(a) (b)

Figure 3.1: Spherical microparticles formed by a group of solid beads. (a) beads in a face-centered-cubic lattice via rigid or super strong bonds; (b) beads packed on the surface of the spherical shell

many DPD beads in a face-centered-cubic (fcc) lattice via rigid or super strong bonds [186–189]. In previous studies, to avoid the undesirable penetration of liquid beads into the solid microspheres, the fcc lattice constant of the microspheres was specially chosen at 0.73 r_c. By reducing this lattice constant, denser beads are packed into these solid microspheres so that a strong enough repulsive force will be generated once the liquid bead gets close to it. The second scheme is to model the microparticle as a hollow sphere with some solid beads packed on the surface [89, 190]. By sufficient number of beads arranged on the surface, the liquid beads are spontaneously prevented from penetrating the microparticles. Using this hollow sphere, less solid beads are needed compared with the first scheme to fill the whole solid sphere, thus saving computational cost.

However, in the MDPD method, the pairwise conservative force is composed of not only a repulsive component but also an attractive component, as shown in Eq. (2.35). The attractive force between liquid beads and solid microparticle beads tends to induce penetration of liquid beads into the microparticle. By examining Eq. (2.35) again, it can be found that the repulsive force strongly depends on the bead density given in Eq. (2.37), which increases quickly when two beads get very close. So the overall force for two beads close to each other is repulsive, and it finally becomes attractive when the distance between beads increases to some value larger than the repulsive cutoff radius r_d but still less than the attractive cutoff radius r_C. According to this, a promising solution can be found by densely packing solid beads on the shell surface or into the solid sphere. This is also in accordance with the scheme for generating the microparticle mentioned in the previous subsection. In this study, microspheres formed by different numbers of solid beads are tested, following the reference work for choosing and uniformly locating these beads on the shell surface [185]. As a result, without modifying any weight functions or cutoff radius for the conservative force between liquid beads and solid beads, penetration is successfully avoided for microspheres formed by 312 beads, 612 beads, and 1242 beads. The number of solid beads used to form a uniform microsphere cannot be any arbitrary number, so it is not feasible to double this number exactly, as is the common practice in grid-based methods. In fact, the number and positions of these solid beads are specially chosen so as to uniformly distribute the beads on the surface of the sphere [185]. Considering the trade-off between computation cost and spherical isotropy, an intermediate value, a microsphere with 612 beads, is used in this study for all of the following simulations. After that, different inter-

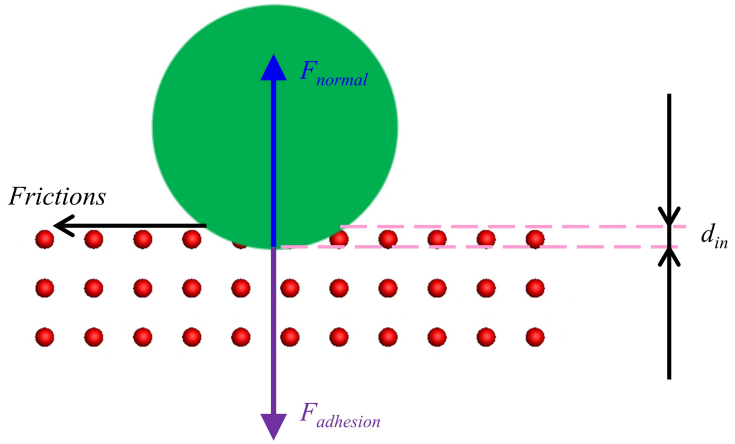

Figure 3.2: Relevant forces to be modeled for the microparticle substrate interaction, including adhesion force, normal force, and friction force. The microparticle is assumed to be rigid and the contact between the rigid microparticle and the elastic wall will lead to an indentation, noted as d_{in}.

facial behaviors of the microparticle, like hydrophobic or hydrophilic, can be obtained by adjusting the repulsive force component and attractive force component between liquid beads and solid beads forming the microparticle. In fact, the repulsive force component is fixed, while the attractive force component is adjusted to achieve hydrophobic or hydrophilic properties, the same as in the method used in Section 2.4.

3.1.3 Microparticle substrate interaction

After the interactions between liquid beads and microparticle beads are dealt with as desired in the previous subsection, the interaction between wall beads and microparticle beads needs to be modeled as well. The relevant forces to be modeled are shown in Fig. 3.2, including adhesion force viz. van der Waals (vdW) force, normal force, and friction force.

Due to the microsize of the solid particle, the adhesion force may mainly originate from van der Waals bonds, without considering any other ionic, covalent, or acid-base bonds. Though it is impossible or extremely complicated to model the exact forces from physical principles, this attractive behavior can be easily implemented by adjusting the conservative interaction force between wall beads and microparticle beads. The attractive and repulsive components between wall beads and microparticle beads can be adjusted accordingly to have a desired adhesive behavior and even controllable adhesive strength. Due to this adhesion force, which is obtained by summing all the forces exerted on microparticle beads by the wall, the microparticle is dragged toward the fixed wall and tends to penetrate it. To avoid penetration, this adhesion force can be physically balanced by a normal force from the wall due to the contact so that no other reflection modeling or boundary conditions are needed. This normal force is directly related to the shape deformation of geometries. Based on the contact mechanics for modeling solid-solid contact [107, 191], the wall material is

assumed to be elastic and the spherical microparticle is assumed to be rigid. Then the normal force can be calculated based on the depth of indentation d_{in} as given by

$$F_{normal} = \frac{4}{3} R_s^{1/2} d_{in}^{3/2} E \tag{3.1}$$

where F_{normal} is the normal force, E is the elastic modulus of the wall, and R_s is the radius of the solid microparticle. Meanwhile, once there is contact between two solid surfaces, the level of friction also needs to be considered if there is relative motion between them. Since the wall is fixed, there will be static friction on the microparticle if it has a potential to slide along the wall. When the driving force on the microparticle goes beyond the maximum static friction, the microparticle starts to move but is retarded by translational friction. Besides translational friction, a rolling motion possibly occurs for the microparticle in contact with the wall if there is a net torque on the microparticle. The translational friction force and rolling friction force on the microparticle are obtained based on the normal force, as given by

$$\begin{aligned} F_{trans} &= f_s \times F_{normal} \\ F_{roll} &= f_r \times F_{normal} \end{aligned} \tag{3.2}$$

where f_r is the rolling friction coefficient and f_s is the maximum static friction coefficient, which is assumed to be the same as the translational friction coefficient.

3.1.4 Motion of the microparticle

After modeling of relevant forces on the microparticle, position and velocity of the microparticle can now be calculated based on all these relevant forces. The microparticle moves as a rigid sphere, and the motion can be decomposed into two completely independent parts: translation and rotation, which can be determined by the total force and torque exerted on the entire microparticle [192, 193]. The force and torque acting on the entire microparticle are calculated by summing the forces and torques on each bead composing the microparticle. Then, the translational motion and rotational motion of the microparticle are integrated independently, which is explained in detail in the following.

First, for the translational motion, the position and velocity of the microparticle can be integrated straightforwardly, as given by

$$\begin{aligned} \frac{d\vec{r}_s}{dt} &= \overrightarrow{v_s} \\ m_s \frac{d\overrightarrow{v_s}}{dt} &= \sum_{i=1}^{N_s} \overrightarrow{f_i} \end{aligned} \tag{3.3}$$

where N_s is the total number of beads forming the microparticle, m_s is the mass of the solid microparticle obtained by summing the mass of the N_s beads on the sphere surface, $\overrightarrow{v_s}$ is the velocity of the solid microparticle, $\vec{r}_s$ is the position of the microparticle, and $\overrightarrow{f_i}$ is the total force exerted on each bead of the microparticle from all neighbor beads as given before. In fact, the position and velocity of the microparticle are calculated using the centroid of the sphere.

As for the rotational motion or rolling motion of the microparticle, some additional calculations are needed to update the orientation of the microparticle and positions of each bead on the surface. If there is net torque on the microparticle, it may cause a rotational motion when the microparticle is suspended. Once the microparticle is in contact with the wall, the net torque may lead to a rolling motion of the microparticle, which can be treated as a combination of rotational motion and translational motion. Thus, if there is net torque, one can always start with the integration of rotational motion. Once the microparticle has a rotation of angle ϕ, the position of each bead will change accordingly, as given by [193]

$$R_{xyz}^{new} = Rot_{\phi} R_{xyz}^{old} \tag{3.4}$$

where R_{xyz}^{old} and R_{xyz}^{new} are the old and new positions of one bead on the microparticle surface, respectively, and Rot_{ϕ} is the rotation matrix. This rotation matrix is directly evaluated based on the value of ϕ, as

$$Rot_{\phi} = \begin{bmatrix} Rot_{11} & Rot_{12} & Rot_{13} \\ Rot_{21} & Rot_{22} & Rot_{23} \\ Rot_{31} & Rot_{32} & Rot_{33} \end{bmatrix} \tag{3.5}$$

where

$$\begin{aligned}
Rot_{11} &= \frac{\omega_x^2}{\omega^2}(1-\cos\phi) + \cos\phi \\
Rot_{12} &= \frac{\omega_x\omega_y}{\omega^2}(1-\cos\phi) - \frac{\omega_z}{|\omega|}\sin\phi \\
Rot_{13} &= \frac{\omega_x\omega_z}{\omega^2}(1-\cos\phi) + \frac{\omega_y}{|\omega|}\sin\phi \\
Rot_{21} &= \frac{\omega_x\omega_y}{\omega^2}(1-\cos\phi) + \frac{\omega_z}{|\omega|}\sin\phi \\
Rot_{22} &= \frac{\omega_y^2}{\omega^2}(1-\cos\phi) + \cos\phi \\
Rot_{23} &= \frac{\omega_y\omega_z}{\omega^2}(1-\cos\phi) - \frac{\omega_x}{|\omega|}\sin\phi \\
Rot_{31} &= \frac{\omega_x\omega_z}{\omega^2}(1-\cos\phi) - \frac{\omega_y}{|\omega|}\sin\phi \\
Rot_{32} &= \frac{\omega_y\omega_z}{\omega^2}(1-\cos\phi) + \frac{\omega_x}{|\omega|}\sin\phi \\
Rot_{33} &= \frac{\omega_z^2}{\omega^2}(1-\cos\phi) + \cos\phi
\end{aligned} \tag{3.6}$$

where ω_x, ω_y, and ω_z are components of angular velocity $\vec{\omega}$ in x, y and z directions, respectively, and $\phi = |\omega|\Delta t$ and $|\omega|$ is the amplitude of $\vec{\omega}$. In order to obtain the angular velocity of the microparticle $\vec{\omega}$ due to a net torque on it, a position vector relative to the centroid of the microparticle R_C can be

defined first as

$$\overrightarrow{r_{iC}} = \overrightarrow{r_i} - \overrightarrow{R_C} \tag{3.7}$$

where $\overrightarrow{r_i}$ is i^{th}'s bead position in global computation coordinates. Then the angular momentum of the microparticle $\vec{L}$ can be obtained as

$$\overrightarrow{L} = \sum_{i}^{N_s} \overrightarrow{r_{iC}} \times \overrightarrow{P_i} \tag{3.8}$$

where $\overrightarrow{P_i}$ is the momentum of each bead defined by definition as $\overrightarrow{P_i} = m_i \overrightarrow{v_i}$. Then the rotational velocity can be found from the relation

$$\overrightarrow{\omega} = I^{-1} \cdot \overrightarrow{L} \tag{3.9}$$

where I is the momentum of inertia. Since the microparticle in this study is represented by a spherical shell, the momentum of the inertia tensor can be replaced by a constant value for a spherical shell as $I = 2N_s m_i R_s^2/3$. This is another reason to pack more beads uniformly on the shell surface so this approximation can be more accurate. Then the rate of change of the angular momentum is determined by the externally applied torque summarized over all beads on the surface

$$\frac{d\overrightarrow{L}}{dt} = \sum_{i}^{N_s} \overrightarrow{r_{iC}} \times \overrightarrow{f_i} \tag{3.10}$$

The updated value of the rotational velocity $\vec{\omega}^{new}$ after a time step Δt is found from the first-order approximation by combining Eq. (3.9) and Eq. (3.10)

$$\vec{\omega}^{new} = \vec{\omega} + \frac{d\vec{\omega}}{dt}\Delta t \tag{3.11}$$

$$= \vec{\omega} + \frac{1}{I} \cdot \Delta t \cdot \sum_{i}^{N_s} \overrightarrow{r_{iC}} \times \overrightarrow{f_i} \tag{3.12}$$

Once the microparticle stays in touch with the wall, a rolling motion will take place, instead of the rotational motion for a suspended microparticle. Based on the assumption that there is no slipping at the contact point, this rolling motion can be decomposed of a rotational motion in a reference frame fixed to the microparticle and a translational motion of the centroid in a reference frame fixed to the wall, as shown in Fig. 3.3. The rotational motion component can be solved in a similar way as mentioned above for a suspended body. For the translational motion component, a displacement of an arc length $R_s\phi$ has to be added to the microparticle centroid and all of the beads on the sphere surface. So, to decide whether there is a rotational motion or rolling motion, the microparticle's position has to be monitored during the simulations to determine whether there is contact with the solid wall.

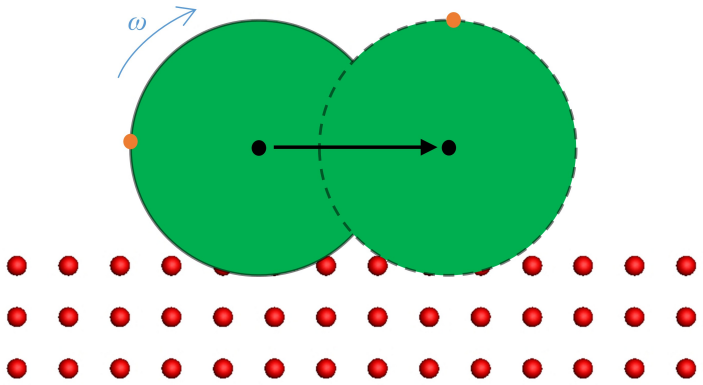

Figure 3.3: Rolling motion of the microparticle on the wall: the sphere with a solid black boundary shows the previous position and the one with a dashed black boundary shows the updated position. The marker in orange illustrates the rotational motion, and the centroid in black shows the translational motion.

3.2 Pickup and transport of a hydrophobic microparticle

After modeling of the microparticle, we are now ready to study the interactions among a microparticle, a droplet, and a wall. As a baseline case, the pickup and transport of a hydrophobic microparticle by a droplet is simulated and analyzed in detail. The problem setup and parameters will be given first in the following subsection. Then the trajectory of the microparticle, as well as the flow fields inside the droplet containing the microparticle, will be examined. A phenomenological comparison with experimental observations will be used to validate our numerical model.

3.2.1 Simulation setup

A design based on the case in Section 2.4 is used to study the interactions among liquid droplet (l), wall (w), and solid microparticle (s), as the initial setup at $t = 0$ shown in Fig. 3.4. It simulates a moving droplet driven by the wettability gradient (such as voltage difference between two electrodes), with an addition of a microparticle in the midway. The simulations are performed in a three-dimensional computational domain of size $150(x) \times 70(y) \times 20(z)$. The origin point is set at the center of the computational domain. The start position of the wettability gradient region x_0 is set as -40, which is also the initial position of the liquid droplet center. The wall surface is set at $z = -10$. Some other parameters are shown in Table 3.2, which are unchanged throughout the study. R_l is the radius of the liquid droplet, R_s is the radius of the solid microparticle, and d is the initial distance between the droplet and the microparticle. The scaling between nondimensional MDPD units and physical units is shown in Table 3.3.

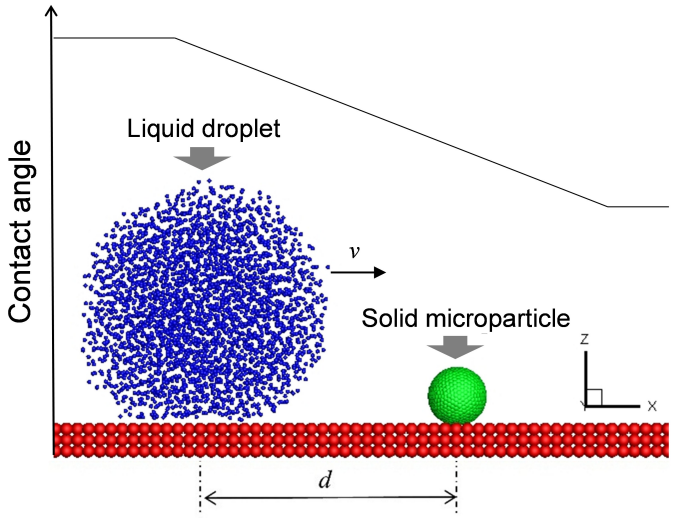

Figure 3.4: Initial setup of liquid droplet (blue) and solid microparticle (green) resting on the substrate (red); d is the initial distance between the droplet and the microparticle.

Besides the parameters mentioned above, the effects of the remaining parameters on the manipulation of the microparticle will be parametrically studied in the next chapter. These parameters include droplet radius R_l, friction coefficients f_r and f_s, and attraction parameter between liquid beads and microparticle beads A_{ls}, which determines the hydrophilicity of the microparticle. For the current baseline case, droplet radius R_l is 5 and the attraction force between liquid beads and microparticle beads A_{ls} is -15, indicating that the microparticle is hydrophobic. The initial distance between the droplet and the microparticle d is 10, which means the initial x position of the microparticle is -30. The friction coefficients between the microparticle and the substrate are $f_s = 0.2$ and $f_r = 0.1$. The wettability gradient region ends at $x_f = 40$, so according to Eq. (2.39), the location-dependent A_{lw} is obtained as

$$A_{lw} = \begin{cases} 8.765 & x < -40 \\ -1.211 - \sqrt{552.125 - 3.30033 \times \theta_0 + 3.300 \times \frac{\theta_0 - \theta_f}{40-(-40)}(x-(-40))} & -40 \le x \le 40 \\ 21.707 & x > 40 \end{cases} \tag{3.13}$$

3.2.2 Results and discussion

The simulation is conducted in two stages. In the first stage, a uniform wettability condition is applied on the wall so that the liquid beads initialized on the structured fcc lattice are allowed to gradually form a natural droplet shape with a certain contact angle with the wall, like the droplet shown in Fig. 3.4. Physically, this refers to the state when all electrodes are charged with the same voltage. After that, a specific wettability gradient is applied on the wall to actuate the droplet from

Table 3.2: The computational parameters for modeling of the microparticle and wettability gradient. Adapted with permission from [194]. Copyright 2015 American Chemical Society.

Parameter	Symbol	Value
Elastic moduli of wall	E	1.00e+6
Initial position of liquid droplet	x_0	-40.00
Radius of solid microparticle	R_s	1.00
Amplitude of attractive force	A_{sw}	-1.00
Amplitude of repulsive force	B_{ls}	3.00
Contact angle at hydrophobic end	θ_0	150.00°
Contact angle at hydrophilic end	θ_f	40.00°
Initial distance between droplet and microparticle	d	10.00

Table 3.3: Scaling between nondimensional MDPD units and physical units for the manipulation of microparticles

Variable	Symbol	MDPD system	Physical value
length	r_c	1.0	$4.0\mu m$
mass	m_{MDPD}	1.0	$4.48 \times 10^{-14} kg$
surface tension	σ	7.53	$0.073 N/m$
time	t	1.0	$2.16\mu s$

the hydrophobic end to the hydrophilic end, which physically means the voltage on one electrode is suddenly switched to trigger the motion of the droplet. The microparticle, initially positioned near the hydrophobic end, will be picked up and transported by the droplet to the hydrophilic end. To be specific, in this baseline case, the first stage runs 2,000 time steps using a uniform contact angle at 150°. The second stage runs for another 800,000 time steps using the wettability condition as given in Eq. (3.13).

For one representative run, the time histories of the x and z positions of the microparticle center are shown in Fig. 3.5, sampled for every 10 time steps starting from the second stage. Fluctuations of the curve can be observed for the x position of the microparticle due to the Brownian motion. For the z position, the fluctuations may not be observed clearly from the figure due to limited resolution and dense data points. Actually, the amplitude of fluctuations in the z direction remains within a tiny range less than ± 0.01. The z position of the microparticle is always slightly below -9, which is the horizontal position of the wall surface, indicating that the microparticle is always in contact with the substrate and friction forces always exist. The x-position curve of the microparticle is composed of two segments: a concave (upward) segment and a convex (concave downward) segment. The microparticle is accelerated in the concave upward segment, while it is decelerated in the convex segment. There exists an inflection point between $t = 2000$ and 4000. After passing $x = 40$ at $t = 4800$, the velocity of the droplet will slow down to zero due to friction and the lack of a driving force (the trivial wettability gradient exerted on a small portion of the droplet).

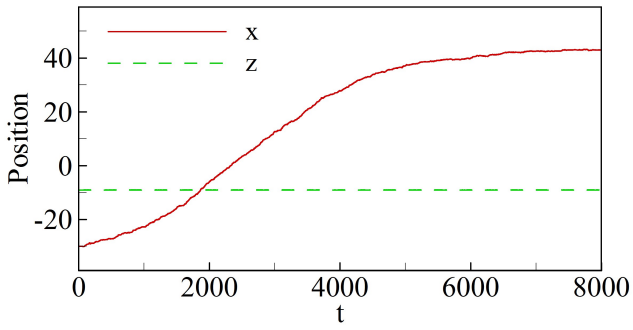

Figure 3.5: Variation of the position of the microparticle center with time. Adapted with permission from [194]. Copyright 2015 American Chemical Society.

To present the results more visually, the droplet shape and position as well as the microparticle position at four different times, t = 80, 1600, 3200, 4800, are shown in Fig 3.6. Similar to the results in Section 2.4, the droplet deforms gradually from a spherical shape to a cap shape, spreading more widely in the more hydrophilic area. When the droplet moves from the hydrophobic end to the hydrophilic end along the x direction, its front end contacts the microparticle first. Due to the adhesion and friction between the microparticle and the substrate, the microparticle is not pushed away by the droplet at the beginning but gradually gets submerged into the droplet. After most of the droplet bypasses it, the microparticle is finally pulled away by the droplet. During the whole transport process, the microparticle always stays near the vapor/liquid interface in the receding region of the droplet and keeps contact with the substrate. The simulation results on the transport of a single hydrophobic microparticle are consistent with the experimental observation on collection of superhydrophobic PTFE particles by Zhao [46], as shown in Fig. 1.6. In their experimental observations, the collected hydrophobic particles also stayed near the air-to-water interface but not inside the water droplet. Due to the friction between the microparticle and the substrate, the droplet is significantly decelerated. From an auxiliary case using the same setup and parameters without the microparticle, the travel time for the droplet from $x = -40$ to 40 is 2973 . With the existence of the microparticle, the travel time increases to 4800.

To examine the flow fields inside the droplet containing a microparticle and to compare it with the situation without a microparticle in Section 2.4, the quasi-stationary method mentioned in Section 2.4 is applied here again. The quasi-stationary state can be obtained in this case, because the position of the hydrophobic microparticle is relatively fixed to the droplet when a constant wettability gradient is applied. To save computational time, the position of the microparticle center is tracked instead of the droplet center, which requires averaging all of the liquid beads for every time step. Due to the complexity and randomness introduced by the existence of the microparticle, 2,000,000 time steps are sampled to average out the fluctuations by cutting the computational domain into many small cells and averaging the particles inside each cell. The flow structures in the x-z plane are represented in Fig. 3.7, as the position of the microparticle center equals $x = -10$. The

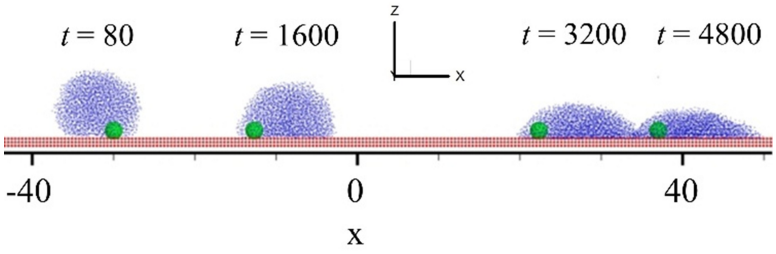

Figure 3.6: Shape and location of the droplet and microparticle at four different times, t = 80, 1600, 3200, 4800. Adapted with permission from [194]. Copyright 2015 American Chemical Society.

result is taken in x-z plane along the middle of droplet as well as going through the center of the microparticle. Different from the combined motion of translation and rotation in a droplet without a microparticle (Fig. 2.17), there is a clear downward and pushing motion in the rear side of the microparticle. In the front end of the droplet, there is a small rotational motion in a limited domain. Compared with the rotational motion inside the whole droplet in Section 2.4, this also explains the smaller velocity than the case without the microparticle. Although the deformation of the droplet is similar to the case without the microparticle, the existence of the microparticle greatly alters the flow fields inside the droplet, thus reducing the overall moving velocity of the droplet.

From a different view angle, the flow fields inside the droplet are also shown for the y-z plane in Fig. 3.8. The microparticle lies in the middle of the droplet in the y direction. Near the bottom of the droplet, rotational motions exist at both sides of the microparticle, which is similar to the droplet motion without the existence of the microparticle obtained by Li et al. [82]. The flows are both upward in the area close to the microparticle on both sides. As a result, the droplet tends to lift up the microparticle due to the liquid motion inside. This also helps reduce the friction between the microparticle and the substrate, thus enhancing the forward motion along the wettability gradient direction. However, this hydrodynamic drag itself is not too strong to counteract the adhesion force from the substrate. The hydrophobic microparticle still lies on the substrate, causing friction forces. In the area near the air droplet interface, the flow is outward in the y-z plane and forward in the x direction (Fig. 3.7). The liquid particles move gradually from the rear to the front so the droplet as a unified whole moves forward together with the microparticle.

3.3 Conclusion

In this chapter, the modeling of microparticles in the MDPD scheme is introduced. Using a spherical shell to represent the microparticle, the droplet-microparticle interaction is modeled by packing dense beads on the shell surface to avoid the penetration of liquid beads into the microparticle, while conserving the momentum automatically. After that, the interaction between the rigid microparticle and the solid wall was modeled following the principles of contact mechanics. The adhesion force, normal force, and friction forces between the microparticle and the wall are all considered. When all relevant forces are obtained, the translational motion and rotational motion of

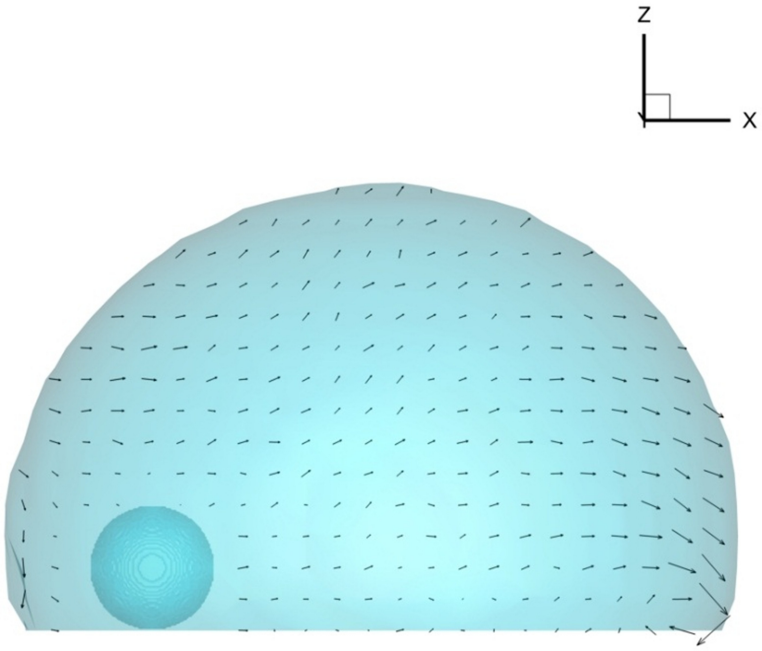

Figure 3.7: The flow vectors of the droplet in the *x*-*z* plane with the existence of the microparticle

the microparticle are integrated independently by summarizing the forces and torques on each bead forming the microparticle.

After the model was designed, a baseline case was conducted to simulate the pickup of a hydrophobic microparticle by a droplet, which is actuated by the wettability gradient of the wall. The pickup and transport of the microparticle are obtained successfully once the droplet encounters the microparticle. During the transport, the droplet deforms from a spherical shape at the hydrophobic end to a cap shape at the hydrophilic end. The microparticle is dragged by the droplet toward the hydrophilic end, staying on the wall near the air liquid interface. Due to the contact and friction between the microparticle and the wall for the whole process, the motion of the droplet is decelerated compared to the motion of a droplet without the microparticle. Using the quasi-stationary method, the flow structures inside the droplet are found to be greatly different from a droplet without a microparticle, especially the flows along the droplet moving direction. There is a hydrodynamic lift force on the microparticle, but not enough to lift it up from the wall.

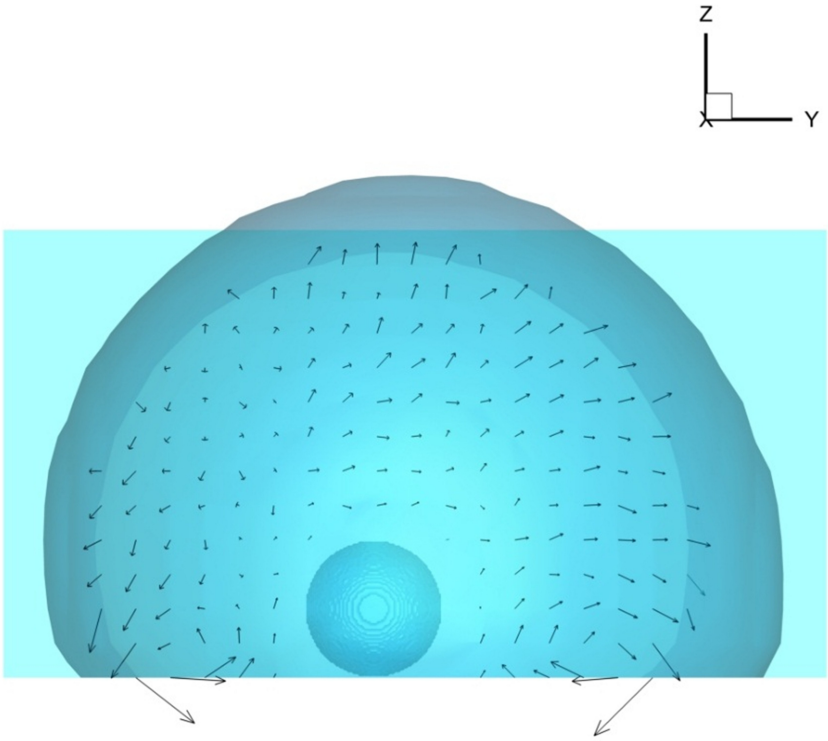

Figure 3.8: The flow vectors of the droplet in the *y*-*z* plane with the existence of the microparticle

Chapter 4

Effects of different factors on pickup and delivery of microparticles

In this chapter, effects of different factors on the manipulation processes (including pickup, transport, and drop-off) are investigated. These factors include the droplet size, wetting properties of the microparticle, and particle-substrate friction coefficients. These are important and controllable parameters for a DMF system to perform different functions. However, to control the delivery of microparticles, a trap design or an external magnetic field is always required in a DMF system, adding to the complexity of the experimental system [31]. To find a better solution, a trap-free delivery of a hydrophobic microparticle is designed and demonstrated in our numerical work based on the previous results and understanding of the droplet-microparticle interactions, without adding any new structures or external forces.

4.1 Effects of different factors on the pickup of a single microparticle

In this section, the effects of different factors on the pickup and transport of the microparticle will first be studied. Based on the baseline case in the previous chapter, parametric studies are performed on several important factors, including droplet radius R_l, wetting property of the microparticle A_{ls}, and friction coefficients of the wall f_r and f_s, as shown in Fig. 4.1. The results for the effects of each factor will be introduced in the following subsections, respectively. All of these parameters can be physically and easily adjusted in experimental designs and manufacturing. For example, as introduced in Chapter 1, microparticles of different sizes and different coating materials have been employed in different kinds of biological and chemical applications. Droplet size can be controlled by a nozzle, and properties of a wall can be changed by coating it with materials of different properties.

4.1.1 Droplet size

The effect of droplet size is first studied in this subsection by using droplets of different radii with other parameters given in Table. 3.2. The initial setup of the simulation is the same as the baseline case in Section 3.2.1. Similarly, the simulation for each case in this section is also

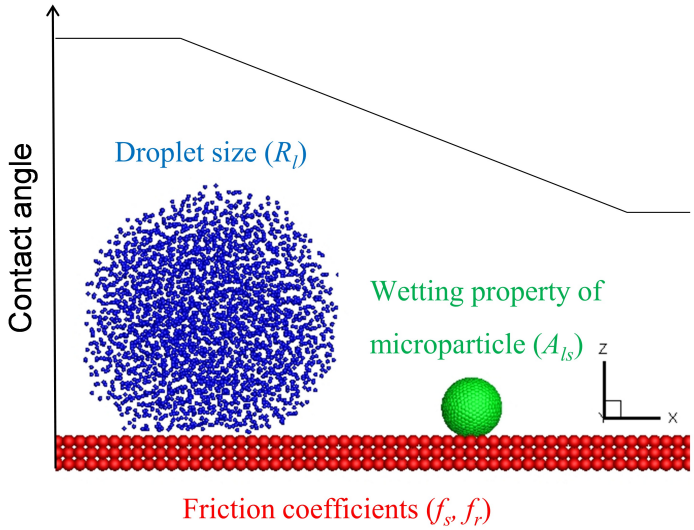

Figure 4.1: Different factors to be studied for their effects on the manipulation of the microparticle.

composed of two stages. The first stage runs 3000 time steps using a uniform contact angle at 150° before actuating the droplet. Because more liquid beads are required for larger droplets, more time steps are used for the first stage compared to the baseline case. The second stage runs for another 1,000,000 time steps using the same wettability condition as given in Eq. (3.13). Friction coefficients between the microparticle and the substrate are $f_s = 0.2$ and $f_r = 0.1$. The attraction force parameter between the liquid beads and the microparticle beads A_{ls} is -15, indicating that the microparticle is hydrophobic.

The results of one representative run for each case are analyzed in the following. The time history of microparticle movement (in terms of the x position of the microparticle center) is shown in Fig. 4.2 for four different droplet sizes, i.e., $R_l = 5, 6, 7$, and 8. The curves are obtained by recording the microparticle position for every 10 time steps. It can be seen that, in all cases, the microparticle is successfully picked up and transported from the hydrophobic end $x = -30$ to the hydrophilic end $x = 40$, as the five lines finally overlap after $t = 8000$. Meanwhile, as seen from Fig. 4.2, the larger the droplet size is, the faster the microparticle is transported to the hydrophilic end. The travel time for the microparticle from $x = -30$ to $x = 0$ is shortened from 2317 to 1673, 1324, and 1140 as the droplet radius increases from 5 to 6, 7, and 8. For a larger droplet, the difference of wettability across the droplet is larger due to the larger contact surface between the droplet and the substrate. So the motion of the droplet becomes faster as the droplet size becomes larger and larger, though the difference gets gradually smaller with further increases in R_l. Therefore, by increasing droplet size, the driving force on the droplet is increased and the duration of the microparticle transport is shortened. This result can be a helpful guidance for experimental design, since considering the cost of solutions, a much larger droplet size is not beneficial at all for the pickup and transport of a microparticle, as well as a waste of materials. The optimal droplet size for the microparticle, not

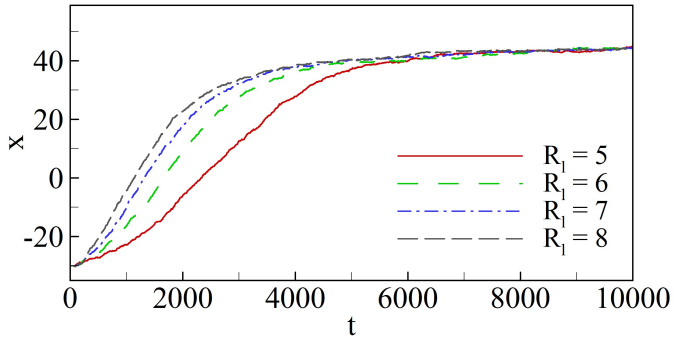

Figure 4.2: Time history of the microparticle position for different droplet sizes. Reprinted with permission from [194]. Copyright 2015 American Chemical Society.

too small to pick up the microparticle nor too big, can be determined by more tests within a wider range.

4.1.2 Wetting property of the microparticle

As discussed in the Introduction, the wetting property of the wall can be tuned from hydrophobic to hydrophilic by controlling the liquid wall interaction parameter A_{lw}. Similarly, the wetting property of the microparticle can also be adjusted by tuning the liquid microparticle interaction parameter A_{ls}. The surface wettability of the microparticle can be changed from hydrophobic to hydrophilic by decreasing the value of A_{ls}. Since the droplet in the present study is always a water droplet (as the surface tension in the scaling tables shown above), not any other oil or ethanol droplet, the wetting property of the microparticle is in fact referring to the wetting behavior between the microparticle and water. In experimental works [46], different types of particles with different contact angles (in parentheses) have already been studied, such as polystyrene (66°), Teflon coated glass (120°), and Teflon powder (110°). So the values of my parameters are inside the range of physical possibilities. In this subsection, six different cases with $A_{ls} = -15, -16, -17, -18, -19$, and -19.5 are simulated to study the effect of the wetting property of the microparticle. As A_{ls} changes from -15 to -19.5, the corresponding contact angle varies from 109° to 66°. The numerical setup is the same as that in the previous subsection except with varied values of A_{ls} and the fixed droplet size of $R_l = 5$.

The results of one representative run for each case are analyzed in the following. Figure 4.3 shows the time history of the microparticle for six different values of $A_{ls} = -15, -16, -17, -18, -19$, and -19.5. The curves are obtained by recording the microparticle position for every 10 time steps. In all cases, the microparticle is successfully picked up and transported from the hydrophobic end $x = -30$ to the hydrophilic end $x = 40$, while in cases $A_{ls} = -18, -19$, and -19.5 the final position of the microparticle is slightly further than in the other three cases. It is also found that, as the microparticle becomes more hydrophilic, less time is needed for the microparticle to be transported over the whole region, though the results for cases $A_{ls} = -19$ and -19.5 are quite close.

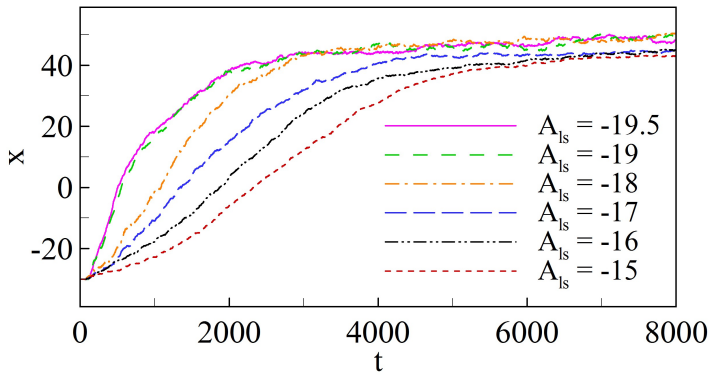

Figure 4.3: Time history of microparticle x-position with different hydrophilicity parameter A_{ls}. Adapted with permission from [194]. Copyright 2015 American Chemical Society.

To illustrate the reason for the different average speeds using different hydrophilicity, the temporal change of the z position of the microparticle center is shown in Fig. 4.4. It is found that the final z positions of the microparticle center stay at $z = -9$ for three cases with $A_{ls} \leq -17$. Since the z position of the wall surface is -10 and the radius of the microparticle is 1, the fact that the z position of the microparticle center is equal to -9 indicates that the microparticle is in contact with the wall surface. For the cases with $A_{ls} = -18$, -19, and -19.5, the final z positions of the microparticle center are lifted up to $z = -8$, i.e., about 1.5 above the substrate surface. For $A_{ls} = -19$, it should be noted that there is a sudden rise of the z position (up to $z = -5.5$) at $t = 234$, which means the microparticle is fully engulfed in the droplet, and then the microparticle center gradually returns to about $z = -8$ and keeps around this level after $t = 1000$. The inset of Fig. 4.4 clearly shows the relative position of the microparticle and the droplet at $t = 2000$ for $A_{ls} = -19$. The microparticle is already engulfed in the droplet and stays in the core area of the droplet. This is phenomenologically matched with the experimental observations for the sampling of superhydrophilic microparticles [46], as shown in Fig. 1.7(f). In these experimental works, the microparticles are suspended and distributed almost evenly within the droplet, due to the strong hydrophilicity. This phenomenon is totally different from the results for hydrophobic microparticles studied in Section 3.2. For $A_{ls} = -19.5$, there is also a similar sudden rise of the microparticle in the z direction at $t = 150$, which means engulfment, just a little bit earlier than the case $A_{ls} = -19$. For $A_{ls} = -18$, the rise of the microparticle in the z direction occurs much later and more weakly at $t = 1153$. Before the microparticle is lifted up, it is pulled forward on the substrate surface by the droplet. Because the friction between the microparticle and the substrate lasts longer in the $A_{ls} = -18$ case compared with the cases $A_{ls} = -19$ and $A_{ls} = -19.5$, there is slower transport of the microparticle in the $A_{ls} = -18$ case compared with the cases $A_{ls} = -19$ and $A_{ls} = -19.5$ (see Fig. 4.3). For the other three cases, $A_{ls} = -15, -16$, and -17, the microparticle stays almost constant around $z = -9$, implying that it is always attached to the substrate. For these cases, the trajectory curves overlap with each other, as the difference is too small to be easily detected from a graph. To reveal the tiny difference by averaging over the whole temporal domain, the averaged values of the

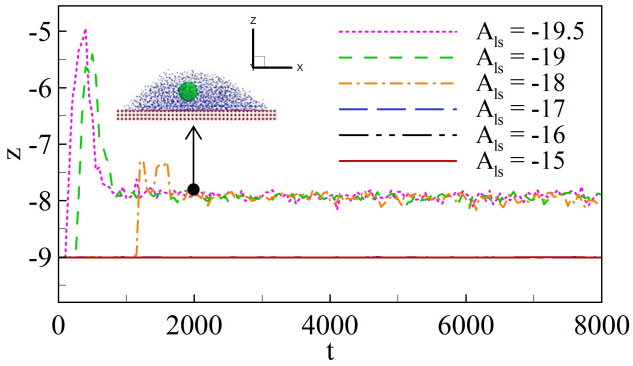

Figure 4.4: Time history of the z position of the microparticle center with different values of wettability parameter A_{ls}. The inset shows that the center of the microparticle is lifted up from the wall surface at $t = 2000$ for $A_{ls} = -19$, due to the engulfment in the core area of the droplet. Adapted with permission from [194]. Copyright 2015 American Chemical Society.

z position are: -9.00249 for $A_{ls} = -15$, -9.00216 for $A_{ls} = -16$, and -9.00170 for $A_{ls} = -17$. Five decimal places have to be used here to detect the difference between their z positions. The slightly higher z position for smaller A_{ls} results from stronger attractive force between the droplet and the microparticle. This more attractive interaction between the microparticle and the droplet slightly lifts up the microparticle in the z direction. Though the difference in the z position is quite small, it can lead to a big difference for normal force due to the strong elastic moduli of the substrate. A higher z position of the microparticle will lead to a smaller deformation on the wall surface, which results in a smaller normal force and friction for the motion of the microparticle. Consequently, the smaller the frictions are, the faster the microparticle is transported. This explains why there is faster transport of the microparticle for the case $A_{ls} = -17$ than the case $A_{ls} = -16$, which is slightly faster than the case $A_{ls} = -15$, as shown in Fig. 4.4.

As mentioned in previous paragraphs, the final positions of the microparticle in different cases are different in Fig. 4.3. The microparticle reaches the same final position at $t = 8000$ for $A_{ls} = -15, -16$, and -17, but not as far as the position for $A_{ls} = -18$, -19, and -19.5. The reason is that, for these three cases, the overall attractive force from the droplet on the microparticle is not large enough to engulf it, so the microparticle is always attached to the substrate and stays at the rear side of the droplet. When A_{ls} decreases to -18, the attractive force between the droplet and the microparticle is strong enough to pull the microparticle away from the substrate surface, and the microparticle stays in the middle of the droplet.

4.1.3 Frictions between the substrate and the microparticle

In experimental designs, the surface friction conditions can be different when different materials and different techniques are used for the layer-by-layer coatings on the substrate. In this subsection, the effect of surface frictions on the pickup and transport of the microparticle will be studied by tuning both the static friction coefficient f_s and rotational friction coefficient f_r. The

friction condition between the substrate and the microparticle depends on both objects. As for the microparticles, as some examples mentioned above, they are usually made of glass, polystyrene, or coated with Teflon [46]. And in some other studies [47], they also have worked with melamine and some airborne bio-particles, such as pollen with natural roughness from different species and bacteria. As for the substrate, it is usually made of a glass substrate coated with extreme thin insulator and hydrophobic layers (tens or hundreds of nanometers thickness), which can be made by silicon dioxide with Teflon, or Teflon alone [13]. However, to the author's best knowledge, detailed roughness conditions or friction conditions between the microparticles and the substrate have not ever been provided in the literature, because it is pretty hard to find out or measure the exact roughness based on their different manufacturing process for the substrate layers. Therefore, the levels of friction to be studied in the present work is based on the estimation between several main types of known materials, such as glass to glass (static friction coefficient is 0.9-1.0), polystyrene to polystyrene (0.5), rubber to rubber (1.16), PTFE to steel (0.05-0.2) [195]. In the present study, the choices of the static friction coefficients are ranging from 0.2 to 1.6, which are close to these common materials. As for the rolling friction coefficients, it is even harder to find such exact information in the literature or on websites. But in general it should be much smaller than the sliding friction.

The numerical setup used here is similar to that in Section 4.1.1 except for the friction coefficients. Six different combinations of f_s and f_r are selected to conduct the parametric study, including $f_s = 0.2$ & $f_r = 0.2$, $f_s = 0.4$ & $f_r = 0.2$, $f_s = 0.4$ & $f_r = 0.4$, $f_s = 0.8$ & $f_r = 0.4$, $f_s = 0.8$ & $f_r = 0.8$, and $f_s = 1.6$ & $f_r = 0.8$. The simulation for each case in this section is also composed of two stages. The first stage runs 3000 time steps using a uniform contact angle at 150° before actuating the droplet. The second stage runs for another 3 000 000 time steps using the same wettability condition as given in Eq. (3.13), considering the slower motions due to greater friction compared with previous cases.

Results of one representative run for each case are analyzed in the following. The time history of x positions of the microparticle center for six cases is compared in Fig. 4.5. The curves are obtained by recording the microparticle position for every 500 time steps. The results show that there is a significant increase in the transport time of the microparticle as friction coefficients increase. But the effects of two friction coefficients can be quite different as we compare different curves in the sequence. Between cases $f_s = 0.2$ & $f_r = 0.2$ (green line) and $f_s = 0.4$ & $f_r = 0.2$ (blue line), the transport time of the microparticle is greatly increased compared with the increase between cases $f_s = 0.4$ & $f_r = 0.2$ and $f_s = 0.4$ & $f_r = 0.4$ (black). These results indicate that, when the static friction is increased twice, there is a great increase for the transport time needed, which is also seen between the pair of case $f_s = 0.4$ & $f_r = 0.4$ and case $f_s = 0.8$ & $f_r = 0.4$, and the pair of case $f_s = 0.8$ & $f_r = 0.8$ and case $f_s = 1.6$ & $f_r = 0.8$. However, when the rotational friction is increased twice, only a slight increase is observed for the transport time needed, as is also seen between the pair of case $f_s = 0.8$ & $f_r = 0.4$ and case $f_s = 0.8$ & $f_r = 0.8$. So the manipulation of the microparticle is much more sensitive to the change in f_s than to that in f_r, hence only the effect of static friction coefficient f_s is discussed in the following text.

In cases of $f_s = 0.2, 0.4$, and 0.8, the microparticle is picked up and transported to the end of the wettability gradient region, which takes more time for a larger friction coefficient. However, when f_s is increased to 1.6, the microparticle is picked up by a droplet at the beginning but is not able to be transported to the hydrophilic end $x = 40$. Midway through the transport, at about $x = 20$,

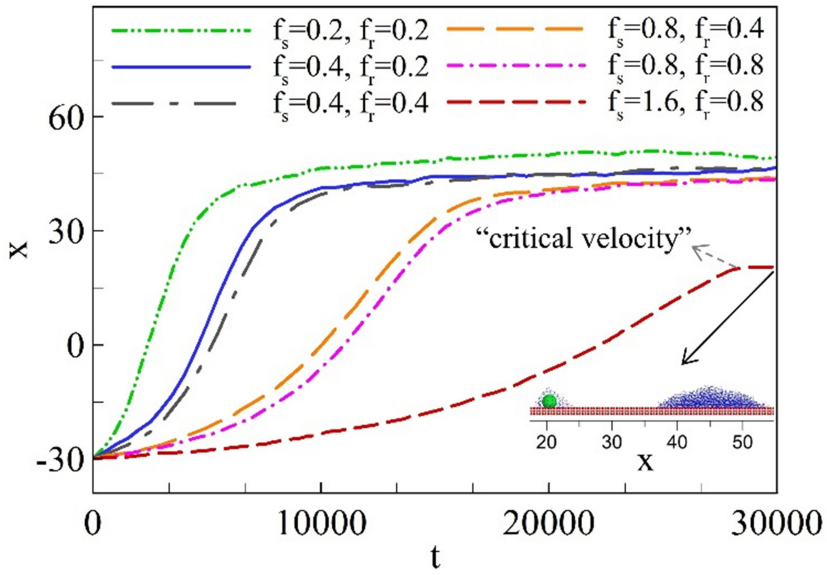

Figure 4.5: Time history of microparticle x-position using different friction coefficients. The inset shows the position of microparticle and droplet at $t = 30,000$, using $f_s = 1.6$, $f_r = 0.8$. Reprinted with permission from [194]. Copyright 2015 American Chemical Society.

the microparticle is dropped off from the droplet and stays there with a few liquid beads attached, as the subfigure shows in Fig. 4.5. This drop-off of the microparticle happens at the position where the maximum slope is observed in its trajectory in Fig. 4.5, which is called critical velocity. To eliminate the randomness from the statistical process, four repeated runs were made for this case using the same parameters, and the drop-off of the microparticle happens in all repeated runs at almost the same location (1% difference). Our hypothesis is that the drop-off of the microparticle and the breakup of the droplet are related to the critical velocity of the droplet. Below the critical velocity, the droplet can carry the microparticle. Beyond the critical velocity, the instantaneous acceleration of the microparticle is less than that of the droplet, which will result in a difference of velocity between the microparticle and the droplet. Finally, the microparticle is dropped off from the droplet and some liquid enveloping the microparticle is separated from the main droplet and remains attached on the surface of the microparticle. To validate our hypothesis, more studies are performed in the following section to better understand physics underlying the occurrence of microparticle drop-off.

In the previous cases, the microparticle is observed to be dropped off from the droplet when the substrate microparticle friction increases to a certain large value. To understand this phenomena better, the driving force and friction force on the microparticle will be analyzed at different locations along the path under different friction coefficients. For this part, we also use the quasi-stationary method to sample and average out the microparticle's velocity, as well as relevant forces. Each value in the following content is averaged out over five repetitive runs, with 2,000,000 time steps used for each run. In the first group of cases, the results for the forces and velocity at location $x = -5$ and

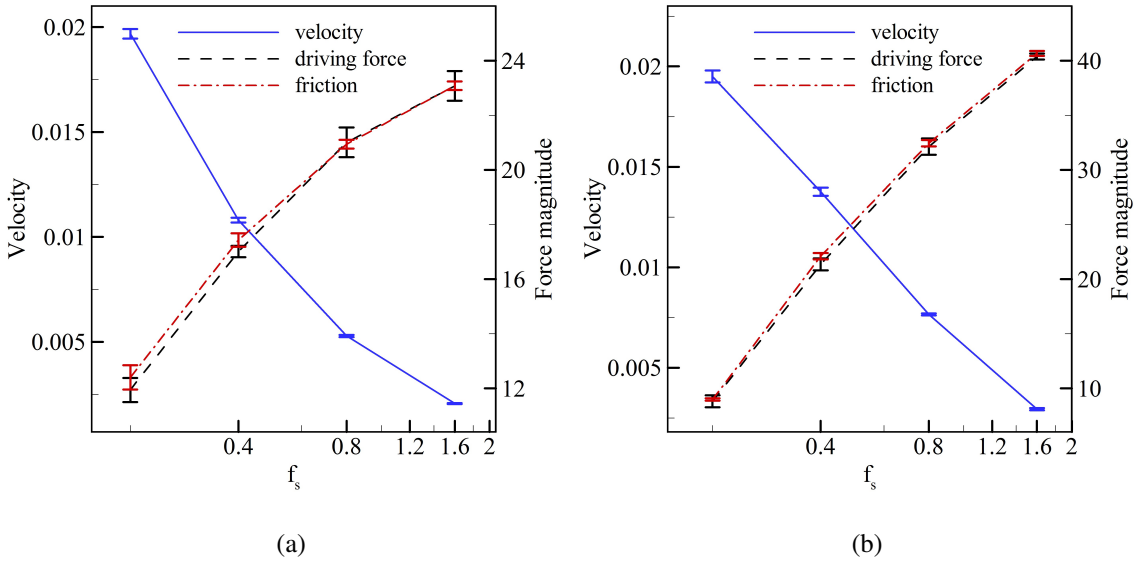

Figure 4.6: The driving force from the droplet on the microparticle, the friction force from the substrate on the microparticle, and the velocity of the microparticle with different f_s at (a) $x = -5$ and (b) $x = 15$.

$x = 15$ with different values of friction coefficient f_s are shown in Fig. 4.6. At both locations, as f_s becomes larger, the friction force between the microparticle and the wall becomes larger as well, which requires a larger driving force to keep the motion. The transport velocity naturally becomes smaller due to larger resistance.

For the second group of comparison, the velocity and forces at different locations along the transport path are recorded using $f_s = 0.4$ and $f_s = 0.8$, as shown in Fig. 4.7. The driving force and friction force on the microparticle are always close to each other, and there is a positive correlation between the velocity and the forces in both figures. As velocity first increases and then decreases along the path from $x = -15$ to $x = 15$ at $f_s = 0.4$ in Fig. 4.7a, the variation of forces shows the same trend. As $f_s = 0.8$ in Fig. 4.7b, the velocity is always increasing though at a decreasing rate, and the forces show an increasing trend as well. A clearer trend can be observed in Fig. 4.8, as f_s is increased to 1.6. The data points are sampled from $x = -15$ to $x = 5$ before the occurrence of the drop-off of the microparticle from the droplet. From the trends in Fig. 4.8, the forces and velocity are monotonically increasing, which are typically different from the trends in Fig. 4.7, especially in Fig. 4.7a for $f_s = 0.4$. The maximum force magnitudes in this case are higher than those in all previous cases mentioned. As mentioned previously, the driving force on the droplet is provided from the wettability gradient of the substrate, which is always strong enough to move the droplet forward. However, the driving force on the microparticle is due to the interactions from liquid particles, which is limited by the cohesive attraction of the droplet. Hence, when the required driving force keeps increasing and finally goes beyond the maximum value the droplet can provide,

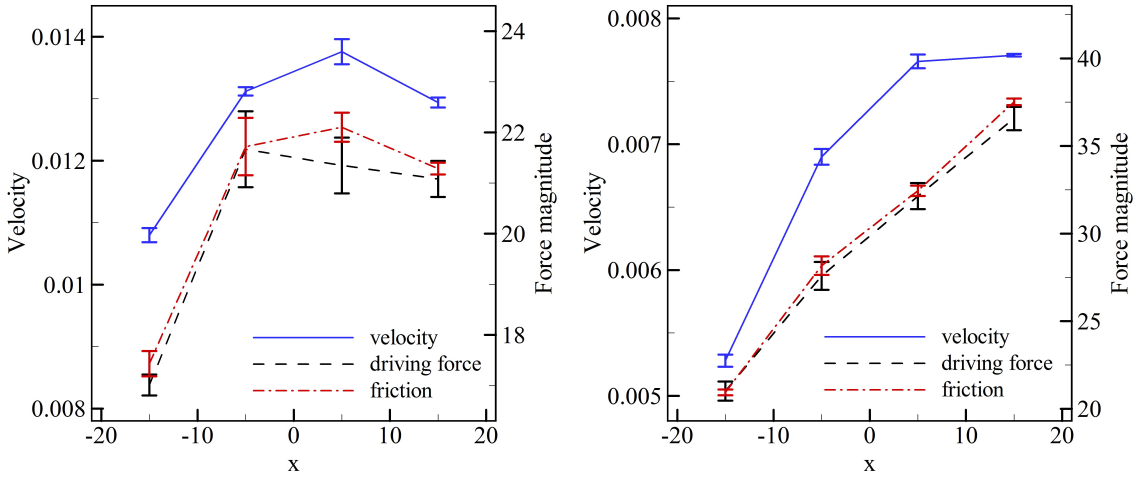

Figure 4.7: The driving force from the droplet on the microparticle, the friction force from the substrate on the microparticle, and the velocity of the microparticle at different locations using (a) $f_s = 0.4$ and (b) $f_s = 0.8$.

the microparticle cannot keep pace with the droplet, and it will be dropped off from the droplet with some liquid particles attached.

4.2 Effects of different factors on the delivery of a single hydrophobic microparticle

From the results in Fig. 4.5 in the previous section, strong friction ($f_s = 1.6$) is found to give rise to the drop-off of the microparticle from the droplet. As introduced in Chapter 1, the continuous transport of the microparticle without drop-off and the accurate delivery (drop-off) of the microparticle are both useful and necessary ways to complete certain biological and medical implementations. In order to better avoid or control this drop-off, more studies are conducted in this section to develop the understanding of the drop-off mechanism. From the results and discussions in the previous subsections, it is already known that droplet size and microparticle hydrophilicity can strongly influence the motion of the microparticle. So the effects of droplet size and microparticle hydrophilicity on the drop-off of the microparticle will be studied in the following subsections.

4.2.1 Droplet size

Following the parameters and setups in Subsection 4.1.3, the effect of droplet size on the drop-off process is studied by using four different radii of droplets: $R_l = 5$, 6, 7, and 8. The friction

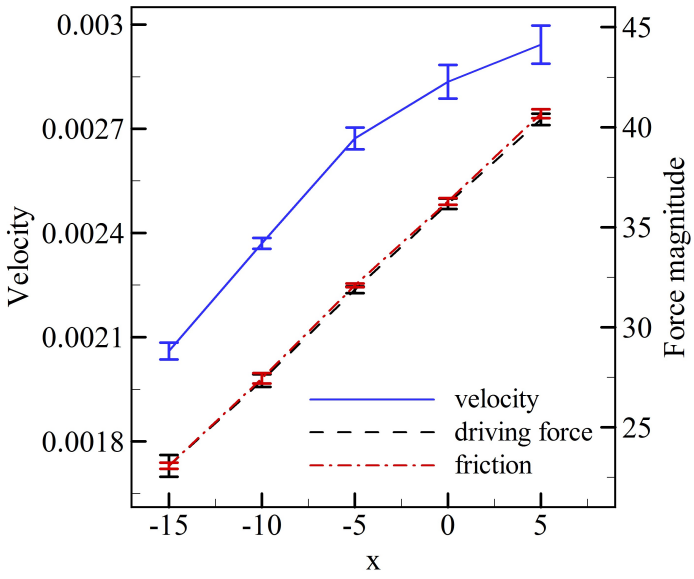

Figure 4.8: The driving force from the droplet on the microparticle, the friction force from the substrate on the microparticle and the velocity of the microparticle at different locations from $x = -15$ to $x = 5$ using $f_s = 1.6$.

coefficients are $f_s = 1.6$ and $f_r = 0.8$. The results of one representative run for each case are compared in Fig. 4.9. For all four cases, the microparticle is dropped off before reaching $x = 40$, where the wettability gradient ends. As droplet size becomes larger, the drop-off of the microparticle occurs at an earlier time as well as at a closer location from the hydrophobic end (starting location). This can be explained from the results and analysis of the transport processes in Subsection 4.1.1. As the droplet size increases, the driving force on the droplet from the wall is increased, but not the driving force on the microparticle from the droplet, which is determined by mutual interactions between the droplet and the microparticle. So, as the droplet size increases, the droplet motion together with the microparticle is faster due to the larger driving force from the substrate, and then the critical velocity for drop-off is reached faster at a shorter distance.

Another commonality worth noting from Fig. 4.9 is that, for all four cases, the velocity is always increasing as the trajectory is always bending upward (concave up) until the occurrence of drop-off. Though it is not possible to measure the critical velocity and the critical driving force that the droplet can provide using the quasi-stationary statistical method, there is still another rough way to determine the critical velocity from the trajectory of the microparticle. To be more specific, the critical velocity can be estimated using quadratic equations to fit the curvature portion before the occurrence of the drop-off. Five repetitive runs are conducted for each size of droplet $R_l = 5$, 6, 7, and 8. From the results in Table 4.1, it can be seen that the critical velocities differ only as much as

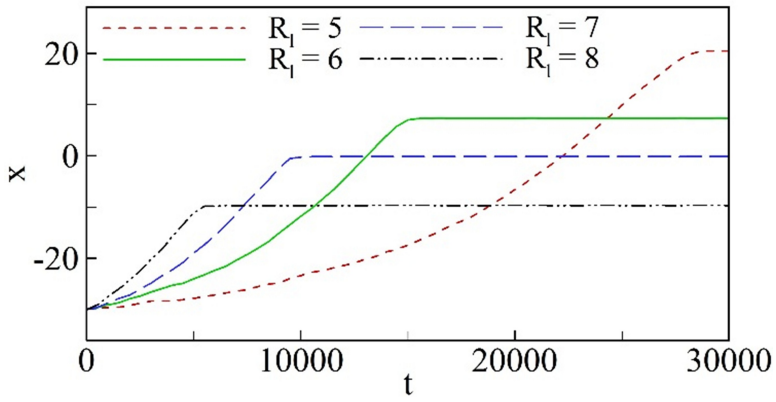

Figure 4.9: Time history of transport of the microparticle under strong friction using different droplet sizes. Reprinted with permission from [194]. Copyright 2015 American Chemical Society.

Table 4.1: Critical velocity for the drop-off of the microparticle using different sizes of droplets

Radius of droplet	Critical velocity
5	$0.00420 \pm 2.24 \times 10^{-5}$
6	$0.00429 \pm 1.87 \times 10^{-5}$
7	$0.00438 \pm 2.55 \times 10^{-5}$
8	$0.00433 \pm 2.74 \times 10^{-5}$

6% from each other. This is reasonable because the drop-off of the microparticle only depends on the cohesive force of the droplet, which is a liquid property that cannot be affected by the droplet geometry.

4.2.2 Wetting property of the microparticle

Following the parameters and setups in Subsection 4.1.3, the effect of the wetting property of the microparticle on the drop-off process is studied with four different values of A_{ls}, i.e., -15, -16, -17, and -18, respectively. The friction coefficients are $f_s = 1.6$ and $f_r = 0.8$. The results of transport processes of the microparticle are compared in Fig. 4.10. For both case $A_{ls} = -18$ and case $A_{ls} = -17$, the microparticle is not dropped off during the transport processes. For the case with $A_{ls} = -18$, the microparticle is pulled away from the surface of the substrate so that the friction between the microparticle and the substrate surface disappears (see inset (a) in Fig. 4.10). For the case $A_{ls} = -17$, the microparticle remains in contact with the substrate surface and stays in the receding region of the droplet during the transport process (see inset (b) in Fig. 4.10). Due to the friction between the microparticle and the substrate surface for the case $A_{ls} = -17$, it takes

a much longer time (seven times longer) for the microparticle to travel from $x = -30$ to $x = 40$ compared with the case $A_{ls} = -18$. For the case $A_{ls} = -16$, the drop-off of the microparticle occurs at the same x location compared with the case $A_{ls} = -15$, but at an earlier time due to larger average velocity. The satellite droplet in the case with $A_{ls} = -16$ continues to move the microparticle toward the hydrophilic end at an extremely low speed (see inset (c) in Fig. 4.10).

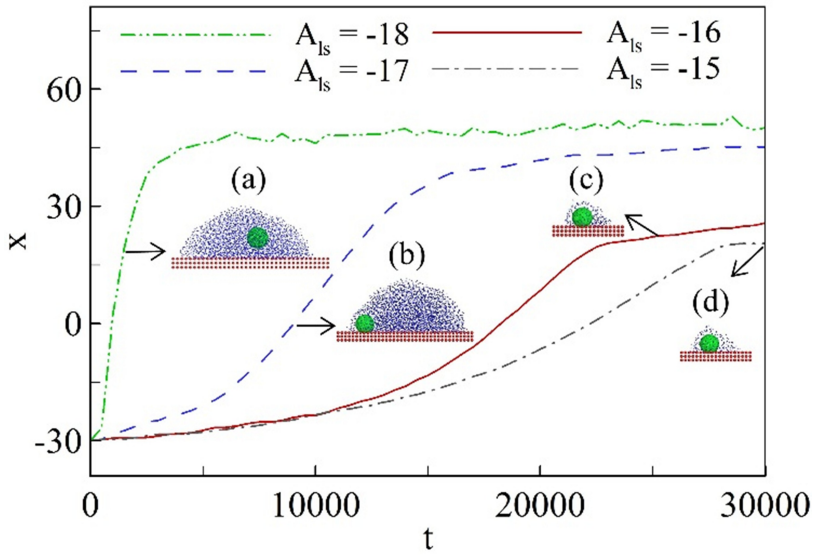

Figure 4.10: Time history of transport of the microparticle under strong friction using different attraction parameters A_{ls}. Inset (a): Relative position of the microparticle and the droplet in the case of $A_{ls} = -18$; Inset (b): Relative position of the microparticle and the droplet in the case of $A_{ls} = -17$ at $t = 9050$; Inset (c): The satellite droplet attached on the microparticle in the case of $A_{ls} = -16$ at $t = 25500$; Inset (d): The satellite droplet attached on the microparticle in the case of $A_{ls} = -15$ at $t = 29500$. Reprinted with permission from [194]. Copyright 2015 American Chemical Society.

4.3 Controllable delivery of a single hydrophobic microparticle

As introduced in Chapter 1, the transport and controllable delivery of microparticles is of critical importance to many medical and biological applications. The transport of droplets and microparticles carried by droplets has already been experimentally performed in digital microfluidics systems by alternatively switching the potentials of a series of electrodes along the designated path. However, to accurately control the delivery of microparticles, either a mechanical trap design or an extra magnetic field is required, adding to the complexity of the digital microfluidics system. So, in this section, two different designs are tested numerically for the controllable delivery of a single microparticle without the addition of traps or magnetic fields. To be more specific, only a single

hydrophobic microparticle will be studied here, since the drop-off of a hydrophobic microparticle has already showed up in the previous studies. By designing and tuning the potential of electrodes or wettability gradient along the designated path, the delivery of a hydrophobic microparticle can be controlled utilizing the friction between the microparticle and the wall. However, for a hydrophilic microparticle, it is pretty difficult to separate it from a droplet without any other external forces because, as previous results have shown, it tends to stay inside the core area of the droplet.

In the previous subsections, the effects of droplet size and the wettability property of a microparticle on its transport and delivery/drop-off have already been analyzed. Based on these results, two designs for trap-free delivery of a hydrophobic microparticle ($A_{ls} = -15$) will be demonstrated in the following numerical simulations. For both designs, the main purpose is to demonstrate the controllable delivery, not necessarily the delivery after a long distance of transport, so a short distance of transport will be designed to minimize the computational cost.

4.3.1 Passive delivery

The first method is to utilize the previous results for the drop-off of the microparticle directly, which is called "passive delivery". The location and wettability condition when the microparticle is dropped off on the wall with strong friction $f_s = 1.6$ and $f_r = 0.8$, have already been obtained for different droplet sizes. So if the designated area for drop-off is coated with this specific wettability condition, the microparticle is expected to be dropped off there. The requisite for this method is that the friction must be strong enough to cause the drop-off and that we have to know beforehand exactly where the microparticle will be dropped off under such strong friction for a certain size of droplet.

To implement the passive delivery of a microparticle, a droplet of radius 7 is used. The hydrophilicity of the microparticle is $A_{ls} = -15$, as mentioned above. The initial x positions of the droplet and the microparticle are still -40 and -30, respectively. The strong frictions are needed to cause the dropoff, set as $f_s = 1.6$, $f_r = 0.8$. The designated location for dropping off the microparticle is $x = -15$, or the region between $x = -17.5$ and $x = -12.5$ (see Fig. 4.11), given some statistical uncertainty for drop-off. To achieve that goal, the wettability gradient of the substrate is specially designed, as given by

$$A_{lw} = \begin{cases} -8.765 & x < -40.0 \\ -1.211 - \sqrt{373.769 + 7.917x} & -40.0 < x \leq -20.0 \\ -1.211 - \sqrt{306.194 + 4.539x} & -20.0 < x \leq 25.1 \\ -21.707 & x > 25.1 \end{cases} \tag{4.1}$$

This wettability design can be achieved by using either EWOD or permanent surface coatings [24, 170]. With this design, the microparticle is expected to be transported quickly from $x = -40$ to $x = -20$ by the stronger wettability gradient than that in Subsection 4.2.1, to save computation time. Though a stronger wettability gradient is applied for this region, the critical velocity will not be reached inside this short region to allow the microparticle to be safely transported through this region. After that, the same wettability gradient as that in Subsection 4.2.1 is applied from $x = -20$ to $x = 25.1$ to make the microparticle's velocity continue to increase but more smoothly. Based on

the result in Subsection 4.2.1, the microparticle is expected to be dropped off near $x = -15$.

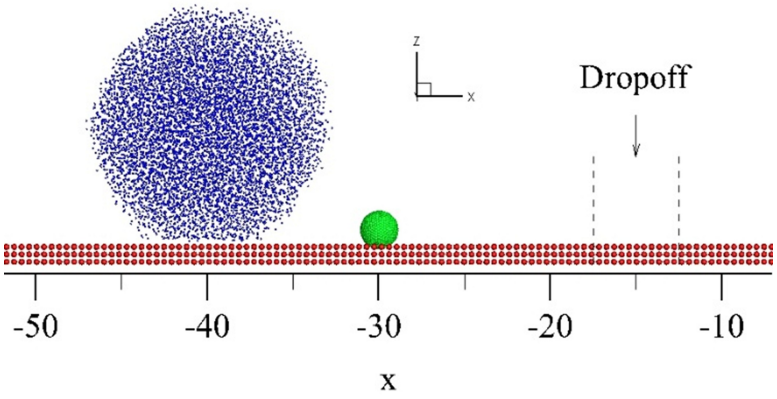

Figure 4.11: Initial setup of liquid droplet (blue) and solid microparticle (green) resting on the wall (red)

Figure 4.12 shows the time history of the manipulation processes with six insets to show the shape and positions of the microparticle and the droplet at six different times (t = 1700, 2300, 2700, 3100, 3300, and 3500 for insets (a) - (f), respectively). During the transport process, the hydrophobic microparticle remains in contact with the wall and stays in the receding region of the droplet as expected. The microparticle is picked up at $x = -30$ and moves together with the droplet (see insets (a) and (b) in Fig. 4.12). When it moves to the designated region between $x = -17.5$ and $x = -12.5$ (see insets (c), (d), (e), (f) in Fig. 4.12), the microparticle detaches gradually from the droplet and stays in that designated region. The droplet continues to move to the hydrophilic end of the wettability region by itself.

From the results above, the goal of the controlled delivery to the designated area is achieved, though there is no good way to control the specific location where the microparticle will be dropped off. This is because the interactions between microparticle and liquid beads are a stochastic process, so that it is hard to determine the location or state for drop-off. For this passive delivery design, the prediction or control of the location of drop-off is totally based on our results and knowledge beforehand. So the limitation is that, in order to implement this method, cases using the exact same parameters have to be conducted in advance to find out the drop-off location or wettability condition under certain specific conditions, including friction conditions, droplet sizes, and so on.

4.3.2 Active delivery

After the discussion on passive delivery of a microparticle, an advanced delivery system was designed to actively control the dropoff location for the microparticle. The second proposed method, which is called “active delivery”, is more flexible to control the dropoff location requiring less knowledge beforehand but uses more complex designs for the wettability gradient. The droplet

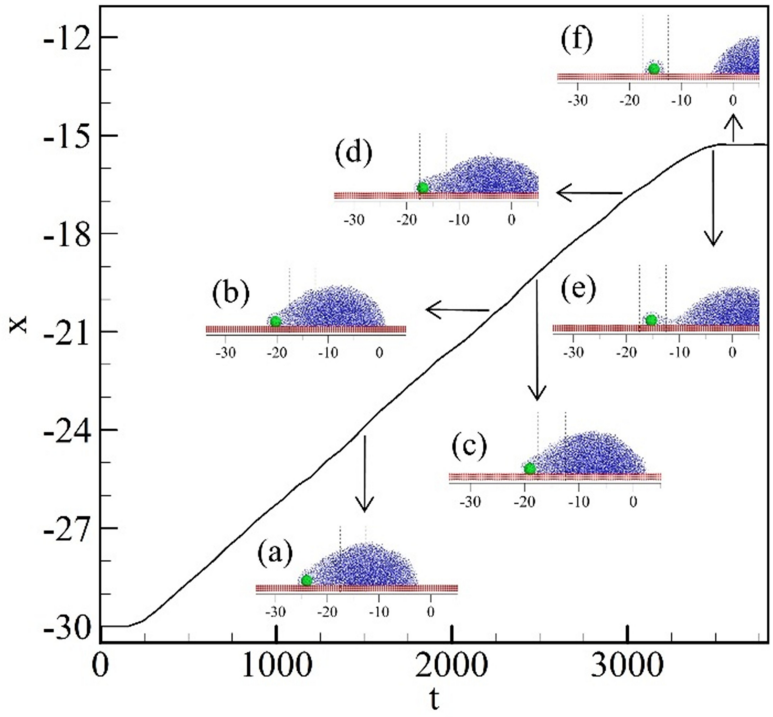

Figure 4.12: Time history of the manipulation of the microparticle with a droplet. The six insets show the shapes and positions of the microparticle and droplet at six different times: (a) $t = 1500$; (b) $t = 2280$; (c) $t = 2520$; (d) $t = 3000$; (e) $t = 3480$; (f) $t = 3600$.

is expected to transport and drop off the microparticle to the designaged location, which can be any position along the path of the transport process. To achieve that goal, enough forces of friction, but not necessarily very strong friction, are needed. The initial x positions of the droplet and the microparticle are still -40 and -30, respectively. The designated location for dropping off the microparticle is between $x_f = -2$ and $x_f = 2$. The droplet size is $R_l = 5$ and the friction is $f_s = 0.8$ and $f_r = 0.4$, with other parameters the same as those in the passive delivery case in the previous subsection, except for the design of the wettability gradient, which will be given in details later.

To implement a controlled delivery of a microparticle, the whole process is divided into two stages. In stage 1, the droplet is driven to move in the x direction, picking up and carrying the microparticle to the destination near $x = 0$. In stage 2, the microparticle is separated from the droplet and remains in the drop-off region ($-2 \le x \le 2$) while the droplet is moved away. For each stage, the wettability gradient of the substrate is specially designed.

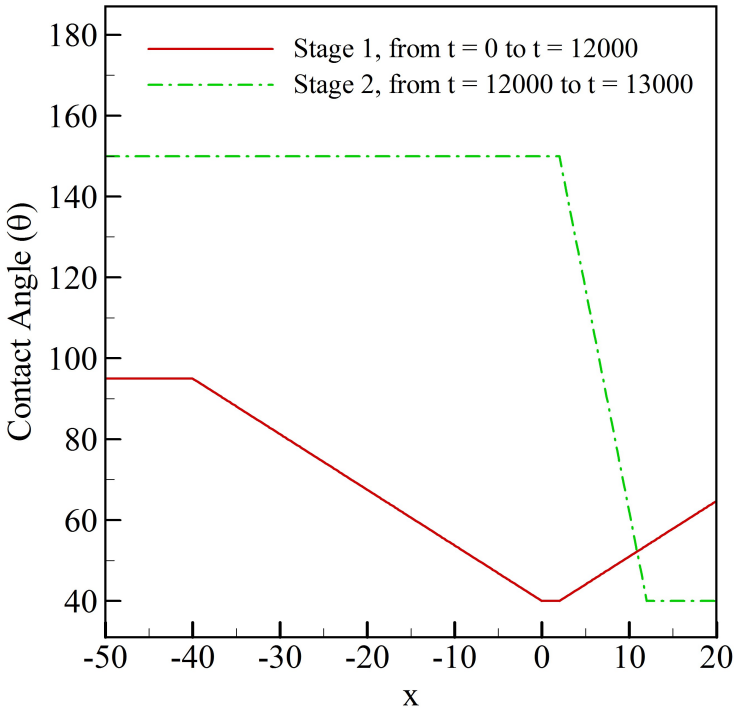

Figure 4.13: Distribution of the contact angle along the substrate in two stages. Reprinted with permission from [194]. Copyright 2015 American Chemical Society.

In stage 1, the wettability parameter A_{lw} is designed as

$$A_{lw} = \begin{cases} -16.66 & x \le -40 \\ -1.211 - \sqrt{420.11 + 4.54x} & -40 < x \le 0 \\ -21.71 & 0 < x \le 2 \\ -1.211 - \sqrt{429.19 + 4.54x} & x > 2 \end{cases} \tag{4.2}$$

The corresponding distribution of the contact angle is shown in Fig. 4.13. The key design of the wettability gradient of the substrate in stage 1 is to have a "V-shape" distribution of the contact angle with a valley near $x = 0$ so that the droplet and the microparticle will stop near $x = 0$. For $x \le -40$, the contact angle keeps a constant of 95°. In the region of $40 \le x < 0$, the contact angle (θ) decreases linearly from 95° to 40°. A moderate wettability gradient ($-55°$ per 40 unit x) is applied here for two reasons: (1) a large wettability gradient may lead to unintended early drop-off of the microparticle before reaching the destination; and (2) it takes a long time for controlled delivery with a small wettability gradient that only generates a weak capillary driving force. The reversed wettability gradient for $x > 2$ is designed to generate capillary force pointing in the negative x direction, which functions as a break to stop the droplet movement. With this design, the droplet center is expected

to stop at $x = 1$ due to the symmetry of the wettability gradient around that position. Considering the fact that the hydrophobic microparticle tends to stay in the receding region of the droplet, the stop position of the microparticle is expected to be around $x = 0$. The time assigned for stage 1 is 12,000, which is much longer than the droplet travel time ($\sim$ 8000) from $x = -40$ to $x = 1$. This extra-long time is to ensure that the droplet and the microparticle will absolutely reach to and stop at their designated locations.

The target for the second stage is to separate the microparticle from the droplet. The microparticle is expected to be kept around $x = 0$ as the droplet is moved away. With the above consideration, a specially designed wettability distribution is given in stage 2:

$$A_{lw} = \begin{cases} -8.77 & x \leq 2 \\ -1.21 - \sqrt{-15.53 + 36.30x} & 2 < x \leq 12 \\ -21.71 & x > 12 \end{cases} \tag{4.3}$$

The corresponding contact angle distribution is also plotted in Fig. 4.13. For $x \leq 2$, the contact angle keeps at a constant of 150°. In the region of $2 < x \leq 12$, the contact angle linearly decreases from 150° to 40°. For such a high wettability gradient exerted on only the advancing portion of the droplet, it is expected that the droplet will separate from the microparticle quickly without dragging the microparticle forward. The time for stage 2 is from 12,000 to 13,000, which is long enough for the droplet to separate from the microparticle and move away. This two-stage wettability design can only be achieved by using EWOD due to the required switching of wettability distribution/electrode potentials, which is not possible for permanent surface coatings technique [24, 170].

Here, we assume the switch time for the surface wettability (or electrode potentials in experimental setups) from stage 1 to stage 2 is extremely short so that the droplet shape will not change during the switch time. With this assumption, we conduct the numerical simulation for stage 1 and stage 2 while ignoring the transition time. The main purpose is to demonstrate the controlled delivery of the microparticle to the destination, including the pickup, transport, and drop-off processes. Figure 4.14 shows the time history of the microparticle position. Three insets in Fig. 4.14 show the shapes and positions of the microparticle and the droplet at 3 different times (t = 9000, 12,100 and 13,000 for insets (a) - (c), respectively). In stage 1, the microparticle is picked up by the droplet and transported to the position $x = 2.30$. At $t = 9000$, the droplet and the microparticle completely stop, and their positions and status are shown in inset (a) in Fig. 4.14. At $t = 12000$, the wettability gradient suddenly changes from stage 1 to stage 2. A strong wettability gradient is imposed on the advancing portion of the droplet to quickly move away the droplet itself. Inset (b) in Fig. 4.14 shows the status of the droplet and the microparticle near the end of the separation at $t = 12100$. The microparticle is dragged forward a little bit from $x = -2.3$ to $x = 1.5$ by the droplet before the complete separation. After that, the main droplet moves while the microparticle enveloped by the satellite droplet is dropped off at $x = -1.5$ (see inset (c) in Fig. 4.14). Using precise control of substrate wettability in two stages, we successfully demonstrate an active trap-free delivery of the hydrophobic microparticle to a destination on the substrate with a droplet carrier in the numerical simulation.

Comparing these two designs for controllable delivery, the active delivery is more flexible for parameter setup and does not require too much knowledge beforehand as that in passive delivery.

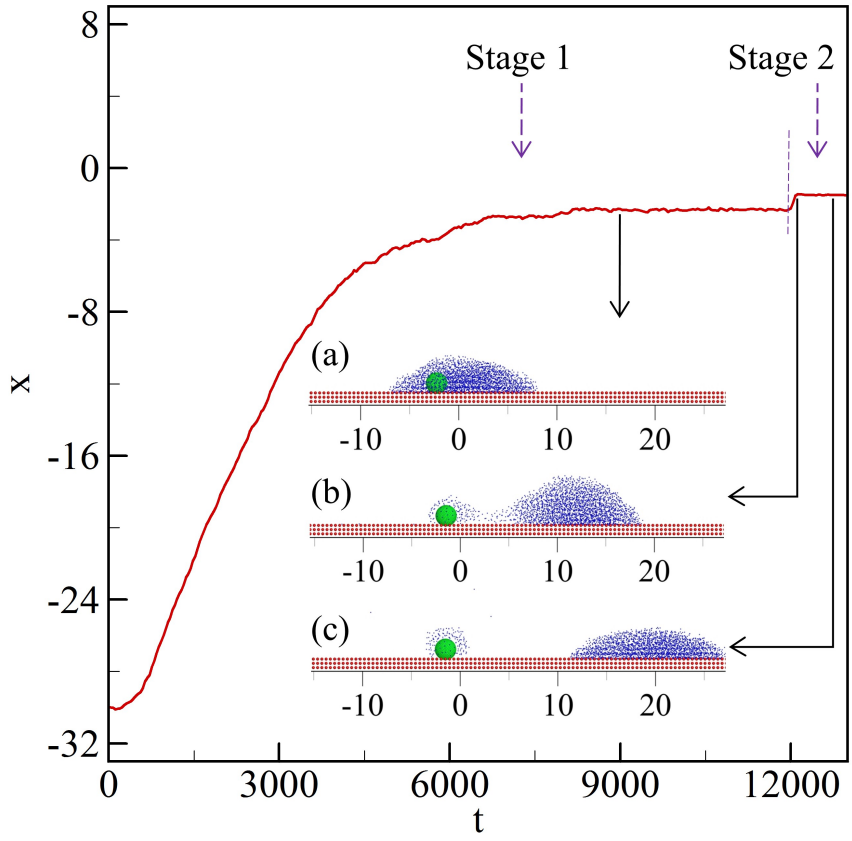

Figure 4.14: Time history of the manipulation of the microparticle with a droplet. Three insets show the shapes and positions of the microparticle and droplet at three different times: (a) t = 9000; (b) t = 12100; (c) t = 12800. The droplet is shown in blue and the solid microparticle is green. Reprinted with permission from [194]. Copyright 2015 American Chemical Society.

The main idea for active delivery is to transport and stop the microparticle in a designated area. After that, the droplet is quickly and accurately dragged away by a strong wettability gradient, so that the microparticle is left behind. The key requirement for active delivery is the accurate prediction of the location of the microparticle and wettability gradient region in the second stage, which requires an accurate control of the switching of electrode potentials in experimental implementations. On the other hand, the passive delivery design does not need to switch the wettability gradient during the process. So it does not require such a switch of electrode potential in the experimental setups, and it can even be fabricated as a device without usage of electrodes.

4.4 Conclusion

In this chapter, in order to obtain a better understanding of the manipulation (pickup, transport, and drop-off) mechanisms of a single microparticle in a digital microfluidic (DMF) system, we numerically studied the interaction among a solid microparticle, a solid substrate, and a liquid droplet using MDPD simulations by varying different control parameters. The droplet can be used as a carrier to pick up, transport, and deliver a single microparticle to a designated destination.

We conducted parametric studies to investigate the effects on the manipulation of the microparticle from the droplet size, wetting properties of the microparticle, and particle-substrate friction coefficients. The results show that the microparticle manipulation processes are significantly affected by these parameters. First, an increase in droplet size will speed up the microparticle delivery process due to the larger contact area between the droplet and the wall. Second, as the microparticle becomes more hydrophilic, the transport process is also accelerated, but for different reasons. It is also found that the relative positions of the microparticle inside the droplet are different for hydrophobic and hydrophilic microparticles during the manipulation processes. For the hydrophobic microparticle, it remains in contact with the substrate surface in the receding region of the droplet, which retards the transport process due to the friction between the microparticle and the substrate. For the hydrophilic microparticle, it is lifted up from the substrate surface so that the friction disappears and the motion is accelerated. After studying the effects of droplet size and the wetting properties of the microparticle, it is also found that the increase of particle-substrate friction coefficients can lead to drop-off of a hydrophobic microparticle during the transport process. This is because both the driving force and friction force increase with velocity, and the drop-off occurs when the limited cohesive force inside the droplet to drive the microparticle is not strong enough to overcome the continuously increasing friction force. This drop-off of the microparticle can be affected by the droplet size and the wettability of the microparticle. By using a larger size of droplet, the drop-off cannot be prevented, but the drop-off location is found to be closer to the starting position. The critical velocity, which is defined as the instantaneous velocity of the microparticle right before the occurrence of drop-off, is measured by curve fitting of the trajectory curve using different sizes of droplets. From the comparison, it is found that the critical velocity is about the same for different sizes of droplets. This is consistent with our previous analysis, because by increasing droplet size, only the driving force on the droplet is increased, not the driving force on the microparticle, which is provided and limited by the cohesive force inside the droplet regardless of the geometry. By changing the wetting property of the microparticle, however, the drop-off can be prevented when the microparticle is more hydrophilic. As the microparticle becomes more and more hydrophilic, the friction force can be reduced and even eliminated if the microparticle is hydrophilic enough to be engulfed in the droplet.

Based on the numerical results above, these sensitive parameters, including the droplet size and particle-substrate friction coefficients, can be used to guide the design of DMF systems for the controllable delivery of single hydrophobic microparticles without any trap structures or external forces. Two different designs, namely passive delivery and active delivery, have been demonstrated to be capable of controlling the location for the delivery of single hydrophobic microparticle without any trap design or external field forces. The active delivery is achieved by accurately and swiftly switching the wettability gradient near the droplet, while the passive delivery requires knowledge beforehand to predict the location for drop-off, which needs enough results from auxiliary cases

using the same parameters. However, these designs cannot be applied for hydrophilic microparticles, because the hydrophilic ones are engulfed in the core area of the droplet and have no more contact with the wall. Thus the friction between the microparticle and the wall cannot be utilized to immobilize the microparticle.

These numerical results provide a fundamental understanding of interactions among the microparticle, the droplet, and the substrate to facilitate the optimal design of a digital microfluidic system utilizing microparticles. Based on these, better control of the pickup, transport, and drop-off of microparticles can be achieved. Especially, two trap-free designs for the delivery of a hydrophobic microparticle is demonstrated through the numerical simulations, which provide a new technique for the manipulation of hydrophobic microparticles in the DMF design.

Chapter 5

Summary and Future Work

5.1 Concluding Remarks

The main objective and main contribution of this research is to study the manipulation of microparticles by droplets using numerical tools. The droplet is used as a carrier to pick up, transport, and deliver a microparticle to a designated destination. From a numerical perspective, this problem incorporates several difficulties together, including the free interface between liquid and air, solid-solid contact between microparticles and substrates, liquid flow with finite size particles, and thermal fluctuations. After analysis of the strengths and shortcomings of different numerical simulation techniques, the MDPD method was adopted as the tool for this numerical study. To validate our code and develop the symmetric boundary condition, Poiseuille flow was first simulated using the DPD method in both 3D and 2D configurations, and the velocity profiles obtained agreed well with predictions based on the fluid's viscosity. In the second validation case, the MDPD method was applied to simulate the motion of a droplet driven by wettability gradients. The droplet velocities at different positions were extracted using the quasi-stationary method, and the values agreed well with theoretical approximations.

After the validation of the current numerical tool, the modeling of a solid microparticle was designed to deal with both solid-liquid interactions and solid-solid interactions. A spherical shell was used to represent the microparticle, and enough beads were packed on the shell surface to avoid the penetration of liquid beads into the microparticle while naturally conserving the momentum during solid-liquid interactions. Then the interaction between the rigid microparticle and the solid wall was modeled based on contact mechanics. The adhesion force, normal force, and friction forces between the microparticle and the wall were considered in our model. When all the relevant forces on the microparticle from both the liquids and the wall were obtained, the translational motion and rotational motion of the microparticle were integrated by summarizing the forces and torques on each bead forming the microparticle. After building up the model of a solid microparticle, a baseline case was conducted to simulate the pickup and transport of a hydrophobic microparticle by a droplet, actuated by the wettability gradient of the wall. The microparticle was dragged by the droplet toward the hydrophilic end, staying on the wall near the air-liquid interface. Due to the contact and frictions between the microparticle and the wall for the whole process, the motion of the droplet was decelerated compared to the motion of a droplet without the microparticle. Using the quasi-

stationary method, the flow structures inside the droplet were found to be greatly different from those of a droplet without a microparticle, especially the flows along the direction the droplet was moving. The liquids behind the microparticle pushed the microparticle forward, and rotational motion of the liquids on both sides of the microparticle dragged it upward. There was a hydrodynamic lift force on the microparticle but not enough to lift it up from the wall.

After the modeling of the solid microparticle and analysis for the baseline case, parametric studies were conducted to investigate the effects of different factors, such as the droplet size, wetting properties of the microparticle, and particle-substrate friction coefficients. To be more specific, the effects of different factors on the pickup, transport, and delivery of the microparticle were investigated. The increase of droplet size sped up the transport process, as larger contact with the wall provides a larger driving force for the motion of the droplet and the microparticle. However, the increase of particle-substrate friction coefficients could lead to drop-off of the hydrophobic microparticle during the transport process. Before the drop-off occurred, both driving force and friction force increased as the velocity increased. In other words, a positive correlation between the velocity and the driving force on the microparticle was observed during the transport process of the microparticle. As the velocity kept increasing, when the friction force, or the required driving force on the microparticle from the droplet, went beyond the maximum driving force the droplet could provide, the microparticle would be dropped off from the droplet with some liquid beads attached. This instantaneous velocity at the instant of drop-off was named critical velocity. The critical velocity was found to be same for different droplet sizes, since it is determined and limited by the cohesive force of the liquid but not the droplet geometry.

Besides the effects of droplet size and friction, the wetting properties of the microparticle also has a great effect on the transport and delivery. For different microparticles, either hydrophobic or hydrophilic, the relative position of the microparticle inside the droplet was totally different during the transport process. For the hydrophobic microparticle, it always stayed in contact with the substrate surface residing in the receding region of the droplet. This contact led to friction between the microparticle and the substrate retarding the transport process. In contrast, the hydrophilic microparticle was lifted up from the substrate surface due to the strong attraction between the liquid and the microparticle, so the friction and possible drop-off of the microparticle no longer existed. Due to this difference, to control the delivery of microparticles, different strategies should be applied for hydrophobic and hydrophilic microparticles. For a hydrophobic microparticle, which is relatively easier to manipulate than a hydrophilic microparticle, we demonstrated two trap-free designs for controllable delivery by a droplet carrier without any other trap design or external forces. The active delivery was achieved by accurately and swiftly switching the wettability gradient near the droplet, while the passive delivery required knowledge beforehand to predict the location for drop-off, which required enough results from auxiliary cases using the same parameters. However, these designs could not be applied for strongly hydrophilic microparticles because these microparticles were engulfed in the core area of the droplet and had no more contact with the wall. Thus the friction between the microparticle and the wall could not be utilized to immobilize the microparticle. The possibility for a design to actively and accurately deliver a single hydrophilic microparticle without trap structures and external forces will be discussed in the following future work section.

The numerical results provide a fundamental understanding of interactions among the microparticle, the droplet, and the substrate, which is beneficial for the optimal design of a digital

microfluidic system for different functions. The MDPD method also provides a valuable numerical tool that can be used to study more physics related to digital microfluidics and microparticles.

5.2 Future Work

Although the manipulation of a single microparticle by a droplet has been thoroughly analyzed in this research, with discussions on the effects of different factors, several aspects need further development and closer examination.

5.2.1 Controllable delivery of single hydrophilic microparticles by droplets

The controllable delivery of microparticles is an important function for many biological and medical applications. In previous results, we have demonstrated the controllable delivery of single hydrophobic microparticles utilizing the friction between the microparticle and the wall, without the assistance of any trap structures or external forces. However, strongly hydrophilic microparticles tend to be lifted up from the wall and absorbed into the droplet, so that the friction cannot be utilized for delivery in this case. To deliver a hydrophilic microparticle, one proposed idea is to successively split the droplet in half until the daughter droplet containing the microparticle is small enough. In experimental designs, various and accurate manipulation of droplets has already been successfully achieved, such as transport, merging, splitting and positioning. However, for droplets containing a single hydrophilic microparticle inside, the accurate positioning of the microparticle is still a challenging objective since the microparticle is floating inside. Based on our current numerical tool, a controllable delivery design for a hydrophilic microparticle can be explored and tested at low cost, which can be beneficial for the experimental designs.

5.2.2 Effects of thermal fluctuations on the manipulation of microparticles

As introduced in Chapter 1, thermal fluctuations are an essential part of fluid mechanical problems at microscopic and mesoscopic length scales [90–95], and this is also one of the reasons why the DPD method is applied for this study. However, by far, we have not explicitly investigated the effects of thermal fluctuations on the manipulation processes of microparticles. Previous researches on droplet motion only [82] found that increasing thermal fluctuations is capable of assisting the droplet motion during the transport, but not changing the final location where the droplet stops. The effect of thermal fluctuations on the transport and deliver of microparticles needs to be investigated.

5.2.3 Manipulation of microparticles by droplet between two parallel plates

Compared with the open system using one plate, the digital microfluidics system using two parallel plates is better in the accurate control of the droplet and keeping the experimental environment uncontaminated. The droplet is sandwiched between two electrode substrates and surrounded by some other immiscible liquid or gas, such as silicone oil, to avoid any contamination or evaporation. Different flow structures can be expected for the droplet motion between two plates, compared

with the results for droplet motion on single substrate. By modifying the geometries and configurations, our current numerical tool is capable of revealing the details for the droplet motion, as well as the manipulation of microparticles using this two-plate system.

5.2.4 Enhanced removal of microparticles by surfactants

For surface cleaning applications, how to enhance the efficient removal of dust particles is the critical objective. The introduction of surfactants can be a feasible way to deal with the removal of hydrophobic particles, which are more difficult to clean by distilled water than hydrophilic particles. The modeling of surfactants in the MDPD scheme needs to be built first. To be specific, the interactions between surfactants and droplets, the interactions between surfactants and substrates, and the interactions between surfactants and microparticles are required to model the whole system.

5.2.5 Removal of microparticles by large droplets driven by gravity

Surface cleaning techniques, or dust removal techniques, are widely used for solar panels in large-scale solar farms, building surfaces and some other glass surfaces. Bioinspired by different species of living nature, both animals and plants, self-cleaning technology by manufacturing superhydrophobic surfaces has rapidly developed since the late 20th century [196–199]. Water droplets can easily roll down these superhydrophobic surfaces, taking the dust particles away with them. With the development of self-cleaning coating technology, self-cleaning and antireflective glasses have also been developed for solar modules to further improve their overall efficiency [200, 201]. However, in a desert environment, the amount of distilled water required for cleaning can still be a big budget. So, to save the usage of water resources and to improve the removal efficiency, the mechanism for the removal of dust and dirt particles by water droplets on superhydrophobic surfaces needs to be studied systematically. Based on our current mesoscopic numerical model, the interactions between microparticles and droplets have already been investigated. However, to apply our current mesoscopic model to the macroscopic droplets ($\geq$ millimeter size) and particles ($\geq$ 100 micrometers), a new scaling method needs to be built, otherwise hundreds of thousands of beads will be required for the simulation, which is a formidable computational task. Another feature to add for the modeling is gravitational force, which will be the driving force for the droplets and microparticles instead of the surface tension force used in mesoscopic digital microfluidics systems.

5.2.6 Modeling of single microparticles using single beads

As for the modeling of solid microparticles in MDPD, there could be other alternatives similar to those in the DPD method, as mentioned earlier. It could be modeled as a solid sphere with beads filling both the surface and the inside of the sphere. Or the spherical microparticle could be represented by a single bead with a large imaginary boundary. In this way, a perfect spherical symmetry could be achieved, and it can also save a great deal of memory storage and calculations for hundreds of beads forming the microparticles, as in our current research. Though the one bead modeling, or point representation of the microparticle is not able to represent any other detailed geometry for the microparticle, this can still be widely used for situations when the microparticle is

quite small compared with the system, as a dust particle compared to a milliliter size droplet mentioned in the previous subsection. For this one-bead modeling, the interaction parameters between the one bead microparticle and liquid beads need to be reestablished, as well as the interactions between the one-bead microparticle and the wall.

5.2.7 Manipulation of magnetic microparticles in digital microfluidics

As introduced in Chapter 1, to have more flexible and precise control, magnetic microparticles, or magnetic beads, are adopted in different biological and chemical applications [29–31]. Based on our current model, we have already investigated the interactions among droplets, microparticles, and walls. And we have also demonstrated the pickup and transport of microparticles by droplets, as well as the delivery of hydrophobic microparticles. By the addition of magnetic forces, the delivery of hydrophilic microparticles can also be achieved. This was accomplished by the addition of a proper field force in our current simulations. This external field force can be turned on or off as requested and its direction can even be switched like rotating the magnetic poles in experimental setups. More flow phenomenon and flexible manipulations can be expected from simulations of droplets with magnetic microparticles.

5.2.8 Manipulation of multiple microparticles by droplet

The interactions between multiple microparticles and cargo droplets can be important for many applications in digital microfluidics and surface cleaning applications. The capability and limitation of the droplet to pick up multiple microparticles on the substrate is critical for particle sampling and removal technologies. The interactions between multiple microparticles and a droplet will be much more complicated to study. For a group of heterogeneous microparticles, the selection of certain category of particles can be performed based on the difference of the wetting properties of the microparticles. This process can be studied numerically based on our current tool, and the flow structures inside the droplet carrying multiple microparticles can be revealed.

5.2.9 Shape extraction for thin film geometry

In Section 2.4.2, the relation between contact angles and interaction parameters has been investigated by extracting the surface profile and fit the contact angle at different parameter values. In order to have a stable measurement, a beautiful and smooth shape, as shown in Fig. 2.11 and Fig. 2.12, is required to extract the geometry profile. However, if the contact angle is as small as about 15° or less (superhydrophilic), the water droplet is spreading very widely on the wall and the thickness of the liquid layer is really small to capture exactly. Also, since there is a randomness in the MDPD method, it is hard to determine a clear exact shape for this really small contact angle. The bead density distribution inside the geometry is not that clear to be determined (compared with Fig. 2.11(b)), in other words, it is prone to be subjective to determine the shape. Due to the randomness of this numerical method, there must be enough bead numbers to be clustered and sampled to extract deterministic information. Therefore, for geometries with thin layers of particles, a better way is needed to get useful information from them, such as for superhydrophilic thin films.

Bibliography

[1] T. M. Squires, S. R. Quake, Microfluidics: Fluid physics at the nanoliter scale, Reviews of modern physics 77 (3) (2005) 977.

[2] G. M. Whitesides, The origins and the future of microfluidics, Nature 442 (7101) (2006) 368–373.

[3] D. J. Beebe, G. A. Mensing, G. M. Walker, Physics and applications of microfluidics in biology, Annual review of biomedical engineering 4 (1) (2002) 261–286.

[4] E. K. Sackmann, A. L. Fulton, D. J. Beebe, The present and future role of microfluidics in biomedical research, Nature 507 (7491) (2014) 181–189.

[5] D. B. Weibel, G. M. Whitesides, Applications of microfluidics in chemical biology, Current opinion in chemical biology 10 (6) (2006) 584–591.

[6] K. S. Elvira, X. C. i Solvas, R. C. Wootton, et al., The past, present and potential for microfluidic reactor technology in chemical synthesis, Nature chemistry 5 (11) (2013) 905–915.

[7] P. S. Dittrich, A. Manz, Lab-on-a-chip: microfluidics in drug discovery, Nature Reviews Drug Discovery 5 (3) (2006) 210–218.

[8] C. Rivet, H. Lee, A. Hirsch, S. Hamilton, H. Lu, Microfluidics for medical diagnostics and biosensors, Chemical Engineering Science 66 (7) (2011) 1490–1507.

[9] P. Neuži, S. Giselbrecht, K. Länge, T. J. Huang, A. Manz, Revisiting lab-on-a-chip technology for drug discovery, Nature reviews Drug discovery 11 (8) (2012) 620–632.

[10] D. Psaltis, S. R. Quake, C. Yang, Developing optofluidic technology through the fusion of microfluidics and optics, Nature 442 (7101) (2006) 381–386.

[11] D. Mark, S. Haeberle, G. Roth, F. von Stetten, R. Zengerle, Microfluidic lab-on-a-chip platforms: requirements, characteristics and applications, Chemical Society Reviews 39 (3) (2010) 1153–1182.

[12] S.-Y. Teh, R. Lin, L.-H. Hung, A. P. Lee, Droplet microfluidics, Lab on a Chip 8 (2) (2008) 198–220.

[13] R. B. Fair, Digital microfluidics: is a true lab-on-a-chip possible?, Microfluidics and Nanofluidics 3 (3) (2007) 245–281.

[14] S. U. Son, R. L. Garrell, Transport of live yeast and zebrafish embryo on a droplet (digital) microfluidic platform, Lab on a chip 9 (16) (2009) 2398–2401.

[15] K. Choi, A. H. Ng, R. Fobel, A. R. Wheeler, Digital microfluidics, Annual Review of Analytical Chemistry 5 (2012) 413–440.

[16] D. Beyssen, L. Le Brizoual, O. Elmazria, P. Alnot, Microfluidic device based on surface acoustic wave, Sensors and Actuators B: Chemical 118 (1) (2006) 380–385.

[17] Y. N. Cheung, N. T. Nguyen, T. N. Wong, Droplet manipulation in a microfluidic chamber with acoustic radiation pressure and acoustic streaming, Soft matter 10 (40) (2014) 8122–8132.

[18] J. Pipper, M. Inoue, L. F. Ng, P. Neuzil, Y. Zhang, L. Novak, Catching bird flu in a droplet, Nature medicine 13 (10) (2007) 1259–1263.

[19] T. Ohashi, H. Kuyama, N. Hanafusa, Y. Togawa, A simple device using magnetic transportation for droplet-based pcr, Biomedical microdevices 9 (5) (2007) 695–702.

[20] P. Y. Chiou, H. Moon, H. Toshiyoshi, C.-J. Kim, M. C. Wu, Light actuation of liquid by optoelectrowetting, Sensors and actuators A: physical 104 (3) (2003) 222–228.

[21] J. Shemesh, A. Bransky, M. Khoury, S. Levenberg, Advanced microfluidic droplet manipulation based on piezoelectric actuation, Biomedical microdevices 12 (5) (2010) 907–914.

[22] T. S. Sammarco, M. A. Burns, Thermocapillary pumping of discrete drops in microfabricated analysis devices, AIChE Journal 45 (2) (1999) 350–366.

[23] S. K. Cho, H. Moon, C.-J. Kim, Creating, transporting, cutting, and merging liquid droplets by electrowetting-based actuation for digital microfluidic circuits, Microelectromechanical Systems, Journal of 12 (1) (2003) 70–80.

[24] Y.-H. Lai, M.-H. Hsu, J.-T. Yang, Enhanced mixing of droplets during coalescence on a surface with a wettability gradient, Lab on a Chip 10 (22) (2010) 3149–3156.

[25] D. Chatterjee, B. Hetayothin, A. R. Wheeler, D. J. King, R. L. Garrell, Droplet-based microfluidics with nonaqueous solvents and solutions, Lab on a Chip 6 (2) (2006) 199–206.

[26] Z. Cao, F. Chen, N. Bao, H. He, P. Xu, S. Jana, S. Jung, H. Lian, C. Lu, Droplet sorting based on the number of encapsulated particles using a solenoid valve, Lab on a chip 13 (1) (2013) 171–178.

[27] F. E. Kruis, H. Fissan, A. Peled, Synthesis of nanoparticles in the gas phase for electronic, optical and magnetic applicationsa review, Journal of Aerosol Science 29 (5) (1998) 511–535.

[28] H. Kawaguchi, Functional polymer microspheres, Progress in Polymer Science 25 (8) (2000) 1171–1210.

[29] M. A. Gijs, Magnetic bead handling on-chip: new opportunities for analytical applications, Microfluidics and Nanofluidics 1 (1) (2004) 22–40.

[30] M. A. Gijs, F. Lacharme, U. Lehmann, Microfluidic applications of magnetic particles for biological analysis and catalysis, Chemical reviews 110 (3) (2009) 1518–1563.

[31] A. van Reenen, A. M. de Jong, J. M. den Toonder, M. W. Prins, Integrated lab-on-chip biosensing systems based on magnetic particle actuation–a comprehensive review, Lab on a Chip 14 (12) (2014) 1966–1986.

[32] J. C. Chow, J. G. Watson, E. M. Fujita, Z. Lu, D. R. Lawson, L. L. Ashbaugh, Temporal and spatial variations of pm 2.5 and pm 10 aerosol in the southern california air quality study, Atmospheric Environment 28 (12) (1994) 2061–2080.

[33] K. He, F. Yang, Y. Ma, Q. Zhang, X. Yao, C. K. Chan, S. Cadle, T. Chan, P. Mulawa, The characteristics of pm 2.5 in beijing, china, Atmospheric Environment 35 (29) (2001) 4959–4970.

[34] N. Englert, Fine particles and human healtha review of epidemiological studies, Toxicology letters 149 (1) (2004) 235–242.

[35] F. Lu, D. Xu, Y. Cheng, S. Dong, C. Guo, X. Jiang, X. Zheng, Systematic review and meta-analysis of the adverse health effects of ambient pm 2.5 and pm 10 pollution in the chinese population, Environmental research 136 (2015) 196–204.

[36] H. A. Burge, W. R. Solomon, Sampling and analysis of biological aerosols, Atmospheric Environment (1967) 21 (2) (1987) 451–456.

[37] W. Griffiths, G. DeCosemo, The assessment of bioaerosols: a critical review, Journal of Aerosol Science 25 (8) (1994) 1425–1458.

[38] H. A. Burge, D. L. Pierson, T. O. Groves, K. F. Strawn, S. K. Mishra, Dynamics of airborne fungal populations in a large office building, Current microbiology 40 (1) (2000) 10–16.

[39] J. Douwes, P. Thorne, N. Pearce, D. Heederik, Bioaerosol health effects and exposure assessment: progress and prospects, Annals of Occupational Hygiene 47 (3) (2003) 187–200.

[40] W. Eduarda, D. Heederik, Methods for quantitative assessment of airborne levels of non-infectious microorganisms in highly contaminated work environments, American Industrial Hygiene Association 59 (2) (1998) 113–127.

[41] Z. Wang, T. Reponen, S. A. Grinshpun, R. L. Górny, K. Willeke, Effect of sampling time and air humidity on the bioefficiency of filter samplers for bioaerosol collection, Journal of Aerosol Science 32 (5) (2001) 661–674.

[42] T. Reponen, K. Willeke, S. Grinshpun, A. Nevalainen, Biological particle sampling, Aerosol Measurement: Principles, Techniques, and Applications, Third Edition (2011) 549–570.

[43] W. Eduard, D. Heederik, C. Duchaine, B. J. Green, Bioaerosol exposure assessment in the workplace: the past, present and recent advances, Journal of environmental monitoring 14 (2) (2012) 334–339.

[44] T. J. Mukoda, L. A. Todd, M. D. Sobsey, Pcr and gene probes for detecting bioaerosols, Journal of aerosol science 25 (8) (1994) 1523–1532.

[45] M. P. Schafer, Detection and characterization of airborne mycobacterium tuberculosis h37ra particles, a surrogate for airborne pathogenic m. tuberculosis, Aerosol science and technology 30 (2) (1999) 161–173.

[46] Y. Zhao, S. K. Cho, Microparticle sampling by electrowetting-actuated droplet sweeping, Lab on a Chip 6 (1) (2006) 137–144.

[47] M. K. Tan, J. R. Friend, L. Y. Yeo, Microparticle collection and concentration via a miniature surface acoustic wave device, Lab on a Chip 7 (5) (2007) 618–625.

[48] Y. Zhao, S. K. Chung, U.-C. Yi, S. K. Cho, Droplet manipulation and microparticle sampling on perforated microfilter membranes, Journal of Micromechanics and Microengineering 18 (2) (2008) 025030.

[49] M. Jönsson-Niedziółka, F. Lapierre, Y. Coffinier, S. Parry, F. Zoueshtiagh, T. Foat, V. Thomy, R. Boukherroub, Ewod driven cleaning of bioparticles on hydrophobic and superhydrophobic surfaces, Lab on a Chip 11 (3) (2011) 490–496.

[50] S. K. Cho, Y. Zhao, et al., Concentration and binary separation of micro particles for droplet-based digital microfluidics, Lab on a Chip 7 (4) (2007) 490–498.

[51] H. Kinoshita, S. Kaneda, T. Fujii, M. Oshima, Three-dimensional measurement and visualization of internal flow of a moving droplet using confocal micro-piv, Lab on a Chip 7 (3) (2007) 338–346.

[52] H.-W. Lu, F. Bottausci, J. D. Fowler, A. L. Bertozzi, C. Meinhart, et al., A study of ewod-driven droplets by piv investigation, Lab on a Chip 8 (3) (2008) 456–461.

[53] S. Ma, J. M. Sherwood, W. T. Huck, S. Balabani, On the flow topology inside droplets moving in rectangular microchannels, Lab on a Chip 14 (18) (2014) 3611–3620.

[54] A. Author, Simulation tools for lab on a chip research: advantages, challenges, and thoughts for the future, Lab on a Chip 8 (9) (2008) 1424–1431.

[55] Y. Sui, H. Ding, P. D. Spelt, Numerical simulations of flows with moving contact lines, Annual Review of Fluid Mechanics 46 (2014) 97–119.

[56] D. Peng, B. Merriman, S. Osher, H. Zhao, M. Kang, A pde-based fast local level set method, Journal of Computational Physics 155 (2) (1999) 410–438.

[57] M. Sussman, A. S. Almgren, J. B. Bell, P. Colella, L. H. Howell, M. L. Welcome, An adaptive level set approach for incompressible two-phase flows, Journal of Computational Physics 148 (1) (1999) 81–124.

[58] P. D. Spelt, A level-set approach for simulations of flows with multiple moving contact lines with hysteresis, Journal of Computational Physics 207 (2) (2005) 389–404.

[59] Y. Chen, R. Mertz, R. Kulenovic, Numerical simulation of bubble formation on orifice plates with a moving contact line, International Journal of Multiphase Flow 35 (1) (2009) 66–77.

[60] C. W. Hirt, B. D. Nichols, Volume of fluid (vof) method for the dynamics of free boundaries, Journal of computational physics 39 (1) (1981) 201–225.

[61] D. Gueyffier, J. Li, A. Nadim, R. Scardovelli, S. Zaleski, Volume-of-fluid interface tracking with smoothed surface stress methods for three-dimensional flows, Journal of Computational Physics 152 (2) (1999) 423–456.

[62] A. Q. Raeini, M. J. Blunt, B. Bijeljic, Modelling two-phase flow in porous media at the pore scale using the volume-of-fluid method, Journal of Computational Physics 231 (17) (2012) 5653–5668.

[63] D. A. Hoang, V. van Steijn, L. M. Portela, M. T. Kreutzer, C. R. Kleijn, Benchmark numerical simulations of segmented two-phase flows in microchannels using the volume of fluid method, Computers & Fluids 86 (2013) 28–36.

[64] E. Aulisa, S. Manservisi, R. Scardovelli, A surface marker algorithm coupled to an area-preserving marker redistribution method for three-dimensional interface tracking, Journal of Computational Physics 197 (2) (2004) 555–584.

[65] E. Coyajee, B. J. Boersma, Numerical simulation of drop impact on a liquid–liquid interface with a multiple marker front-capturing method, Journal of Computational Physics 228 (12) (2009) 4444–4467.

[66] A. Yazdani, P. Bagchi, Three-dimensional numerical simulation of vesicle dynamics using a front-tracking method, Physical Review E 85 (5) (2012) 056308.

[67] P. Seppecher, Moving contact lines in the cahn-hilliard theory, International journal of engineering science 34 (9) (1996) 977–992.

[68] D. Jacqmin, Contact-line dynamics of a diffuse fluid interface, Journal of Fluid Mechanics 402 (2000) 57–88.

[69] M. Ahmadlouydarab, Z.-S. S. Liu, J. J. Feng, Interfacial flows in corrugated microchannels: Flow regimes, transitions and hysteresis, International Journal of Multiphase Flow 37 (10) (2011) 1266–1276.

[70] M. Ahmadlouydarab, Z.-S. S. Liu, J. J. Feng, Relative permeability for two-phase flow through corrugated tubes as model porous media, International Journal of Multiphase Flow 47 (2012) 85–93.

[71] M. Ahmadlouydarab, J. J. Feng, Motion and coalescence of sessile drops driven by substrate wetting gradient and external flow, Journal of Fluid Mechanics 746 (2014) 214–235.

[72] M. Ahmadlouydarab, J. Azaiez, Z. Chen, Dynamics of viscous liquid bridges inside microchannels subject to external oscillatory flow, Physical Review E 91 (2) (2015) 023002.

[73] G. A. Bird, Molecular gas dynamics and the direct simulation of gas flows.

[74] E. Oran, C. Oh, B. Cybyk, Direct simulation monte carlo: recent advances and applications 1, Annual Review of Fluid Mechanics 30 (1) (1998) 403–441.

[75] A. L. Garcia, J. B. Bell, W. Y. Crutchfield, B. J. Alder, Adaptive mesh and algorithm refinement using direct simulation monte carlo, Journal of computational Physics 154 (1) (1999) 134–155.

[76] J. Dawson, One-dimensional plasma model, Physics of Fluids (1958-1988) 5 (4) (1962) 445–459.

[77] J. M. Dawson, Particle simulation of plasmas, Reviews of modern physics 55 (2) (1983) 403.

[78] J. P. Verboncoeur, Particle simulation of plasmas: review and advances, Plasma Physics and Controlled Fusion 47 (5A) (2005) A231.

[79] A. K. Das, P. K. Das, Simulation of drop movement over an inclined surface using smoothed particle hydrodynamics, Langmuir 25 (19) (2009) 11459–11466.

[80] A. Das, P. Das, Multimode dynamics of a liquid drop over an inclined surface with a wettability gradient, Langmuir 26 (12) (2010) 9547–9555.

[81] J. Huang, C. Shu, Y. Chew, Numerical investigation of transporting droplets by spatiotemporally controlling substrate wettability, Journal of colloid and interface science 328 (1) (2008) 124–133.

[82] Z. Li, G.-H. Hu, Z.-L. Wang, Y.-B. Ma, Z.-W. Zhou, Three dimensional flow structures in a moving droplet on substrate: A dissipative particle dynamics study, Physics of Fluids (1994-present) 25 (7) (2013) 072103.

[83] H. H. Hu, D. D. Joseph, M. J. Crochet, Direct simulation of fluid particle motions, Theoretical and Computational Fluid Dynamics 3 (5) (1992) 285–306.

[84] H. H. Hu, Direct simulation of flows of solid-liquid mixtures, International Journal of Multiphase Flow 22 (2) (1996) 335–352.

[85] N. A. Patankar, P. Singh, D. D. Joseph, R. Glowinski, T.-W. Pan, A new formulation of the distributed lagrange multiplier/fictitious domain method for particulate flows, International Journal of Multiphase Flow 26 (9) (2000) 1509–1524.

[86] R. Glowinski, T. Pan, T. Hesla, D. Joseph, J. Periaux, A fictitious domain approach to the direct numerical simulation of incompressible viscous flow past moving rigid bodies: application to particulate flow, Journal of Computational Physics 169 (2) (2001) 363–426.

[87] K. Yang, Y.-Q. Ma, Computer simulation of the translocation of nanoparticles with different shapes across a lipid bilayer, Nature Nanotechnology 5 (8) (2010) 579–583.

[88] H.-m. Ding, W.-d. Tian, Y.-q. Ma, Designing nanoparticle translocation through membranes by computer simulations, Acs Nano 6 (2) (2012) 1230–1238.

[89] X.-C. Luu, J. Yu, A. Striolo, Nanoparticles adsorbed at the water/oil interface: coverage and composition effects on structure and diffusion, Langmuir 29 (24) (2013) 7221–7228.

[90] M. Moseler, U. Landman, Formation, stability, and breakup of nanojets, Science 289 (5482) (2000) 1165–1169.

[91] B. Davidovitch, E. Moro, H. A. Stone, Spreading of viscous fluid drops on a solid substrate assisted by thermal fluctuations, Physical review letters 95 (24) (2005) 244505.

[92] Y. Hennequin, D. Aarts, J. van der Wiel, G. Wegdam, J. Eggers, H. Lekkerkerker, D. Bonn, Drop formation by thermal fluctuations at an ultralow surface tension, Physical review letters 97 (24) (2006) 244502.

[93] M. Rauscher, S. Dietrich, Wetting phenomena in nanofluidics, Annu. Rev. Mater. Res. 38 (2008) 143–172.

[94] B. Lin, J. Yu, S. A. Rice, Direct measurements of constrained brownian motion of an isolated sphere between two walls, Physical Review E 62 (3) (2000) 3909.

[95] M. D. Carbajal-Tinoco, R. Lopez-Fernandez, J. L. Arauz-Lara, Asymmetry in colloidal diffusion near a rigid wall, Physical review letters 99 (13) (2007) 138303.

[96] L. Landau, Lifshitz. 1959, fluid mechanics, Reading: Addison-Wesley.

[97] M. Bixon, R. Zwanzig, Boltzmann-langevin equation and hydrodynamic fluctuations, Physical Review 187 (1) (1969) 267.

[98] R. F. Fox, Gaussian stochastic processes in physics, Physics Reports 48 (3) (1978) 179–283.

[99] R. Adhikari, K. Stratford, M. Cates, A. Wagner, Fluctuating lattice boltzmann, EPL (Europhysics Letters) 71 (3) (2005) 473.

[100] B. Dünweg, U. D. Schiller, A. J. Ladd, Statistical mechanics of the fluctuating lattice boltzmann equation, Physical Review E 76 (3) (2007) 036704.

[101] M. Gross, R. Adhikari, M. Cates, F. Varnik, Thermal fluctuations in the lattice boltzmann method for nonideal fluids, Physical Review E 82 (5) (2010) 056714.

[102] P. Hoogerbrugge, J. Koelman, Simulating microscopic hydrodynamic phenomena with dissipative particle dynamics, EPL (Europhysics Letters) 19 (3) (1992) 155.

[103] R. D. Groot, P. B. Warren, Dissipative particle dynamics: Bridging the gap between atomistic and mesoscopic simulation, Journal of Chemical Physics 107 (11) (1997) 4423.

[104] A. Malevanets, R. Kapral, Mesoscopic model for solvent dynamics, The Journal of chemical physics 110 (17) (1999) 8605–8613.

[105] A. Lamura, G. Gompper, T. Ihle, D. Kroll, Multi-particle collision dynamics: Flow around a circular and a square cylinder, EPL (Europhysics Letters) 56 (3) (2001) 319.

[106] K. L. Johnson, K. L. Johnson, Contact mechanics, Cambridge university press, 1987.

[107] V. Popov, Contact mechanics and friction: physical principles and applications, Springer Science & Business Media, 2010.

[108] P. Wriggers, T. A. Laursen, Computational contact mechanics, Vol. 30167, Springer, 2006.

[109] J. C. Simo, P. Wriggers, R. L. Taylor, A perturbed lagrangian formulation for the finite element solution of contact problems, Computer methods in applied mechanics and engineering 50 (2) (1985) 163–180.

[110] M. A. Puso, T. A. Laursen, A mortar segment-to-segment contact method for large deformation solid mechanics, Computer methods in applied mechanics and engineering 193 (6) (2004) 601–629.

[111] T. Andersson, The boundary element method applied to two-dimensional contact problems with friction, in: Boundary element methods, Springer, 1981, pp. 239–258.

[112] F. Paris, A. Blazquez, J. Canas, Contact problems with nonconforming discretizations using boundary element method, Computers & structures 57 (5) (1995) 829–839.

[113] S. Psakhie, Y. Horie, S. Y. Korostelev, A. Y. Smolin, A. Dmitriev, E. Shilko, S. Alekseev, Method of movable cellular automata as a tool for simulation within the framework of mesomechanics, Russian Physics Journal 38 (11) (1995) 1157–1168.

[114] S. Psakhie, Y. Horie, G. Ostermeyer, S. Y. Korostelev, A. Y. Smolin, E. Shilko, A. Dmitriev, S. Blatnik, M. Špegel, S. Zavšek, Movable cellular automata method for simulating materials with mesostructure, Theoretical and applied fracture mechanics 37 (1) (2001) 311–334.

[115] V. Popov, S. Psakhie, Numerical simulation methods in tribology, Tribology International 40 (6) (2007) 916–923.

[116] S. Merabia, I. Pagonabarraga, A mesoscopic model for (de) wetting, The European Physical Journal E: Soft Matter and Biological Physics 20 (2) (2006) 209–214.

[117] C. Cupelli, B. Henrich, T. Glatzel, R. Zengerle, M. Moseler, M. Santer, Dynamic capillary wetting studied with dissipative particle dynamics, New Journal of Physics 10 (4) (2008) 043009.

[118] M. Liu, P. Meakin, H. Huang, Dissipative particle dynamics simulation of pore-scale multiphase fluid flow, Water resources research 43 (4).

[119] A. Tiwari, J. Abraham, Dissipative-particle-dynamics model for two-phase flows, Physical Review E 74 (5) (2006) 056701.

[120] D. Frenkel, B. Smit, Understanding molecular simulation: from algorithms to applications, Vol. 1, Academic press, 2001.

[121] D. C. Rapaport, The art of molecular dynamics simulation, Cambridge university press, 2004.

[122] M. L. Klein, W. Shinoda, Large-scale molecular dynamics simulations of self-assembling systems, Science 321 (5890) (2008) 798–800.

[123] P. Espanol, Statistical mechanics of coarse-graining, in: Novel Methods in Soft Matter Simulations, Springer, 2004, pp. 69–115.

[124] Y. Chen, J. D. Lee, Connecting molecular dynamics to micromorphic theory.(i). instantaneous and averaged mechanical variables, Physica A: Statistical Mechanics and its Applications 322 (2003) 359–376.

[125] Y. Chen, J. D. Lee, Connecting molecular dynamics to micromorphic theory.(ii). balance laws, Physica A: Statistical Mechanics and its Applications 322 (2003) 377–392.

[126] C. K. Aidun, J. R. Clausen, Lattice-boltzmann method for complex flows, Annual review of fluid mechanics 42 (2010) 439–472.

[127] J. Zhang, Lattice boltzmann method for microfluidics: models and applications, Microfluidics and Nanofluidics 10 (1) (2011) 1–28.

[128] M. Liu, G. Liu, Smoothed particle hydrodynamics (sph): an overview and recent developments, Archives of computational methods in engineering 17 (1) (2010) 25–76.

[129] J. Monaghan, Smoothed particle hydrodynamics and its diverse applications, Annual Review of Fluid Mechanics 44 (2012) 323–346.

[130] S. Li, W. K. Liu, Meshfree and particle methods and their applications, Applied Mechanics Reviews 55 (1) (2002) 1–34.

[131] G. Zhou, W. Ge, J. Li, Theoretical analysis on the applicability of traditional sph method, Chinese Science Bulletin 58 (24) (2013) 2970–2978.

[132] N. Filipovic, M. Ivanovic, M. Kojic, A comparative numerical study between dissipative particle dynamics and smoothed particle hydrodynamics when applied to simple unsteady flows in microfluidics, Microfluidics and nanofluidics 7 (2) (2009) 227–235.

[133] P. Espanol, Hydrodynamics from dissipative particle dynamics, Physical Review E 52 (2) (1995) 1734.

[134] P. Espanol, P. Warren, Statistical mechanics of dissipative particle dynamics, EPL (Europhysics Letters) 30 (4) (1995) 191.

[135] C. Marsh, G. Backx, M. Ernst, Fokker-planck-boltzmann equation for dissipative particle dynamics, EPL (Europhysics Letters) 38 (6) (1997) 411.

[136] C. Marsh, G. Backx, M. Ernst, Static and dynamic properties of dissipative particle dynamics, Physical Review E 56 (2) (1997) 1676.

[137] P. Espanol, M. Revenga, Smoothed dissipative particle dynamics, Physical Review E 67 (2) (2003) 026705.

[138] X. Bian, S. Litvinov, R. Qian, M. Ellero, N. A. Adams, Multiscale modeling of particle in suspension with smoothed dissipative particle dynamics, Physics of Fluids (1994-present) 24 (1) (2012) 012002.

[139] P. M. Kulkarni, C.-C. Fu, M. S. Shell, L. G. Leal, Multiscale modeling with smoothed dissipative particle dynamics, The Journal of chemical physics 138 (23) (2013) 234105.

[140] E. E. Keaveny, I. V. Pivkin, M. Maxey, G. E. Karniadakis, A comparative study between dissipative particle dynamics and molecular dynamics for simple-and complex-geometry flows, The Journal of chemical physics 123 (10) (2005) 104107.

[141] A. Satoh, T. Majima, Comparison between theoretical values and simulation results of viscosity for the dissipative particle dynamics method, Journal of colloid and interface science 283 (1) (2005) 251–266.

[142] A. Satoh, Introduction to Molecular-Microsimulation for Colloidal Dispersions, Vol. 17, Elsevier, 2003.

[143] I. Pagonabarraga, M. Hagen, D. Frenkel, Self-consistent dissipative particle dynamics algorithm, EPL (Europhysics Letters) 42 (4) (1998) 377.

[144] M. P. Allen, D. J. Tildesley, J. R. Banavar, Computer simulation of liquids, Physics Today 42 (3) (2008) 105–106.

[145] G. Besold, I. Vattulainen, M. Karttunen, J. M. Polson, Towards better integrators for dissipative particle dynamics simulations, Physical Review E 62 (6) (2000) R7611.

[146] I. Vattulainen, M. Karttunen, G. Besold, J. M. Polson, Integration schemes for dissipative particle dynamics simulations: From softly interacting systems towards hybrid models, The Journal of chemical physics 116 (10) (2002) 3967–3979.

[147] P. Nikunen, M. Karttunen, I. Vattulainen, How would you integrate the equations of motion in dissipative particle dynamics simulations?, Computer Physics Communications 153 (3) (2003) 407–423.

[148] A. Kumar, Y. Asako, E. Abu-Nada, M. Krafczyk, M. Faghri, From dissipative particle dynamics scales to physical scales: a coarse-graining study for water flow in microchannel, Microfluidics and nanofluidics 7 (4) (2009) 467–477.

[149] I. V. Pivkin, G. E. Karniadakis, Coarse-graining limits in open and wall-bounded dissipative particle dynamics systems, The Journal of chemical physics 124 (18) (2006) 184101.

[150] R. D. Groot, K. Rabone, Mesoscopic simulation of cell membrane damage, morphology change and rupture by nonionic surfactants, Biophysical journal 81 (2) (2001) 725–736.

[151] A. A. Gavrilov, A. V. Chertovich, P. G. Khalatur, A. R. Khokhlov, Effect of nanotube size on the mechanical properties of elastomeric composites, Soft Matter 9 (15) (2013) 4067–4072.

[152] J. C. Shillcock, R. Lipowsky, Tension-induced fusion of bilayer membranes and vesicles, Nature materials 4 (3) (2005) 225–228.

[153] R. M. Füchslin, H. Fellermann, A. Eriksson, H.-J. Ziock, Coarse graining and scaling in dissipative particle dynamics, The Journal of chemical physics 130 (21) (2009) 214102.

[154] M. Revenga, I. Zuniga, P. Espanol, Boundary conditions in dissipative particle dynamics, Computer physics communications 121 (1999) 309–311.

[155] S. Willemsen, H. Hoefsloot, P. Iedema, No-slip boundary condition in dissipative particle dynamics, International Journal of Modern Physics C 11 (05) (2000) 881–890.

[156] D. Duong-Hong, N. Phan-Thien, X. Fan, An implementation of no-slip boundary conditions in dpd, Computational mechanics 35 (1) (2004) 24–29.

[157] I. V. Pivkin, G. E. Karniadakis, A new method to impose no-slip boundary conditions in dissipative particle dynamics, Journal of Computational Physics 207 (1) (2005) 114–128.

[158] D. Visser, H. Hoefsloot, P. Iedema, Comprehensive boundary method for solid walls in dissipative particle dynamics, Journal of computational Physics 205 (2) (2005) 626–639.

[159] L. Wang, W. Ge, J. Li, A new wall boundary condition in particle methods, Computer physics communications 174 (5) (2006) 386–390.

[160] B. Henrich, C. Cupelli, M. Moseler, M. Santer, An adhesive dpd wall model for dynamic wetting, EPL (Europhysics Letters) 80 (6) (2007) 60004.

[161] A. M. Altenhoff, J. H. Walther, P. Koumoutsakos, A stochastic boundary forcing for dissipative particle dynamics, Journal of Computational Physics 225 (1) (2007) 1125–1136.

[162] H. Lei, D. A. Fedosov, G. E. Karniadakis, Time-dependent and outflow boundary conditions for dissipative particle dynamics, Journal of computational physics 230 (10) (2011) 3765–3779.

[163] S. K. Ranjith, B. Patnaik, S. Vedantam, No-slip boundary condition in finite-size dissipative particle dynamics, Journal of Computational Physics 232 (1) (2013) 174–188.

[164] A. Mehboudi, M. S. Saidi, Physically based wall boundary condition for dissipative particle dynamics, Microfluidics and nanofluidics 17 (1) (2014) 181–198.

[165] S. Pal, C. Lan, Z. Li, E. D. Hirleman, Y. Ma, Symmetry boundary condition in dissipative particle dynamics, Journal of Computational Physics 292 (2015) 287–299.

[166] M. Mandell, On the properties of a periodic fluid, Journal of Statistical Physics 15 (4) (1976) 299–305.

[167] W. Pan, I. Pivkin, G. Karniadakis, Single-particle hydrodynamics in dpd: A new formulation, EPL (Europhysics Letters) 84 (1) (2008) 10012.

[168] X. Fan, N. Phan-Thien, N. T. Yong, X. Wu, D. Xu, Microchannel flow of a macromolecular suspension, Physics of Fluids (1994-present) 15 (1) (2003) 11–21.

[169] X. Fan, N. Phan-Thien, S. Chen, X. Wu, T. Y. Ng, Simulating flow of dna suspension using dissipative particle dynamics, Physics of Fluids (1994-present) 18 (6) (2006) 063102.

[170] N. Moumen, R. S. Subramanian, J. B. McLaughlin, Experiments on the motion of drops on a horizontal solid surface due to a wettability gradient, Langmuir 22 (6) (2006) 2682–2690.

[171] P. Warren, Vapor-liquid coexistence in many-body dissipative particle dynamics, Physical Review E 68 (6) (2003) 066702.

[172] A. Ghoufi, P. Malfreyt, Mesoscale modeling of the water liquid-vapor interface: A surface tension calculation, Physical Review E 83 (5) (2011) 051601.

[173] M. Arienti, W. Pan, X. Li, G. Karniadakis, Many-body dissipative particle dynamics simulation of liquid/vapor and liquid/solid interactions, The Journal of chemical physics 134 (20) (2011) 204114.

[174] A. Ghoufi, P. Malfreyt, Calculation of the surface tension from multibody dissipative particle dynamics and monte carlo methods, Physical Review E 82 (1) (2010) 016706.

[175] J. D. Halverson, C. Maldarelli, A. Couzis, J. Koplik, A molecular dynamics study of the motion of a nanodroplet of pure liquid on a wetting gradient, The Journal of chemical physics 129 (16) (2008) 164708.

[176] X. Yao, H. Bai, J. Ju, D. Zhou, J. Li, H. Zhang, B. Yang, L. Jiang, Running droplet of interfacial chemical reaction flow, Soft Matter 8 (22) (2012) 5988–5991.

[177] O. Bliznyuk, J. R. Seddon, V. Veligura, E. S. Kooij, H. J. Zandvliet, B. Poelsema, Directional liquid spreading over chemically defined radial wettability gradients, ACS applied materials & interfaces 4 (8) (2012) 4141–4148.

[178] X. Xu, T. Qian, Droplet motion in one-component fluids on solid substrates with wettability gradients, Physical Review E 85 (5) (2012) 051601.

[179] M. G. Pollack, Electrowetting-based microactuation of droplets for digital microfluidics, Ph.D. thesis, Duke University (2001).

[180] R. S. Subramanian, N. Moumen, J. B. McLaughlin, Motion of a drop on a solid surface due to a wettability gradient, Langmuir 21 (25) (2005) 11844–11849.

[181] G. J. Shah, C.-J. C. Kim, Meniscus-assisted high-efficiency magnetic collection and separation for ewod droplet microfluidics, Microelectromechanical Systems, Journal of 18 (2) (2009) 363–375.

[182] S. Aramrak, M. Flury, J. B. Harsh, Detachment of deposited colloids by advancing and receding air–water interfaces, Langmuir 27 (16) (2011) 9985–9993.

[183] N. Chatterjee, S. Lapin, M. Flury, Capillary forces between sediment particles and an air–water interface, Environmental science & technology 46 (8) (2012) 4411–4418.

[184] I. Goldasteh, G. Ahmadi, A. R. Ferro, Monte carlo simulation of micron size spherical particle removal and resuspension from substrate under fluid flows, Journal of Aerosol Science 66 (2013) 62–71.

[185] R. H. Hardin, N. J. A. Sloane, W. D. Smith, Tables of spherical codes with icosahedral symmetry.
URL http://NeilSloane.com/icosahedral.codes/

[186] M. Laradji, M. J. Hore, Nanospheres in phase-separating multicomponent fluids: A three-dimensional dissipative particle dynamics simulation, The Journal of chemical physics 121 (21) (2004) 10641–10647.

[187] M. J. Hore, M. Laradji, Microphase separation induced by interfacial segregation of isotropic, spherical nanoparticles, The Journal of chemical physics 126 (24) (2007) 244903.

[188] M. Huang, Z. Li, H. Guo, The effect of janus nanospheres on the phase separation of immiscible polymer blends via dissipative particle dynamics simulations, Soft Matter 8 (25) (2012) 6834–6845.

[189] I. Salib, X. Yong, E. J. Crabb, N. M. Moellers, G. T. McFarlin IV, O. Kuksenok, A. C. Balazs, Harnessing fluid-driven vesicles to pick up and drop off janus particles, ACS nano 7 (2) (2013) 1224–1238.

[190] H. Fan, A. Striolo, Nanoparticle effects on the water-oil interfacial tension, Physical Review E 86 (5) (2012) 051610.

[191] K. Johnson, K. Kendall, A. Roberts, Surface energy and the contact of elastic solids, in: Proceedings of the Royal Society of London A: Mathematical, Physical and Engineering Sciences, Vol. 324, The Royal Society, 1971, pp. 301–313.

[192] J. M. Kim, R. J. Phillips, Dissipative particle dynamics simulation of flow around spheres and cylinders at finite reynolds numbers, Chemical engineering science 59 (20) (2004) 4155–4168.

[193] S. Chen, N. Phan-Thien, B. C. Khoo, X. J. Fan, Flow around spheres by dissipative particle dynamics, Physics of Fluids (1994-present) 18 (10) (2006) 103605.

[194] C. Lan, S. Pal, Z. Li, Y. Ma, Numerical simulations of the digital microfluidic manipulation of single microparticles, Langmuir 31 (35) (2015) 9636–9645.

[195] T. E. ToolBox, Friction coefficients for some common materials and materials combinations. URL http://www.engineeringtoolbox.com/friction-coefficients-d_778.html

[196] R. Fürstner, W. Barthlott, C. Neinhuis, P. Walzel, Wetting and self-cleaning properties of artificial superhydrophobic surfaces, Langmuir 21 (3) (2005) 956–961.

[197] Y.-L. Zhang, H. Xia, E. Kim, H.-B. Sun, Recent developments in superhydrophobic surfaces with unique structural and functional properties, Soft Matter 8 (44) (2012) 11217–11231.

[198] T. Darmanin, F. Guittard, Recent advances in the potential applications of bioinspired superhydrophobic materials, Journal of Materials Chemistry A 2 (39) (2014) 16319–16359.

[199] M. Toma, G. Loget, R. M. Corn, Flexible teflon nanocone array surfaces with tunable superhydrophobicity for self-cleaning and aqueous droplet patterning, ACS applied materials & interfaces 6 (14) (2014) 11110–11117.

[200] J. Zhu, C.-M. Hsu, Z. Yu, S. Fan, Y. Cui, Nanodome solar cells with efficient light management and self-cleaning, Nano letters 10 (6) (2009) 1979–1984.

[201] L. K. Verma, M. Sakhuja, J. Son, A. Danner, H. Yang, H. Zeng, C. Bhatia, Self-cleaning and antireflective packaging glass for solar modules, Renewable Energy 36 (9) (2011) 2489–2493.